UNIVERSITÀ
DEGLI STUDI
FIRENZE

DOTTORATO DI RICERCA IN
INGEGNERIA INDUSTRIALE

CICLO XXXI

COORDINATORE Prof. Maurizio De Lucia

Development of a small-size parabolic trough collector: design and experimental test

Settore Scientifico Disciplinare ING/IND 09

Dottorando
Dott. Michele Salvestroni

Tutore
Prof. Maurizio De Lucia

Coordinatore
Prof. Maurizio De Lucia

Anni 2015/2018

Contents

Abstract **3**

List of original publications **7**

1 Introduction **8**
1.1 Energy context 8
1.2 Concentrating collectors 10
1.3 Collectors for medium temperature 14
1.3.1 PTC facilities for process heat 22
1.4 Parameters of PTC 25
1.5 Components of PTC 27
1.5.1 Mirrors 27
1.5.2 Receiver 28
1.5.3 Heat transfer fluid 31
1.5.4 The bearing structure 32
1.6 Theory of PTC 33
1.7 Test on PTC 36

2 The design of the m-PTC **42**
2.1 Optical analysis 42
2.2 The FEM model 50

3 The prototype of m-PTC and the indoor test bench **63**
3.1 The prototype of m-PTC 63

3.2 The test bench for heat loss measurement . . . 66
3.3 Heat loss results . . . 69
3.4 Calculation of the emissivity . . . 71

4 The efficiency test of m-PTC **73**
4.1 The test rig . . . 73
4.1.1 Main components of the test rig . . . 73
4.1.2 Test loop design . . . 79
4.1.3 Measurement sensors . . . 81
4.1.4 Data acquisition . . . 83
4.1.5 Operations of the system . . . 84
4.2 Test of thermal efficiency . . . 85
4.2.1 Procedure and first tests . . . 85
4.2.2 Calculation of the uncertainty . . . 89
4.2.3 Efficiency test . . . 93
4.3 New results of efficiency test . . . 98
4.4 Fitting of the data . . . 100
4.5 Validation of FEM model . . . 103

5 Evaluation of the annual performances **106**
5.1 Production of heat at medium temperature . . . 106
5.2 Estimated costs . . . 112

6 Conclusions and future perspectives **113**

Bibliography **117**

Appendix **125**
Error theory . . . 125
Fitting and uncertainties . . . 127

Abstract

The exploitation of fossil fuels to produce energy (e.g. electric, heat) has increased dramatically the concentration of greenhouse gases in atmosphere. This process is causing the rise of the average temperature of Earth with effects for the environment and for the human life. As a consequence, several strategies have to be undertaken to reduce the use of fossil fuels. In this context the renewable energies play a relevant role.

Among renewable technologies, solar thermal collectors could offer an interesting solution to cover the heat demand needed by human activities. The heat demand constitutes a relevant fraction of the entire consumption of energy: in EU about the 50% of the energy is used to produce heat, in particular for space heating and for industrial process heat. Concerning the latter, about the 11% of heat is required at temperatures below 100 °C and a further 26% is required in a range between 100°C and 200°C. At present, whereas for low temperature applications up to 100°C, the solar thermal collectors represent a mature technology, the appropriate solar collector technology for the production of heat between 100°C and 250°C is still missing. Indeed non-tracking collectors, such as flat plane collectors and evacuated collectors, and tracking collectors, such as large parabolic trough collectors, for different reasons have proven to be not adequate for process heat applications.

The research topic in this PhD program deals with the design, the realization and the experimental test of an innovative small size parabolic trough collector (m-PTC) suitable to produce heat at medium temperature ($100 - 250$°C) with higher efficiency than the solar thermal collectors.

This work is organized into four main topics:

- the state of the art of solar collectors for process heat and the theory of PTC;
- the design of the parabolic collector through the realization of numerical models;
- the realization of the prototype of the parabolic trough collector and the implementation of the test bench for heat loss test of the receiver tube;
- the design of the test rig for outdoor efficiency test on the collector, the experimental tests and the calculation of the efficiency curve of the collector.

Starting from the study of the state of the art, the design phase for the small parabolic trough collector has dealt with the numerical modelization of the parabolic collector from the optical, thermal and structural point of view. This phase has been necessary to fully understand the physics of the system, to identify the relevant parameters and to properly realize the parabolic collector.

The optical analysis through Monte Carlo ray tracing has permitted to fix the dimensions of the collectors components, the width of the mirror and the diameter of receiver tube. It has been found the optimum rim angle of the parabolic mirror, that permits to reduce the weight of optical errors and to increase the acceptance angle of the radiation on the absorber tube, and the radiation distribution on the absorber tube.

Afterwards, a termofluidodynamic FEM model of the receiver tube has been developed and a parametric analysis has been carried out to optimize the components of the receiver tube. Furthermore, the numerical model has allowed to obtain useful details for the realization of the prototype and for the design of the test rig such as the optimal mass flow and the rise in temperature along the collector. A structural finite element model has been realized in order to compute the thermal stress on the absorber tube.

Following the indications of the numerical models the prototype of an innovative parabolic trough collector has been realized. First of all, the m-PTC collector is innovative for its dimensions: it is characterized by extremely small size since it has been designed to be suitable for the integration on the roofs of industrial environments where the space for installation of solar collectors is in general limited. For these reasons, it is much more compact and transportable respect than the

parabolic trough collectors developed to date. It possesses an aperture width of just 420 mm and it is 1800 mm long. Another relevant aspect is that the collector aims to achieve performances higher than solar thermal collectors in the temperature range of $100 - 250°C$. This has been made possible thanks to the thermal property of the evacuated receiver tube, to the high quality of the materials used for the receiver tube (e.g. the selective coating) and thanks to the design solutions adopted.

Furthermore, the absorber tube, characterized by an external diameter of 10 mm, is formed by two concentric tubes so that the fluid inlet and output are at the same side (one-end receiver). This configuration presents several advantages respect the standard one since it is more robust, more simple to realize and less expensive since it possesses fewer number of sealings. Concerning the tracking system, a novel solution in which the rotation axis coincides with the absorber tube has been implemented, permitting to the absorber to remain in fixed position during operations and avoiding flexible pipe connections.

An indoor test rig has been realized to test the thermal performances and to verify the good quality of the receiver tube. The test rig allows the measurement of the heat losses of receiver heating up the absorber tube through the Joule effect.

In order to fully characterize the collector, a test rig for outdoor test has been designed. The test bench has been carefully projected in order to satisfy the requirements imposed by the standard test on solar concentrating collectors. The measurement instrumentation has been properly selected in order to minimize the uncertainty on the final variables to be obtained, the useful thermal power and the efficiency of the collector.

Tests have been run for different inlet temperatures of the fluid and different conditions of irradiance. An accurate analysis of the measurement uncertainties has been conducted. Since the results of the first tests have not been in agreement with the outcomes of the laboratory tests, after a deep examination of the causes, the test rig has been modified in order to correct the systematic errors and to improve the accuracy of the system. New experimental tests have been carried out. The outcomes of these tests are less scattered respect the previous one, present less uncertainty and are in agreement with heat loss test.

The data have been fitted through a multiple linear regression based on weighted least squares obtaining the efficiency curve of the collector. The peak optical ef-

ficiency of the m-PTC has been estimated to be 69%. The predicted thermal efficiency at fluid temperature of 180°C, is 63% $\pm$4%. The experimental results have been compared with the numerical outcomes of the termofluidodynamic FEM model that has been validated.

The yearly performances of the m-PTC have been evaluated through dynamical simulations with TRNSYS. It has been compared the m-PTC with an evacuated collector and a linear Fresnel collector for four different locations and different levels of inlet temperature. Finally, based on the components and the materials used, a prediction of the cost of m-PTC has been reported.

In light of the results, the m-PTC realized has proven to be suitable to produce heat at medium temperature with high efficiency. Thanks to the design, the collector could overcome the main limitations of concentrating collectors for process heat, being small, easy to integrate on the roofs and easy to maintain.

List of original publications

This study is based on the following original publications:

G. Pierucci, S. Hosouli, M. Salvestroni, M. Messeri, F. Fagioli, F. Taddei and M. De Lucia (2018). Experimental Methodology and Thermal Loss Tests on Small Size Absorber Tubes for Solar Applications. *Energies*, 11(10), 2552.

M. Salvestroni, G. Pierucci, F. Fagioli, A. Pourreza, M. Messeri, F. Taddei, S. Hosouli, H. Rashidi and M De Lucia. Design of a small size PTC: computational model for the receiver tube and validation with heat loss test. Conference paper, Solaris 2018, Chengdu, China, 29-30 august, 2018

G. Pierucci, S. Hosouli, M. Messeri, M. Salvestroni, F. Fagioli, F. Taddei, A. Pourreza, H. Rashidi and M. De Lucia. Realization of a Test Rig for Small Solar Collectors and Preliminary Test. Conference paper. Solar Paces 2018, Casablanca, Morocco, 2-5 October 2018

Chapter 1

Introduction

1.1 Energy context

The 80% of the global primary energy supply comes from fossil fuels: coal, liquid petroleum and natural gas (fig. 1.1) which are responsible for the emissions of greenhouse-gas (GHG) such as CO2 [1].

The CO2 concentration in atmosphere has grown considerably in the last years reaching the 410 ppm (parts per million) in 2018; prior to 1800, the atmospheric CO2 concentration was about 280 ppm. The majority of the scientific community believes that this trend is responsible for the rise of the average temperature of the Earth: "It is extremely likely that human influence has been the dominant cause of the observed warming since the mid-20th century"[2]. The Intergovernmental Panel on Climate Change, IPCC, states that human activities are estimated to have caused in 2017 approximately 1.0°C of global warming above pre-industrial levels. The average temperature of the Earth is increasing at 0.2°C per decade (fig. 1.2). Global warming could cause terrible effects on the Earth and on human life; currently many impacts of climate change have already been observed, including glacier retreat, changes in the timing of seasonal events (e.g., earlier flowering of plants), and changes in agricultural productivity [3].

Global warming is likely to reach 1.5°C between 2030 and 2052 if it continues to increase at the current rate. To maintain the rise in temperature below 1.5°C,

global net anthropogenic CO2 emissions should decline by about 45% from 2010 levels by 2030, reaching net zero around 2050 [2].

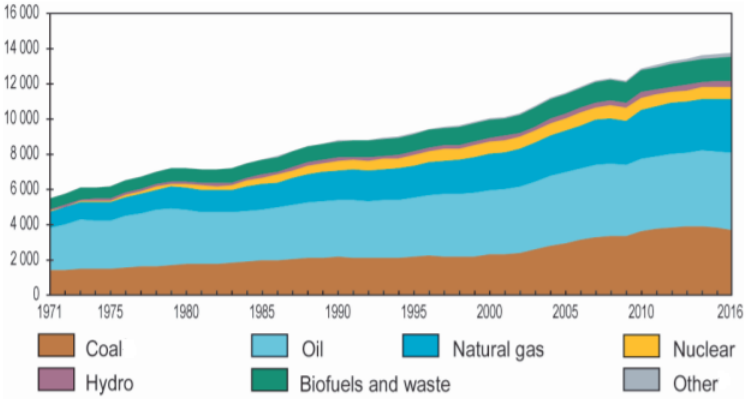

Figure 1.1: World energy consumptions expressed in million tonnes of oil equivalent from 1971 to 2016. From [1].

Several action has to be undertaken to limit the increase of the average temperature of the Earth. Renewable energies, i.e. solar technologies (photovoltaic, solar thermal collectors, concentrating solar collectors), wind power, hydropower, etc. play a relevant role in the struggle for the reduction of use of fossil fuels and the CO2 concentration decrease.

Focusing on heat consumption, the energy use for heat (water and space heating, cooking and industrial processes) accounted for more than one-half of total world final energy consumption in 2016 [4]. The 66% of heat generated worldwide is produced by fossil fuels and the 45% of this amount is used in industry as process heat [5].

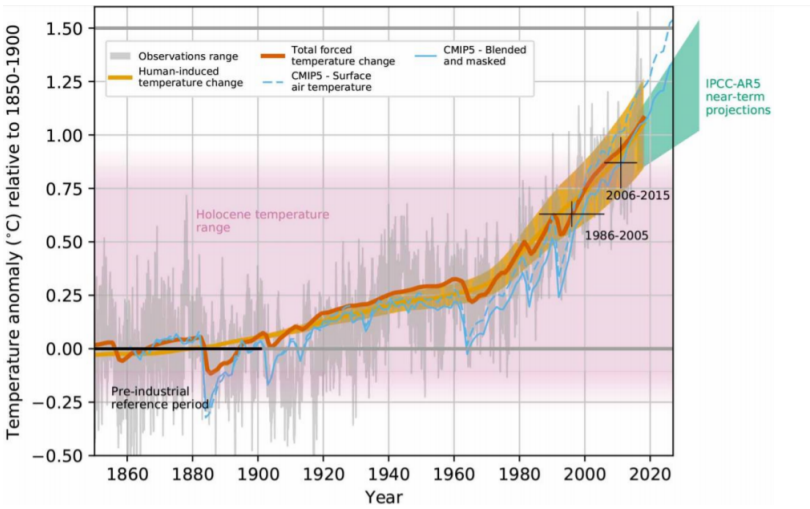

Figure 1.2: Temperature increase of the Earth [2].

1.2 Concentrating collectors

Concentrating collectors are solar collectors that use concentrators, such as mirrors or lenses, to focus solar radiation onto a receiver that carries a working fluid which is heated up to high temperature. Generally, the fluid goes to a steam turbine that is attached to a generator producing electricity. This system is called CSP, concentrated solar power.

Another use of concentrating collectors is the production of heat in a wide range of temperatures (100-350°C) without being connected to a power cycle to exploit directly the heat collected.

Until today, four different kinds of CSP power generation plants have been developed:

- solar parabolic dishes (SPD);
- parabolic trough collectors (PTC);
- solar power tower (SPT);

- linear Fresnel reflectors (LFR).

The parabolic-trough system is the most widely used CSP technology (82% of the total of the plant) and the most mature technology among concentrating collectors.

Generally, CSP plants consist of several components such as solar concentrators, receiver, thermal energy storage, steam turbine and electrical generator. The thermal energy storage represents the great advantage of CSP against other renewable energy technologies as photovoltaic or wind power since storing heat in the tank allows to provide dispatchable energy and power continuously [6]. Due to this feature, the power output of CSP with thermal energy storage does not depend directly on weather conditions; electricity can even be produced at night or periods with insufficient radiation. Moreover the flexibility and predictability given by the thermal storage system allows to provide many of the functions that are needed to support grid operation. Therefore CSP with TES can offer similar operational attributes as conventional power plants [7].

Potential locations for concentrating collector installations around the world are identified by using the distribution of Direct Normal Irradiance, DNI (fig. 1.3). The suitable location for CSP plants are contained in a zone called "sun belt" that is limited approximately by the two parallels 15- 40° north and south. Chile, Australia, North Africa, the Middle East, the Mediterranean, and vast areas in the United States including California, Arizona, Nevada, New Mexico, are the areas with the highest DNI. Commercially viable CSP plants should be realized in areas with a DNI of at least 2000–2800 $\mathrm{kWh}/(\mathrm{m}^2\mathrm{yr})$. Present commercial CSP plants are being developed based on this level of irradiance [6].

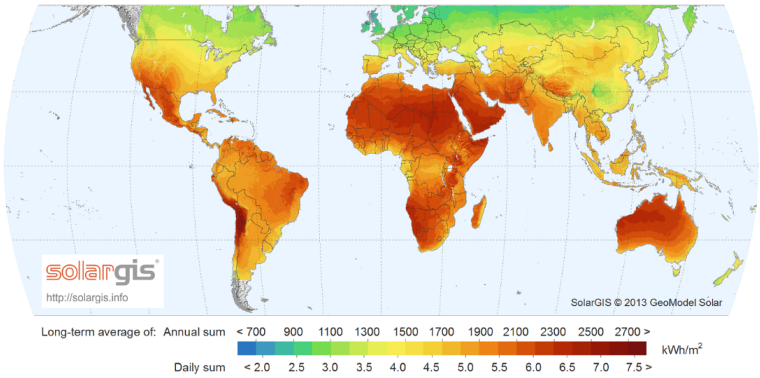

Figure 1.3: World DNI resource [8].

In Italy the highest value of DNI is in Sicily about 2000 $\mathrm{kWh}/(\mathrm{m}^2\mathrm{yr})$; other good areas are Sardinia, Apulia, and the Tyrrhenian coast with 1800 $\mathrm{kWh}/(\mathrm{m}^2\mathrm{yr})$ (fig.1.4). In Florence the average annual DNI is 1333 $\mathrm{kWh}/(\mathrm{m}^2\mathrm{yr})$. Italy has only three operational CSP plants one in Sicily, one in Sardinia and one in Umbria. The 5 MW Archimede parabolic trough solar plant in Sicily has been the first to use molten salts as heat transfer fluid; it is integrated in a combined-cycle gas facility.

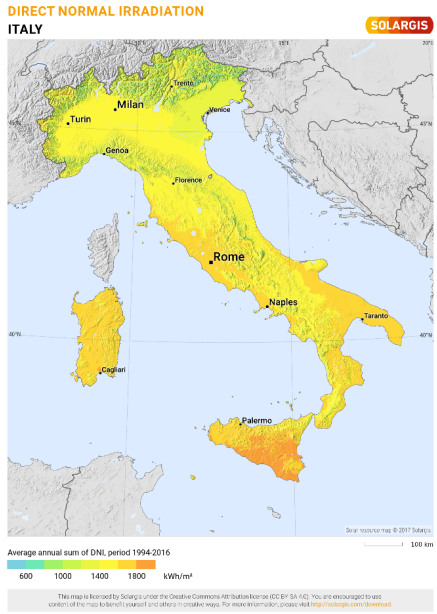

Figure 1.4: DNI map of Italy [8].

Parabolic trough collectors are the most mature technology among concentrating collectors. The first parabolic-trough system was developed in 1912 in Cairo, Egypt. At present, globally, there are 77 operational parabolic-trough power plants and most of them are located in Spain and the United States [6].

The parabolic trough collector is a solar collector that is straight in one dimension and curved as a parabola in the other two. The radiation which arrives parallel to the mirror plane of symmetry is focused along the focal line, where the receiver pipe is installed. A heat transfer fluid flows inside the receiver tube and absorbs concentrated solar energy from the pipe walls raising its enthalpy. In general, the parabolic trough collector is provided with a one-axis solar tracking system to ensure that the solar beam falls parallel to its axis.

Parabolic trough collectors can be used to generate electricity or to produce heat at low temperature (<100 °C), medium temperature (100-250°C) or at high temperature (>250°C).

The PTC used in the solar power plant for the generation of electricity have a typical large aperture width, of about 6-8 m, total lengths from 100 to 150 m and geometrical concentrating ratios between 20 and 30 (fig. 1.5) [9]. They can reach temperatures up to 550°C if molten salts are used as heat transfer fluid.

The PTC for heat production are characterized by smaller aperture widths, between 1 and 3 m, total lengths between 2 and 10 m and geometrical concentrating ratios between 15 and 20.

Figure 1.5: Example of big PTCs: Noor I CSP in Morocco.

1.3 Collectors for medium temperature

There is large amount of human activities that needs heat at low-medium temperatures (starting from T<100ºC up to 250ºC): industrial process heat (IPH), low-temperature heat demand with high consumption rates (domestic hot water, DHW, space heating and swimming pool heating) and heat-driven refrigeration and cooling.

In EU in 2015, about 50% of the final energy demand has been used for heating and cooling. Space heating represents the 27% of the final energy demand,

process heat represents the 16%. Only the 13% of the total heat is generated by renewable sources (12% from biomass) [10].

For what concerns the IPH, low and medium temperature processes (from T<100ºC up to 250ºC) presenting a high share of heat demands on the mining, food and beverage, tobacco, pulp and paper, machinery and transport, equipment, manufacturing sectors; high temperatures (T>250°C) presenting a high share of heat demand on the chemical, non-metallic minerals and basic metals production sectors. In table 1.1 are reported the temperature ranges for various industrial process. In Europe, about the 11% of requirement of heat for industrial process heat occurs at temperatures below 100 °C and a further 26% occurs in a range between 100 and 200°C [10, 11].

Table 1.1: Temperature ranges for some industrial processes. Adapted from [12].

Industry	Process	Temperature $[^{\circ}C]$
Dairy	Pressurization	60-80
	Sterilization	100–120
	Drying	120–180
	Concentrates	60–80
	Boiler feed water	60–90
Tinned food	Sterilization	110–120
	Pasteurization	60–80
	Cooking	60–90
	Bleaching	60–90
Textile	Bleaching, dyeing	60–90
	Drying, degreasing	100–130
	Dyeing	70–90
	Fixing	160–180
	Pressing	80–100
Paper	Cooking, drying	60–80
	Boiler feedwater	60–90
	Bleaching	130–150
Chemical	Soaps	200–260
	Synthetic rubber	150–200
	Processing heat	120–180
	Pre-heating water	60–90
Bricks and Blocks	Curing	60-140
Plastics	Preparation	120–140
	Distillation	140–150
	Separation	200–220
	Extension	140–160
	Drying	180–200
	Blending	120–140

Despite process heat is recognized as the application with highest potential among solar heating and cooling applications, Solar Heat for Industrial Processes (SHIP) still presents a modest share of installed capacity respect the total installed

solar thermal capacity. However, the 2017 was a record year for solar heating in industrial processes, with 124 projects in 17 countries adding over 130 MWth (an increase of 46%), led by the first 100-MWth phase of the Miraah project for enhanced oil recovery in Oman [1].

The interest in using solar systems for supplying the thermal energy required by industry is not only because a large amount of heat is consumed in this sector, but also because loads are usually constant throughout the year, and the plants usually already have maintenance crews who could also care for the solar fields, thus ensuring operation of the system at peak efficiency [9].

The drawbacks of using solar energy in IPH are [9]:

- Land availability and cost. Existing rooftops often not large or strong enough to support the solar field.
- Industrial effluents. An industrial environment involves higher risk of corrosion of solar collectors than a commercial or residential setting.
- Non-constant energy source.
- Availability of conservation alternatives. Many plants can employ simple, inexpensive energy conservation techniques which should precede any commitment to solar energy. These include using waste heat from high-temperature processes to supply low-temperature processes (such as boiler feed-water preheat).
- Economics. Industry often requires payback periods of less than 5 years.

Finally, the major barrier to the production of process heat through solar energy is represented at the moment by the lack of the right solar collector technology. While there are well-established technologies tackling low temperature applications ($T < 100$ºC) such as flat plate collectors and evacuated collectors, for medium temperature applications (100ºC $< T < 250$ºC) the suitable technology of solar collectors has not been established.

As can be seen from figure 1.6, potentially the solar collectors suitable to generate heat at medium temperature are: non-tracking collectors, such as evacuated flat plate (EFP) and evacuated tube collectors (ETC); passive tracking collectors (tracking that is functionalized by non imaging optical components, e.g.

compound parabolic collector, CPC); tracking collectors such as small parabolic trough collectors (PTC) and Fresnel collectors (LFC) [13].

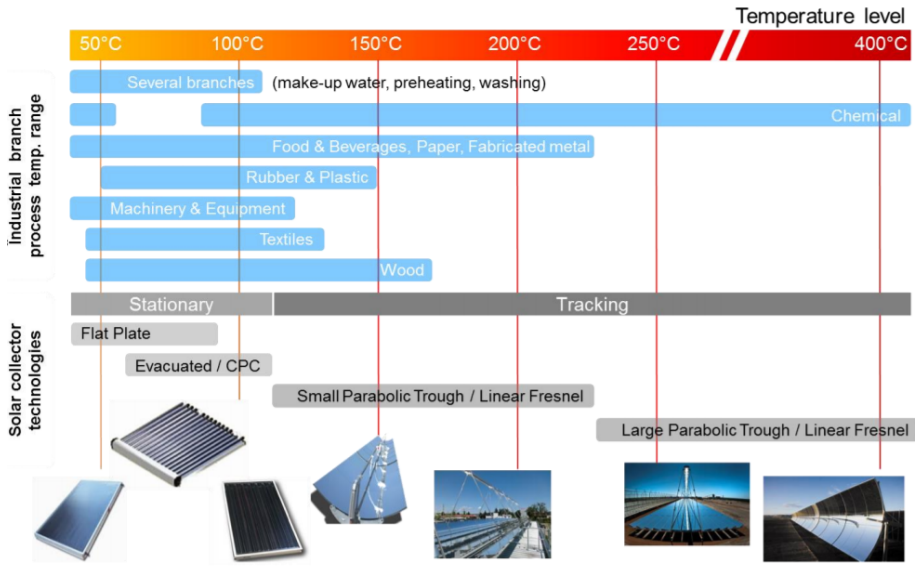

Figure 1.6: Solar thermal collectors and their temperature ranges of application. From [5].

No one of this technologies has emerged as the best for low-medium temperature applications for different reasons. Therefore, there is a strong need to develop a collector technology for medium temperature to make solar energy a viable option to produce heat at that temperatures.

For what concerns flat plate, evacuated tube collectors and CPC collectors, they have low performances above 100°C as can be observed in figure 1.7.

In general the advantages of PTCs for the production of medium temperature heat compared to non tracking solar collectors are several. Thanks to the use of mirrors, they have smaller absorbing surfaces for a given thermal power requirement; therefore they have lower thermal losses and higher efficiency. For this reason, higher working temperature can be reached. Moreover, there is no risk of

dangerous stagnation temperatures, since in such cases the control system sends the collector into stow position [14].

PTC and LFC system present also some disadvantages: they are still much more expensive compared to non tracking collectors. The costs of solar heat for industrial process heat strongly depend on process temperature level, demand continuity, project size and the level of solar radiation of the site. For conventional FPC and ETC, range from 2.5 to 8 eurocents/kWh; for concentrated systems, heating costs are in the range of 6-9 eurocents/kWh. Concentrated systems include, Parabolic Trough Collectors with costs ranging from USD 600–2000/kW, and Linear Fresnel collectors in the range of USD 1200–1800/ kW [15]. Moreover for what concerns PTC the solar tracking system increases installation and maintenance costs, and the complexity of the system. Also the need to clean the mirrors frequently increases maintenance costs [14].

Another disadvantage is that PTCs can only use direct solar radiation, thus their installation is geographically limited; at very high wind speeds operation must be interrupted and the collectors sent into stow position.

PTC and LFC are in general characterized by big dimensions that make difficult to integrate them on the roofs of industrial/commercial environments due to reduced space availability. Besides the installation on the roofs is partly impeded due to their potential for high dynamic wind loading [16]. The PTCs should therefore be small (aperture width less than 3 m), lightweight, easy to install, easy to maintain, low-cost and highly efficient [16].

If the main issues relating to the PTC for process heat will be solved, this technology could offer the solution for the production of medium temperature heat. Several solar collectors aiming to produce heat at medium temperature have been developed in the last years.

For what concerns non tracking collectors, TVP Solar developed a high vacuum, non-tracking flat plate solar thermal collector. This collector can reach 180°C with an average efficiency, related to gross area, of around 45%, at a DNI of $800\,\mathrm{W/m^2}$, for a double effect absorption chiller [13, 17]. The advantage of this collector is that it uses global irradiance instead of direct irradiance.

Winston et al. [18] developed a passive External Compound Parabolic Concentrator (XCPC), a collector which could achieve a 200°C fluid outlet temperature with an efficiency of 36–40% (at a DNI of $800\,\mathrm{W/m^2}$).

Kloben has certified an evacuated CPC collector with an efficiency of 41% at 160 °C (DNI 800 W/m^2) [19].

A rooftop solar, semi-passive tracking concentrating collector, developed by Chromasun, can deliver heat at temperatures of 200°C with 44% efficiency, when DNI is 850 W/m^2 [20].

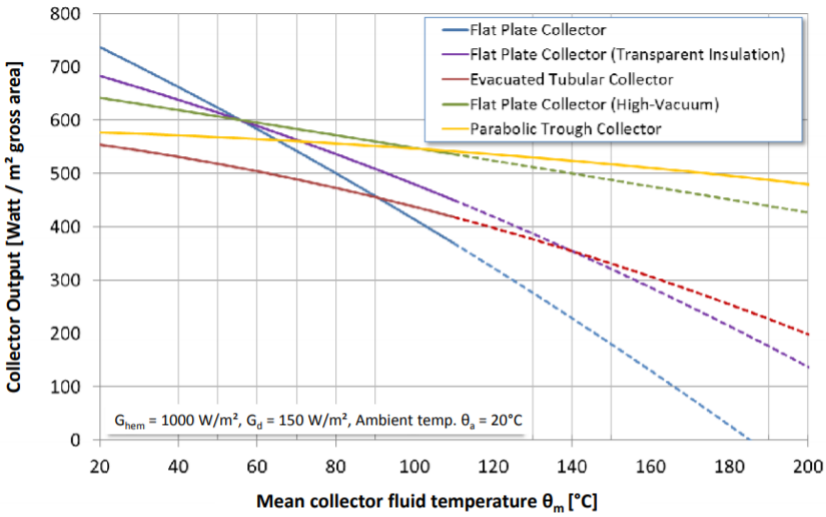

Figure 1.7: Example of efficiency of solar thermal collectors [5].

There are few active-tracking solar collectors which have been commercially developed that can meet the needs of the commercial/industrial heating market.

The linear Fresnel collector developed by Inersur has an aperture width of 0.4 m, a concentration factor of 12, a peak optical efficiency of 75% and 51% thermal efficiency at 150°C [21].

Few PTC of small size have been developed in the recent years and are available on the market. In general they do not present good performances at 180°C since they are equipped with non evacuated receiver tubes to keep the costs low [22].

The PolyTrough 1800 solar collector characterized by an aperture width of 1.845 m and a thermal efficiency at 180°C of 62% at DNI levels of $800-850\,W/m^2$[5].

The 1800 Solitem with an aperture width of 1.8 m has a peak optical efficiency of 68%, an efficiency of 58% at 180°C at DNI levels of $800 - 850\,\mathrm{W/m^2}$ [23].

The small size PTC Power Trough 110 by Inventive Power, has an aperture of 1.2 m, a peak optical efficiency of 60% and a thermal efficiency of 45% at 80°C [24].

Trivelli Energia has developed a small PTC, shown in figure 1.8, with an aperture of 1.2 m and a thermal efficiency of 50% at 180°C [25].

Figure 1.8: Small PTC of Trivelli Energia [25].

A small parabolic trough has been tested by Crema et al. [26]; it has an efficiency of 47% at 200°C with a DNI of $880\,\mathrm{W/m^2}$.

It is worth to notice that the efficiency data of the previous PTCs have been provided by groups of research or by companies, then it is not clear through which procedure the results have been obtained. They have not been certified by the Solar Keymark, the third-party certification mark for solar thermal products.

The only parabolic trough of small size present in the database of the Solar

Keymark is the It Collect with an aperture width of 1 m, a peak optical efficiency of 59%, a thermal efficiency of 44% at 180°C with DNI levels of 800 W/m^2 [27].

The objective of this PhD thesis is to design, develop and test a small parabolic trough that could overcome the principal reasons that limits the diffusion of PTC in the market of low-medium temperature heat, increasing the thermal efficiency of the receiver tube and reducing the costs and the complexity of the system.

1.3.1 PTC facilities for process heat

Three alternative design concepts exist for generating the solar steam required by IPH [9]:

- Unfired boiler or heat exchanger (HE). This has a heat transport loop, which delivers hot fluid from the collectors to an unfired boiler or heat exchanger and recirculates the fluid to the collectors through a circulating pump. In this boiler the hot fluid furnishes the heat required to convert feed water into saturated or superheated steam at the required pressure and temperature. The working fluid commonly used in this indirect concept is thermal oil.

- Flash boiler (FB). This is another indirect process in which the water from the flash boiler is pressurized and circulated through the solar field and heated to a temperature between 180 and 200°C. The water is pressurized and maintained at the required pressure by a circulating pump to prevent boiling within the collectors or the field piping. When the heated water from the collector field enters the boiler flash chamber, due to the change in pressure in the vessel, a part of it is converted into steam, which is delivered to the steam mains of the industrial process. The rest of the water is recirculated through the collector field. Make-up water is fed from the storage tank. Flashing is up to about 4–6%, depending on the temperature of the heated water.

- DSG. This is a direct system, in which the water is partially or completely boiled in the collector. In the first case, water is circulated through a steam drum where steam is separated from the water. Feed water is added to the steam drum or mixed with the recirculated water at a rate regulated by a

level controller in the drum. In the second type, feed water is added directly to the collector field inlet.

Several systems with PTC for the production of heat at low-medium temperature have been built in the recent years around the world. The group of research of professor De Lucia, to which I belong, has realized a solar PTC field in Catania, Sicily for the production of heat at medium temperature (figure 1.9).

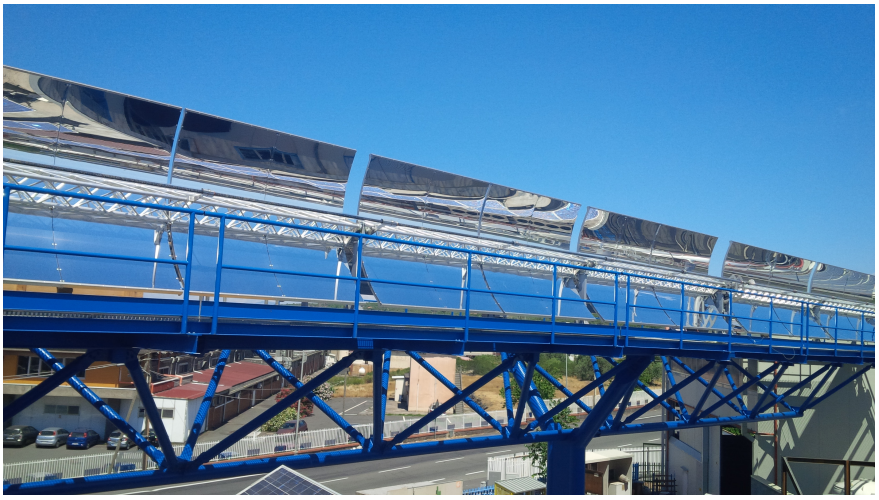

Figure 1.9: PTC installation in Catania realized by the University of Florence.

The features of some facilities are reported in table 1.2. In figure 1.10 a PTC facility for process heat in Mexico.

For the importance of the project, it is necessary to mention the Miraah solar plant in Oman though it is characterized by a large availability of land and therefore very different from typical PTC installation in industrial environments. The plant, that has started operation in February 2018, has a total capacity of 100 MWth and delivers 660 tons of steam per day to the Amal oil field located in the south of the Sultanate of Oman. The steam is used for the extraction of viscous or heavy oil as an alternative to steam generated from natural gas. Once complete the plant will be the world's largest solar process heat system (1 GWth installa-

tion). At this plant the parabolic trough collectors and other system components are indoors, using a green house structure to protect from wind and sand, which is common in remote oil fields like Amal. The green house enables major cost and performance advantages compared to exposed solar designs, from reducing over all material usage to automated washing operations [5].

Table 1.2: Process heat facilities with PTCs around the world [28].

Location	Company or institution	Year	Solar collector	Aperture area $[m^2]$	Fluid/steam generation concept	Application	Process Temp. $[^{\circ}C]$
Modesto (USA)	Frito-Lay Inc.	2008	IST-PT1	5065	Press. Water/HE	Oil heating to fry potato and corn chips	249
Tuba City (USA)	DOE	2009	IST-PT1	160	Press. Water/HE	Distillation of contaminated water	–
El Nasr (Egypt)	New and Renewable Energy Authority	2004	IST-PT1	1900	Press. Water/FB	Steam production for pharmaceutical chemicals	173
Brazil	Kraft Food	2012	IST-PT1	633	Press. Water	-	110
Engadin (CH)	Lesa Dairy	2011	PolyTrough 1200	115	Thermal oil	Dairy products	200
Saignelégier (CH)	Emmi Dairy	2012	PolyTrough 1800	627	Press. Water	Dairy products	180
Cesar (PT)	Silampos	2014	S10	450	Thermal oil	Process Wash and Drying	180
Jalisco, (MX)	Nestle Dairy Plant	2014	Power Trough 110	245	Water	Dairy products; Pasteurization, heating water	95

Figure 1.10: Application of parabolic trough collector in a dairy processing plant in Mexico [24].

1.4 Parameters of PTC

The parabolic trough, is a trough the cross-section of which has the shape of a part of a parabola. More exactly, it is a symmetrical section of a parabola around its vertex. Parabolic troughs have a focal line, which consists of the union of focal points of the parabolic cross-sections. Radiation that enters in a plane parallel to the optical plane is reflected in such a way that it passes through the focal line [29]. The equation of a parabola is:

$$y = \frac{x^2}{4f} \tag{1.1}$$

In order to describe a parabolic trough geometrically, the section of the parabola that is covered by the mirrors has to be determined. Three parameters are commonly used to characterize the form and size of a parabolic trough (figure 1.11): the trough focal length, the aperture width, i.e. the distance between one rim and

the other, and the rim angle, i.e. the angle between the optical axis and the line between the focal point and the mirror rim [29].

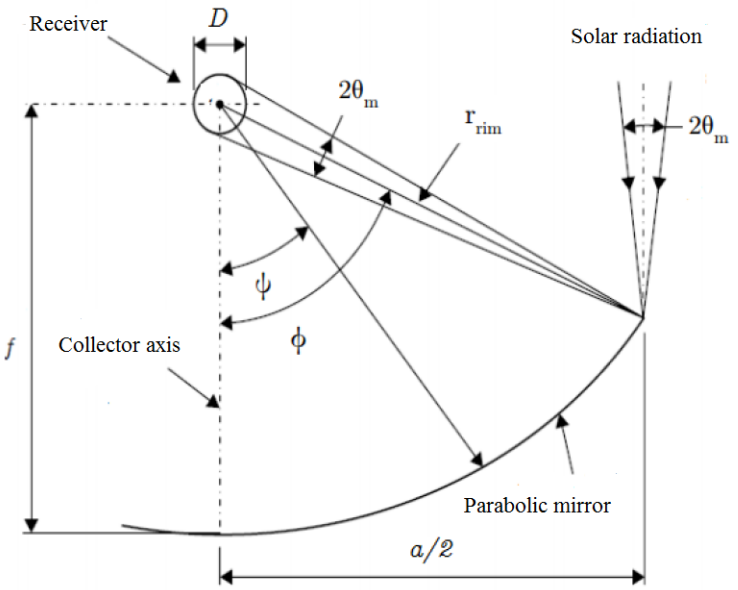

Figure 1.11: Main geometrical parameters of parabolic mirror. Adapted from [12].

Two of the three parameters rim angle, aperture width and focal length are sufficient to determine the cross-section of a parabolic trough completely, i.e. shape and size. This also means that two of them are sufficient to calculate the third one ϕ can be expressed as a function of the ratio of the focal length to the aperture width:

$$\frac{f}{a} = \frac{(1+\cos\phi)}{4\sin\phi} \tag{1.2}$$

The aperture area of the collector is an important constructive measure since at a given DNI and Sun position, it determines the radiation that can be collected.

The aperture area is calculated as the product of the aperture width and the collector length :

$$A_c = a \cdot l \tag{1.3}$$

The concentration ratio is one of the central parameters of the collector. It determines the range of temperatures that the parabolic trough collector can reach. The geometrical concentration ratio GC is defined as the ratio of the collector aperture area to the receiver aperture area:

$$GC = \frac{a \cdot l}{\pi \cdot D \cdot l} = \frac{a}{\pi D} \tag{1.4}$$

In literature, another definition for the concentration ratio is also present; it is the ratio between the projected area of the aperture and the projected area of the tube:

$$GC = \frac{a}{D} \tag{1.5}$$

In the present work, it is used the former definition (ratio between areas).

1.5 Components of PTC

The parabolic trough collector is composed by the parabolic mirror, the receiver tube where a heat transfer fluid flows and the bearing structure.

1.5.1 Mirrors

The main requirements for appropriate mirror materials are their reflective properties. Reflection is distinguished in specular reflection and diffuse reflection. Specular reflection means that the light that comes from a single incoming direction is reflected into a single outgoing direction. According to the law of reflection the direction of the incoming light and the direction of the outgoing light have the same angle with respect to the mirror surface normal. In CSP applications, only

specular reflectivity is of interest, because the reflected radiation must have a defined direction [29]. The decisive quality criterion for efficient mirrors is, hence, the "solar weighted specular reflectivity"; this parameter describes the quantity of the specular reflectivity of the mirror in the solar spectral range (fig. 1.12).

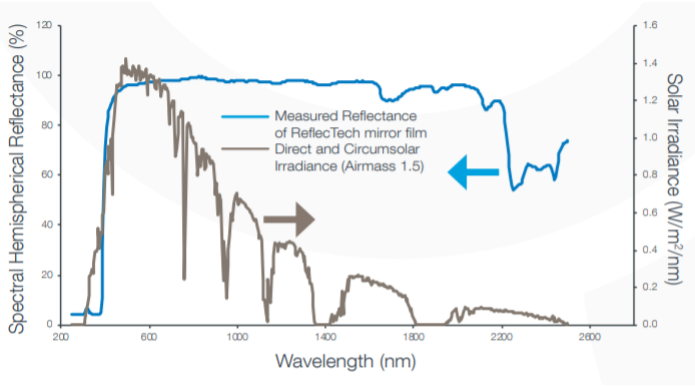

Figure 1.12: Spectral reflectance of a mirror for solar applications [30].

The most common mirrors for PTC today consist in back-silvered glass mirrors [29]. The average solar weighted specular reflectivity of a good silvered glass mirrors is about 94-96%. Polished aluminum mirrors have a lower value of reflectance compared to glass mirrors (88-90%) and less durability.

1.5.2 Receiver

The receiver aims to convert solar radiation into heat. For this reason the receiver tube has to fulfill physical and geometrical requirements. Indeed, solar energy has to be absorbed as completely as possible and optical and thermal losses at the surfaces of the receiver components should be minimized. Furthermore, a large amount of radiation reflected by the parabolic mirror should reach the absorber surface, which implies precise geometric constraints.

The receiver is composed by an absorber tube and by a cylindrical glass cover which protects the absorber from the outside environment. The annulus between the absorber and the glass, is evacuated ($< 10^{-4}$ mbar) so that the convective and

conductive heat losses are reduced further (fig. 1.13). Generally a getter is present to prevent the loss of the vacuum inside the cavity and to absorb the hydrogen generated by the absorber.

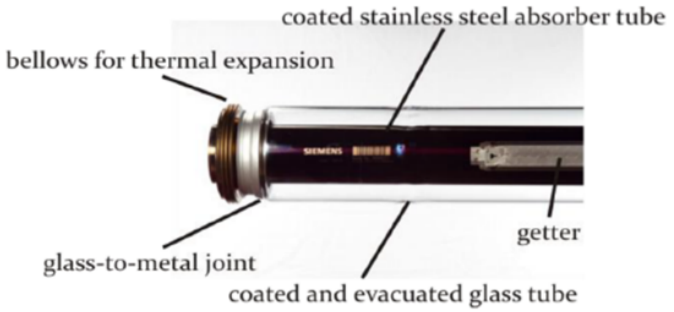

Figure 1.13: Features of the receiver tube [29].

The glass tube, made out of borosilicate glass, has to possess high transmittivity in the visible spectral range. For this reason a special antireflective coating is deposited on it to guarantee value of transmittivity of 96%. Moreover, the glass has quite a low transmittance in the infrared range. This contributes slightly to the insulation effect because a part of the emitted thermal radiation of the absorber tube is maintained in the system: it heats the glass, reduces thereby the convective heat loss from the absorber to the glass tube and generates additional thermal radiation back onto the absorber tube (which, however, is hardly absorbed because of the selective coating).

The absorber tube is generally made by steel AISI 304 or AISI 316. Special coatings are applied on the absorber tube to maximize absorption and minimize heat losses. In order to reach high radiation absorption and a low radiative heat losses, the absorbance of the coating must be high in the solar spectral range ($0.1\,\mu m \leq \lambda \leq 2.5\,\mu m$) and the emissivity must be low in the infrared range ($\lambda \geq 2.5\,\mu m$), as shown in figure 1.14). A coating which possesses this property is called a selective coating.

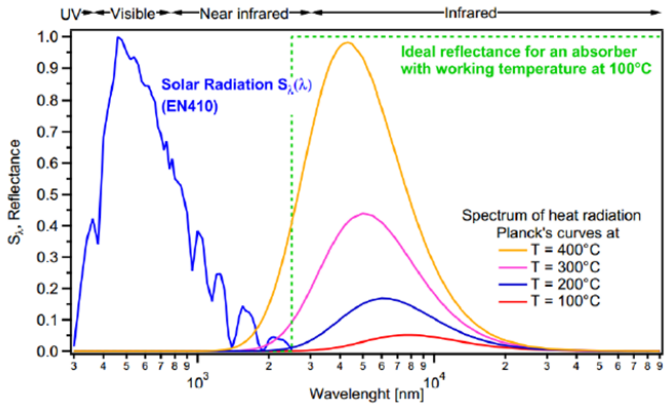

Figure 1.14: Solar and black body spectrum for different temperatures [31].

Selective coatings for the absorber tubes are generally realized with cermet, a material that consists of metallic nano-particles that are embedded in a ceramic matrix [29]. More exactly, the coating consists of different layers. First, there is a reflection layer made out of a metal that is highly reflective in the infrared range, for instance copper, aluminium or molybdenum. Second there is the cermet layer, which itself can be divided into different layers with higher and lower metal content. The cermet layer consists of an oxide like Al2O3 or SiO2 and a metal like molybdenum. The antireflection ceramic layer consists of oxides like Al2O3 or SiO2. Additional adhesion layers are introduced that guarantee the adhesion of the functional layers on the structural tube material. The cermet coating of the Archimede solar energy tube has an absorbance of 0.95 and an emissivity of 0.10 at 550°C. The higher the temperatures are, the more difficult is the design of an efficient selective coating because there is a larger overlap of the thermal emission spectrum and the solar spectrum. Already at 400°C there is a non-negligible spectral overlap in the range of 1500 to 2500 nm as can be seen in figure 1.14.

For what concerns the receiver size, the diameter of the absorber tube must be big enough to guarantee that a high fraction of the radiation reflected by the mirror hits the absorber surface. This information is contained in a parameter called intercept factor; it should be close as possible to 1. On the other hand, the

absorber diameter should not be too large in order to have a high concentration ratio and thus, low thermal losses.

The minimum diameter the absorber must have to intercept all the radiation reflected by the mirror is:

$$D_{min} = \frac{a \sin(\sigma_{tot})}{\sin(\phi)} \tag{1.6}$$

where a is the aperture width of the mirror, σ_{tot} is the result of the root sum square of solar divergence and optical errors, ϕ is the rim angle.

1.5.3 Heat transfer fluid

The heat transfer fluid (HTF) has the task to accumulate the thermal energy in the collectors and to transport it to the power block or to the energy storage. The properties of the HTF deeply influence the performances of the system: the HTF determines the maximum temperature at which energy is delivered and the efficiency of the thermodynamic cycle associated, if the PTC is used to produce power. Moreover, it establishes the optimum flow rate, the pressure loss in pipes and the operating pressure [29].

The HTF has to fulfill certain requirements. It must be liquid, that means that it should have a sufficiently high evaporation temperature (under manageable pressures) so that it is not evaporated under the high temperatures that are reached in the solar field. Additionally, low freezing temperatures are an advantage so that no freezing protection measures are necessary if the temperatures in the solar field get low. It is also important that its thermal stability is sufficient to stand the high operation temperatures (no thermal cracking, for instance). Evaporation temperature and thermal stability determine the maximum operation temperature of a HTF. In order to store and transport high amounts of thermal energy, a high specific heat capacity is useful. Also high heat conductivity is advantageous for quick heat transfer processes. Low viscosity is important to reduce pumping energy [29].

Nearly all parabolic trough power plants use synthetic thermo oil as HTF that has a maximum temperature of 385°C. Currently efforts are done to use molten

salt as HTF that have a maximum temperature of 550°C. An experimental facility that uses molten salts as HTF has been set up in Italy, in Sicily designed by ENEA (Archimede combined cycle power plant).

For applications for production of heat at low and medium temperature (50-250°C), oil and pressurized water are used.

Besides, water is an extraordinary HTF: it has excellent heat transfer properties (high heat capacity, low viscosity), it is non toxic, inexpensive. The drawbacks are: low boiling point at ambient pressure and so it is necessary to pressurize it; high freezing point. To avoid freezing, ethylene and propylene glycol are added to water. These mixtures provide effective freeze protection as long as the proper antifreeze concentration is maintained. The glycol-to-water ratio needed depends from the environmental temperature. At our latitudes, it is enough a glycol/water mixture 20/80. It can also be corrosive if the pH (acidity/alkalinity level) is not maintained at a neutral level. Water with a high mineral content (i.e., "hard" water) can cause mineral deposits to form in collector tubing and system plumbing [29].

Another possibility is represented by using water steam as HTF (direct steam generation).

1.5.4 The bearing structure

The bearing structure of a parabolic trough has the function to carry the mirrors in the right position, to give stability to the troughs and to allow an exact Sun tracking [29]. In order to comply with these functions, the structures have to fulfill some construction requirements. In particular, the stiffness requirements are very high, because any deviation from the ideal parabolic collector shape causes losses in the optical efficiency of the system. It is important that the parabolic troughs are neither deformed by their own weight nor by wind loads. The aperture area represents a large area that is exposed to the wind so that the resulting wind loads are considerable. The collector has to be constructed in such a way that it withstands these loads with only very small geometrical deviations.

1.6 Theory of PTC

The solar radiation that arrives on the ground directly from the sun disc, without being scattered by the atmosphere, is called beam irradiance or direct irradiance. The diffuse irradiance is the fraction of the sun radiation that has undergone scattering processes through the atmosphere and so it has no defined directions. The sum of the beam and the diffuse solar irradiance is called global irradiance[32].

Direct Normal Irradiance (DNI) is defined as the amount of direct irradiance received by a surface that is always held normal to the rays that come in a straight line from the direction of the sun at its current position in the sky.

The relation between the global horizontal irradiance (G_H), DNI (G_b) and diffuse horizontal irradiance ($G_{d,H}$) is described by:

$$G_H = G_b \cdot \cos\theta + G_{d,H} \tag{1.7}$$

where θ is the incidence angle between the normal of the surface and the direction of sun rays.

Parabolic trough can only use direct irradiance since diffuse radiation having random direction can not be focused. For this reason, PTC must track the sun along at least one direction.

The peak or maximal optical efficiency represents the maximum performance that a PTC can reach and it is an important parameter that must be measured when performing a PTC characterization. The value can be analytically derived multiplying the mirrors reflectance ρ, the absorptance of the absorber tube α, the transmittance of the receiver glass envelope τ and the intercept factor γ_0 (that represents the fraction of solar rays that actually reaches the receiver) [29]:

$$\eta_{opt\,0} = \rho \cdot \tau \cdot \alpha \cdot \gamma_0 \tag{1.8}$$

The peak optical efficiency can be evaluated experimentally as the ratio of the radiant solar power absorbed by the receiver to the direct normal irradiance on the aperture area when there are no heat losses, i.e. the temperature of the absorber is very close to ambient temperature, and the incident angle of solar rays is equal to 0° (condition of normal incidence):

$$\eta_{opt\,0} = \frac{\dot{Q}_{abs}}{\dot{Q}_{sun}} = \frac{\dot{Q}_{abs}}{DNI \cdot A_c} \tag{1.9}$$

When the incident angle is not zero $\theta \neq 0$, the optical efficiency decreases. This is described by:

$$\eta_{opt}(\theta) = \eta_{opt\,0} \cdot \cos(\theta) \cdot K(\theta) \cdot \eta_{end} \cdot \eta_{sh} \cdot \eta_{clean} \tag{1.10}$$

The term in $\cos\theta$ accounts for the reduction of irradiance collected by the surface when the normal vector of the surface is not parallel to the direction of sun rays; this effect is called cosine effect.

The $K(\theta)$ term, called incidence angle modifier (IAM), describes the optical collector losses that depends on the incidence angle θ, as for instance the decrease of optical properties (ρ, τ, α) with the incident angle, the dependence of the intercept factor by the incidence angle due to the rise of optical errors, etc.. The terms η_{end} called end losses, accounts for the reduction in optical efficiency due to the fact that at one end of the trough the absorber tube is not illuminated by the reflected radiation since the incident sun rays are oblique; η_{sh} accounts for the losses due to shading and η_{clean} due to the soiling of the mirrors. Figure 1.15 shows the parameters that influence the performances of a PTC.

The thermal efficiency of the collector is defined as the useful heat per second delivered to fluid to sun irradiance on the aperture area. The useful thermal power is obtained by the difference between the thermal power absorbed by the absorber tube and the heat losses of the absorber:

$$\eta_{th} = \frac{\dot{Q}_u}{\dot{Q}_{sun}} = \frac{\dot{Q}_{abs} - \dot{Q}_{loss}}{\dot{Q}_{sun}} = \eta_{opt}(\theta) - \frac{\dot{Q}_{loss}}{\dot{Q}_{sun}} \tag{1.11}$$

For an evacuated receiver under high vacuum ($< 10^{-4}$ mbar), convective losses are close to zero and only radiative losses are present:

$$\eta_{th} = \eta_{opt}(\theta) - \frac{\sigma_B \left(T_{abs}^4 - T_{glass}^4\right)}{GC \cdot DNI \cos(\theta) \left(\frac{1}{\varepsilon_{abs}} + \left(\frac{(1-\varepsilon_{glass})}{\varepsilon_{glass}} \frac{A_{glass}}{A_{assb}}\right)\right)} \tag{1.12}$$

where T_{abs}, T_{glass} are the absorber and glass temperature, σ_B is the Stefan-Boltzmann constant, $\varepsilon_{abs}$and ε_{glass} are the emissivity of the absorber and of the glass, $A_{abs}$and A_{glass} are the surfaces of the absorber and of the glass. As can be seen thermal efficiency rises if GC grows and if the irradiance grows.

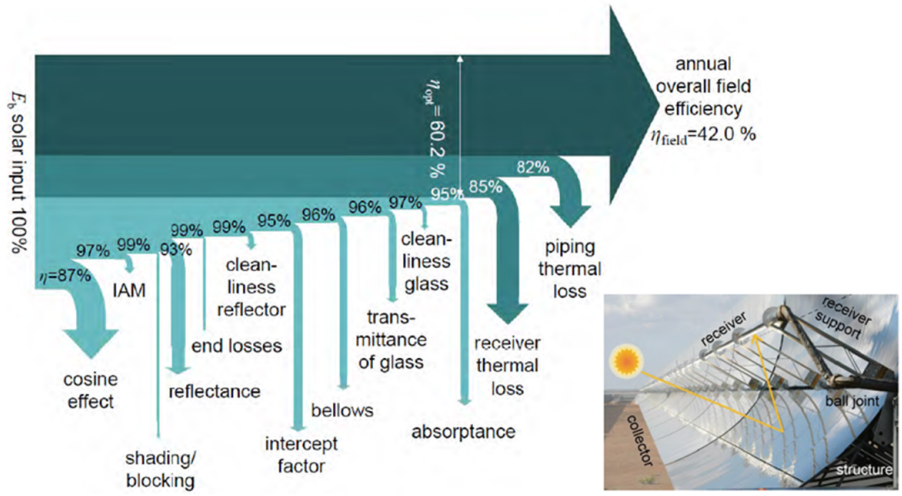

Figure 1.15: Parameters affecting performances of PTC collector.

The experimental thermal efficiency of the collector, for an incident angle of 0°, is the ratio of useful power absorbed by the fluid that flows in the receiver and incident solar power on the area of the collector:

$$\eta_{th} = \frac{\dot{m} C_p (T_{out} - T_{in})}{A_c DNI} \tag{1.13}$$

where C_p has to be evaluated at medium temperature of the fluid.

1.7 Test on PTC

Two kind of test are possible for concentrating collectors: the steady or quasi steady state test and the quasi-dynamic test. There are several standards about test on solar thermal collectors that are applied to concentrating collectors, EN 12975-2 [33], ASTM E905-87:2013 [34], SRCC 600:2010 [35], ASHRAE 93[36], ISO 9806:2013 [37] but there is no uniformity about operating conditions [16] and permitted deviations of variables.

One of the earliest is the European standard EN 12975:2006 and although this standard did not include in its scope the testing of concentrating and/or tracking collectors, it was employed in the past by research institutions for testing PTCs and even by the well-known Solar Keymark organization for certification purposes. The standard ASTM E905-87:2013 [34] is specifically devoted to tracking concentrating solar collectors. Following the same approach, the American standard SRCC 600:2010 [35] is also valid for solar concentrating collectors and is actively being used by developers in the United States for certifying PTCs. The lately published international standard ISO 9806:2013 (recently updated in ISO 9806:2017), does include tracking concentrating collectors in its scope [16].

The steady-state (or quasi steady) test has to be performed only with clear sky and prescribes that all important variables for the thermal characterization of a collector have to remain constants throughout the test period. The oscillations of solar radiation incident on the collector, inlet temperature of heat transfer fluid, mass flow rate and ambient temperature should be within certain limits defined by [33, 37, 34, 36]. This is required to ensure valid results since measurements for determining the rate of heat gain are made simultaneously at the inlet and outlet of the collector and hence not on the same element of fluid. Indeed, it has been verified [38, 39] that, if fluctuations for fluid temperature, mass flow and irradiance exceed the deviations prescribed, wrong results are obtained and the outcomes are not repeatable from day to day.

There is an additional important stability requirement for the data averaging period: should not be present a trend of temperatures (or flow rates) toward higher or lower values, which would indicate that energy is being stored in (or removed from) the mass of the test system and thus the system is not in thermal equilibrium.

Other prescriptions limit the percentage of diffuse radiation and the wind

speed over the collector.

It is worth to notice that several interferences can invalidate the results [34], even if the test bench has been carefully designed to meet the strict requirements of stationary test:

- alignment error, tracker pointing error, and the distorting effects of wind and gravity on the reflector and receiver may contribute to decreased thermal performance by decreasing the fraction of solar radiation incident on the collector aperture that strikes the absorber. The degree to which these errors affect collector thermal performance depends on the incident angle to the collector and the limits of the tracker, collector position and orientation relative to wind direction, wind speed, structural integrity of the collector and its support system, and so forth. Warping and sagging of the reflector due to heat have been observed, particularly in the case of linear trough concentrating collectors, also causing a decrease in the ability of the concentrator to direct the incident solar radiation to the absorber. Thermal expansion of the receiver may also occur under operating conditions of concentrated solar energy, and could cause damage to the receiver or the seals, possibly resulting in increased heat losses.

- Soiling of the collector surfaces (reflector/refractor, absorber cover, etc.) may effectively reduce the solar energy available to the collector, in a way that is neither quantifiable nor reproducible.

- Small variations in the level of solar irradiance during testing may cause considerable difficulties in maintaining quasi-steady state.

- Variations in the quality of the direct irradiance, comprising solar and circumsolar radiation, may give rise to irreducible fluctuations in the thermal performance because the angular responses of the collector and of the pyrheliometer differ.

- Variations in the level of diffuse irradiance may affect the measured thermal performance, particularly for lower concentration ratio collectors. Therefore total (global) solar irradiance measurements are to be made to indicate

the conditions under which the tests are performed, and to allow comparisons to be made with available meteorological data.

According to the ASTM E905-87, testing conditions must exist for a time period equal to two times the response time (which must be calculated for each collector as indicated in the standard) before each test, and for the duration of each test, which shall be the longer of 5 min or one-half the response time. The response time is defined as the time required for ΔT to increase to 90% of its value under quasi-steady state conditions after the shaded collector at equilibrium is exposed to irradiation [16].

The aim of the test is extracting the efficiency curve of the collector for normal incidence and its parameters η_0,$a_1$and a_2 [40]. The use of sun-tracking devices allows testing under these conditions, regardless of the position of the sun (time of day). There are also experimental procedures to obtain the angular dependence of the optical performance, called the incidence angle modifier $K(\theta)$, and the effective thermal capacity.

The heat balance equation that can be written on the basis of the steady state method is (SST):

$$\frac{\dot{Q}}{A_c} = \eta_0 K(\theta) \cdot G_b - a_1 (T_m - T_a) - a_2 (T_m - T_a)^2 \tag{1.14}$$

where T_m and T_a are the medium temperature of the fluid and the ambient temperature.

In this model there is no correction term for the diffuse radiation, which is usually required in simulation programs for the long-term behavior of collectors. This is due to the fact that this is a clear-sky model (low percentage of diffuse radiation) [40].

The quasi-dynamic method derives from the steady-state model by adding some correction terms that allow a more detailed description of the collector. Solar radiation is considered in its two components, direct and diffuse, with corresponding IAMs. The dependence on wind speed is modeled by two corrective terms, the effect of the wind on the optical performance and its influence on heat

losses. Finally, the last correction describes the dependence of losses due to radiation of long wavelength incident on the collector. The net power provided by a collector, according to the quasi-dynamic model, is given by equation [37]:

$$\begin{aligned}\frac{\dot{Q}}{A_c} =& \eta_{0,b} K_b(\theta_L, \theta_T) \cdot G_b + \eta_{0,b} K_d \cdot G_d - c_6 \cdot u \cdot G - c_1 \cdot (T_m - T_a) + \\ & - c_2 \cdot (T_m - T_a)^2 - c_3 \cdot u \cdot (T_m - T_a) + c_4 \cdot \left(E_L - \sigma_B T_a^4\right) - c_5 \cdot \frac{dT_m}{dt}\end{aligned} \tag{1.15}$$

where $K_b$and K_d are the IAM for beam and diffuse component, u is the wind velocity.

The quasi-dynamic test has different duration respect than the quasi steady test. Each test sequence should extend for at least 3 h. At least one of the test sequences should be performed under varying sky conditions, with periods of clouds and clear sky for the correct determination of the thermal capacity. Test data sets must be obtained for at least four fluid temperatures at the entrance at regular intervals over the operating range of the collector [40].

In table 1.3 are reported the requirements imposed by the standards; as can be seen the fluctuations of the variables permitted by the quasi dynamical methods are less strict than steady state test.

Table 1.3: Values and permitted deviations for quasi-steady state and quasi-dynamic state. Adapted from [16].

Variable	ASTM E905-87 Quasi-steady		ISO 9806 Quasi-dynamic	
	Value	Deviation	Value	Deviation
$DNI\left[W/m^2\right]$	>630	$<\pm 4\%$	-	-
$T_{amb}[^\circ C]$	-	$<\pm 2.0$	-	-
$T_{in}[^\circ C]$	-	$<\pm 0.2$	-	$<\pm 1.0$
$\dot{m}[\%]$	-	$<\pm 1.0$	-	$<\pm 2.0$
$vwind\ [m/s]$	<4.5	-	-	<4.0

In literature several test on parabolic trough collectors are reported.

Dudley et. al. [38, 39] performed test on LS-2 and IST collectors using a rotating platform at Sandia National Laboratories. The platform rotates around the vertical axis allowing azimuthal tracking, while the PTC track the elevation of sun; in this way a 2-axis tracking system is realized. It allows to perform test under zero incidence angle condition. The results of the test were elaborated following the steady state method. Several typology of receiver tubes and of different coating were tested.

Fischer et. al. [41] report test on a parabolic trough collector using the quasi dynamic method.

Janotte et. al. performed the characterization of a small size PTC (width of 1.8 m) through stationary method and quasi dynamic method [23]. The results between the two methods are in good agreement.

Larcher et. al. [42] presented the experimental test on a small size PTC with an aperture width of 1.845 m using the steady state method.

A test bench rotating platform, shown in figure 1.16, to test PTC module has been developed by DLR at Plataforma solar de Almeria (PSA). The test bench allows the qualification of all collector components and complete modules of a length of up to 20 m. It is designed to asses large sized PTCs with aperture width of around 6m. The goal of the test bench is reaching a total accuracy on the performance measurements of the module of 2-3 % [43]. It is stressed that the measurement of temperature is highly critical; for this reason, the measurements of inlet and outlet temperature are performed through 3 RTDs that have been calibrated simultaneously.

Fernandez et. al. [16] presents the development of a solar thermal test loop to assess the performance of small-sized parabolic-trough collectors (PTC).

Figure 1.16: Kontas rotating platform at PSA [43].

Chapter 2

The design of the m-PTC

The aim of the project is to design, build and test a compact concentrating collector, called m-PTC (micro-PTC), suitable to be installed on the roof to produce heat at low-medium temperature (up to 250°C) for process heat applications or other applications (absorption cooling). An accurate design phase has preceded the construction of a prototype.

A numerical analysis from an optical and thermal point of view has been conducted.

The design of the small size parabolic trough collector has started with the optical analysis of the collector that has allowed to choose the optimum values for the parameters of the parabola, aperture and rim angle.

2.1 Optical analysis

In order to have a compact, transportable object, suitable to be installed on a commercial/residential roof, the aperture width should be fixed equal or less than 1 m.

Therefore, a design process on the receiver tube is needed since the standard absorber tubes for parabolic trough are characterized by a diameter of 70 mm. Using the standard tube together with a mirror aperture width of 1 m, it would lead to a very low concentration ratio (about 4).

The diameter of the receiver has been selected as a trade-off between concentration ratio and minimum acceptable dimensions. Furthermore, it is not practical to employ tubes with a too small diameter (under 2 mm) because this would cause a high pressure drop for the reference mass flow of the solar thermal collectors ($0.02\,kg/(m^2s)$). For these reasons, the aperture has been fixed to about 0.5 m and the external diameter of absorber tube has been set, as first attempt, to 10 mm leading to a concentration ratio of 16. The optical analysis aims to verify if the tube diameter is adequate to intercept the radiation reflects by the mirror.

The rim angle of the parabola has to be determined. From literature [44], fixed the optical errors and the concentration ratio, the optical efficiency of the collector strongly depends on rim angle. For example in the ideal case (no optical errors), the rim angle that maximize the optical efficiency is 90°. In the real case, where optical errors are present, and for a concentration ratio < 20, optical efficiency is maximum for a rim angle $> 90°$. Moreover, a high rim angle has the advantage that reduces the focal length and make more stable the structure. A diameter of 10 mm and a rim angle of 90° should be in theory able to intercept the radiation included in half angle of about 1.4° as can be verified inverting equation 1.6.

An optical analysis with the open source Monte Carlo ray tracing software developed by NREL, Soltrace [45], has been conducted in order to select the rim angle of the parabola and to evaluate the optical efficiency. The angular width of the sun and the optical errors (micro and macro imperfection of the parabola, receiver tube misalignment, errors due to tracking) have been estimated and applied in the analysis.

Aluminium mirror has been considered more suitable than glass mirror for the shape of parabola selected because of its bending resistance. Indeed only ultra thin glass ($0.1 - 0.2$ mm) could have enough bending resistance for this curvature radius [46]. Furthermore, the aluminum mirror is less expensive. For an aluminum mirror, the slope and specularity errors could be estimated to be about 0.8° on the half angle [47]. For what concerns the misalignment errors, it is expected to place the absorber tube with an error of about 1 mm maximum around the focus point. Since the receiver tube could move away from its original position, due to thermal stresses and external forces (wind loads, etc.), a random error is added to the initial systematic error of misalignment, and thus the misalignment can be treated as a statistical error. The error of misalignment has been estimated to be

about maximum 0.2°. For what concerns the tracking error, the tracking sensor developed inside the group of research has an error $< 0.1^\circ$. Finally it has to be considered the solar beam angle, i.e. the opening angle of the direct solar radiation seen from the Earth. The beam spread of the radiation is 0.27°.

The total error for the half angle is [48]:

$$\sigma_{tot} = \left(\sigma_{sun}^2 + \sigma_{optical}^2\right)^{\frac{1}{2}} \cong 0.87^\circ \tag{2.1}$$

Analytically, using equation 1.6, it turns out that a diameter of 13 mm is able to intercept the 95% (2σ) of the radiation reflected by the mirror for a rim angle of 90°. This result has to be checked through the numerical analysis.

The model realized in Soltrace deals with the parabolic mirror, the cylindrical absorber tube and the cylindrical glass tube. The optical errors have been applied to the surface of the mirror. Several shapes of the parabolic mirror (i.d. different rim angles) have been evaluated.

In figure 2.1, is reported the optical efficiency varying the rim angle of the parabolic mirror for different values of the diameter of the absorber tube. The optical errors are fixed to $\sigma = 0.9^\circ$. As can be seen, for a tube diameter $< 10\,mm$ low values of optical efficiency are obtained, especially for rim angle $< 90^\circ$. The value of the rim angle influences the optical efficiency of the collector: increasing it, higher values of optical efficiency are reached. For absorber diameter of $15\,mm$ and $20\,mm$, compared to $10\,mm$ diameter, there are little advantages in terms of optical efficiency while higher thermal losses are expected since the concentration ratio decreases. For these reasons, a rim angle of 100° has been fixed for the parabola.

The selected configuration and the properties of the materials are reported in table 2.1.

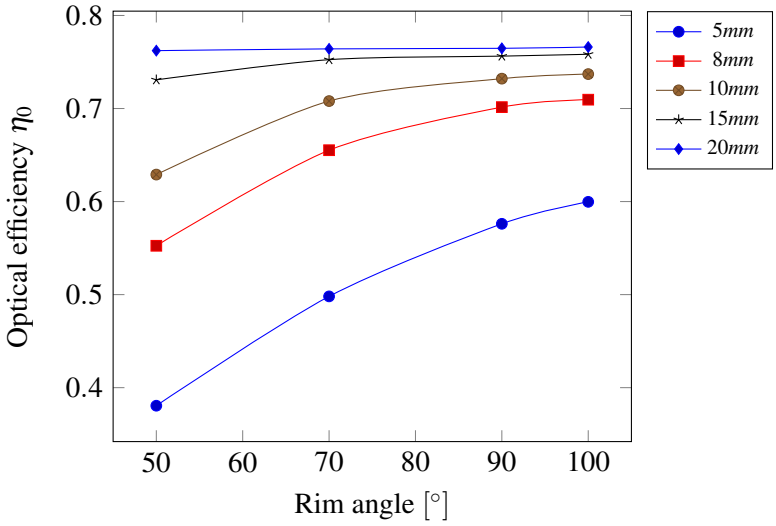

Figure 2.1: Optical efficiency varying the rim angle of the parabola for $\sigma = 0.9°$.

Table 2.1: The features of the small parabolic trough collector.

Features of collector	
Aperture	$420\,mm$
Rim angle	100°
Focal	$83.9\,mm$
Absorber external diameter	$10\,mm$
Glass external diameter	$30\,mm$
Length	$1.8\,m$
Concentration ratio	13.73
ρ	88%
τ	95%
α	95%

The optical efficiency is determined by the shape of the parabola and of the properties of materials. The latter are a trade-off between good performances and

low costs. The optical efficiency estimated is about 73%. The intercept factor is 92%, confirming the rough analytical estimation.

Figure 2.2 shows the irradiance distribution on the absorber tube. As can be seen, the irradiance distribution is symmetrical. Furthermore, along the circumference of the absorber tube the irradiance is non uniform, since the upper part of the receiver, corresponding to the positions close to 0.015 m and -0.015 m on the horizontal axis in the plot, receives only direct radiation, while the lower part of the absorber tube is hit by the radiation reflected from the mirror. The location of the maximum of irradiance along the absorber is around at 50° respect the bottom of the tube and the peak of irradiance is 11 kW/m^2 for a DNI of 1000 W/m^2.

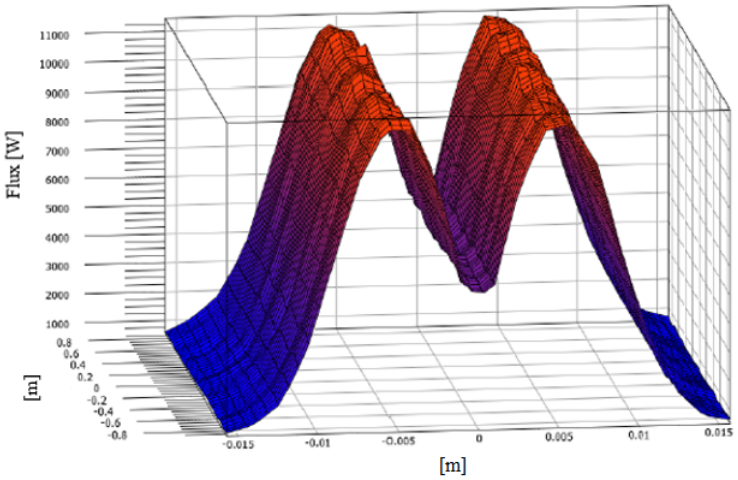

Figure 2.2: Solar flux distribution on the absorber surface, from Soltrace.

In figure 2.3 is reported how varies the optical efficiency changing the transversal angle of incidence on the aperture plane. It can be seen that optical efficiency for quite large transversal incidence angle (1.5°) remains high, about 90% of the peak optical efficiency. Due to the value of the rim angle selected, the collector guarantees high performances far from the conditions of ideal tracking (transversal incidence angle equal to zero). This behavior is very interesting since several uncertainties could arise experimentally, such as the change of the shape of the

parabola due to stress, and could cause an increase of the errors on the transversal plane.

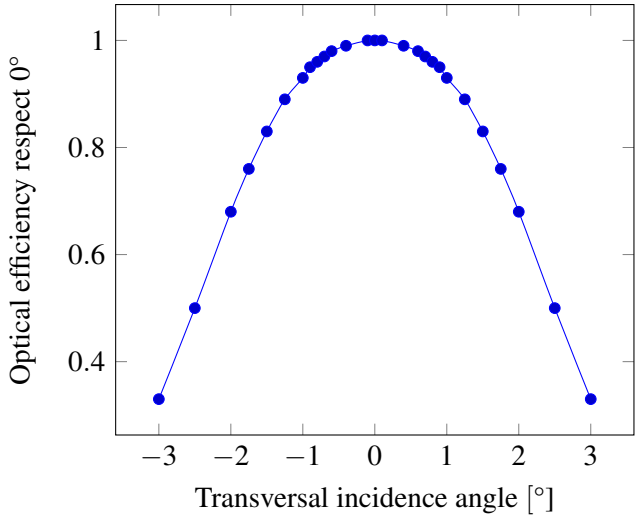

Figure 2.3: Optical efficiency versus trasversal angle of incidence.

An important parameter is the incidence angle modifier (IAM) that describes how the optical efficiency of the collector varies with the angle of incidence. Through Soltrace it has been evaluated. In table 2.2 it has been reported the IAM, the end losses calculated through Soltrace, the end losses evaluated analytically and the length of the collector that is not irradiated. Since the focal length of the mirror is very small, the IAM presents values close to unity also for high angles of incidence. As can be observed the end losses obtained by Soltrace are in good agreement with the analytic results.

Table 2.2: Results of optical efficiency, Iam, end losses calculated through Soltrace, end losses derived analytically, lenght of the collector shadowed.

$\theta[°]$	$\eta_{opt.}[\%]$	IAM	$\eta_{end,Soltrace}$	$\eta_{end,an}$	$L_{end}[m]$
0	73.35	1.0	1.00	1.0	0.000
5	73.36	1.0	0.99	0.99	0.011
10	73.30	1.0	0.99	0.99	0.022
15	73.22	1.0	0.98	0.98	0.033
20	73.01	1.0	0.98	0.97	0.045
25	72.79	0.99	0.97	0.97	0.058
30	72.38	0.99	0.96	0.96	0.071
35	71.89	0.98	0.95	0.95	0.087
40	71.06	0.97	0.94	0.94	0.104
45	69.84	0.95	0.93	0.93	0.124
50	68.06	0.93	0.92	0.92	0.147
55	65.37	0.89	0.90	0.90	0.177
60	61.47	0.84	0.88	0.88	0.214

Figure 2.4 shows the behavior of Iam; in figure 2.5 the end losses of the collector are reported.

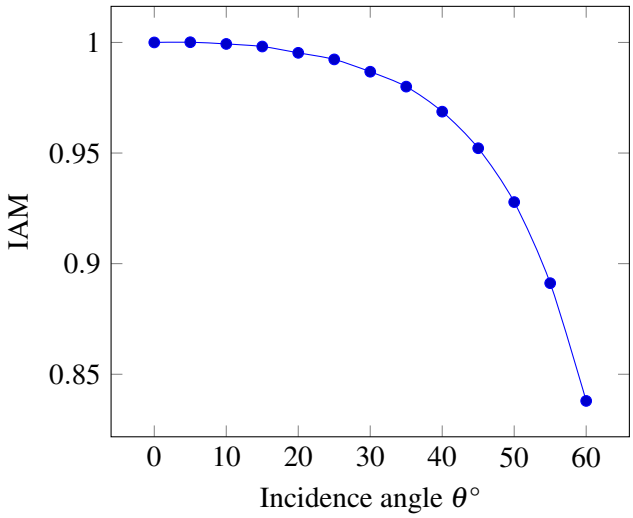

Figure 2.4: Incidence angle modifier.

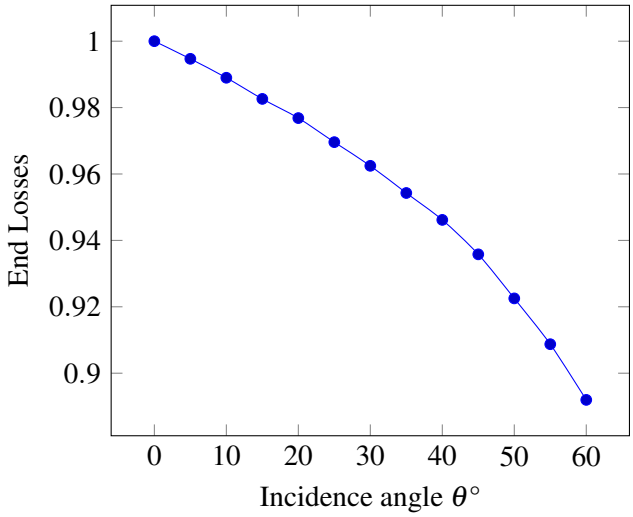

Figure 2.5: End Losses.

2.2 The FEM model

The second stage of the design phase deals with the finite element model developed in order to analyze the relevant physical characteristics of the receiver and to predict the thermal performance.

Several numerical models of the receiver tube of parabolic trough have been developed in the recent years [49, 50, 51, 52, 53, 54, 55]. Following these studies, a CFD model has been realized with Comsol Multiphysics version 5.2.

The model is a 3d termofluidodynamic model of the receiver tube; the parabolic mirror and the support brackets of the receiver tube have not been modelled. The model describes the dynamic of the fluid inside the absorber tube and the heat transfer between all the components of the receiver. The distribution of solar radiation on the absorber obtained through the ray-tracing analysis is applied on the outer boundary of absorber tube.

The model solves the Navier-Stokes equations (continuity, momentum and energy equation) in the fluid domain, the energy equation in the solid domain. A k-e turbulence model with wall function is used when the regime of the flow is turbulent.

The Navier- Stokes equations for a weakly compressible flow (density depends only from temperature) in a laminar regime are:

$$\frac{\partial \rho}{\partial t} + \nabla \cdot (\rho \mathbf{u}) = 0 \tag{2.2}$$

$$\rho \frac{\partial \mathbf{u}}{\partial t} + \rho (\mathbf{u} \cdot \nabla) \mathbf{u} = \nabla \cdot \left[-p\mathbf{I} + \mu \left(\nabla \mathbf{u} + (\nabla \mathbf{u})^T \right) - \frac{2\mu}{3} (\nabla \cdot \mathbf{u}) \mathbf{I} \right] + \mathbf{F} \tag{2.3}$$

$$\rho C_p \frac{\partial T}{\partial t} + \rho C_p \mathbf{u} \nabla T = \nabla \cdot (\kappa \nabla T) + \dot{q} \tag{2.4}$$

The main boundary conditions of the model are (fig 2.6):

- Inlet fluid temperature imposed;

- velocity is fixed in inlet; pressure fixed at outlet boundary;
- the solar flux distribution obtained by the optical analysis is imposed on the outer absorber surface;
- the radiation absorbed by the absorber tube is the 73% of the incoming radiation on the aperture area;
- radiation boundary condition on the inner boundary of glass envelope and on the outer boundary of the absorber; no convection inside the annulus since it is supposed to be under high vacuum, (about $10^{-4}\,mbar$);
- convective and radiative heat transfer between the glass surface and the outside applied on the external surface of the glass tube;
- solar radiation absorbed by the glass imposed on the glass surface.

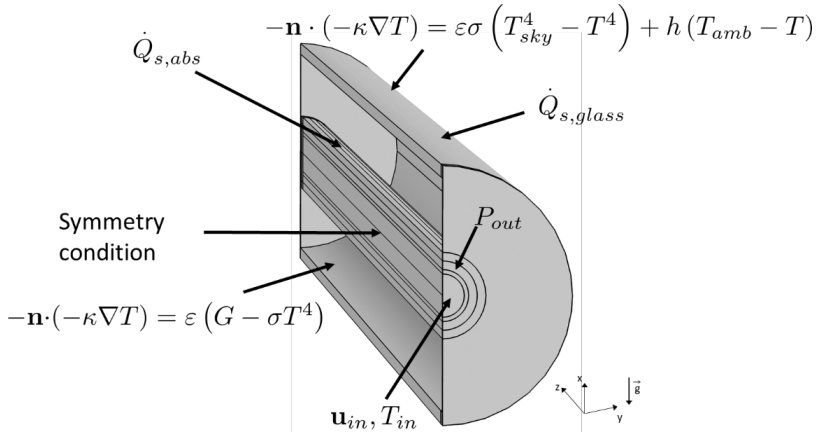

Figure 2.6: Boundary conditions of the FEM model.

The simulations have been run supposing water as heat transfer fluid since the experimental test will be performed using pressurized water.

A novel geometry solution for the absorber tube has been evaluated: the absorber tube is composed by two concentric tubes where the fluid flows. Through this configuration, the inlet and the outlet of the fluid flow are on the same side. This configuration is simpler to build, more robust and more economic than the standard one since it possesses fewer number of sealings. No advantages in thermal efficiency are expected from this configuration since the amount of energy on the absorber is fixed by the aperture area of the mirrors and by the optical properties of the materials. The diameter of inner absorber tube has been fixed to 5 mm; the diameter of the external absorber tube is 10 mm.

The geometry and the domains of the computational model are shown in Figure 2.7.

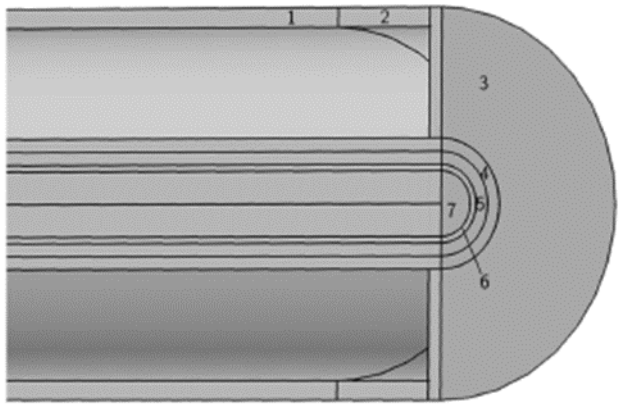

Figure 2.7: 1) Glass; 2) Kovar; 3) Kovar; 4) Outer absorber tube; 5) Fluid domain; 6) Inner absorber tube; 7) Fluid domain.

First of all, a mesh refinement test has been conducted to verify the numerical stability of the model. In table 2.3 are reported three different mesh configurations for the model and the main variables of interest. The tolerance imposed has been modified from 10^{-4} to 10^{-5} moving to finer mesh. It can be seen that the relative deviations are small ($\simeq 10^{-2}\%$) between the different mesh configurations and the results are stable.

Table 2.3: Mesh sensitivity analysis. Boundary conditions: $T_{in} = 293.15\,\mathrm{K}$, $\dot{m} = 0.018\,\mathrm{kg/s}$, $\mathrm{DNI} = 1000\,\mathrm{W/m^2}$. Dof stands for degrees of freedom.

Elements	Dof	T_{out} [K]	ε_{rel} [%]	ΔP [bar]	ε_{rel} [%]	$\bar{T}_{ass}$ [K]	ε_{rel} [%]	η_{th} [%]	ε_{rel} [%]
79487	203939	300.106		0.287		304.870		73.41	
135879	525418	300.076	$1\cdot10^{-2}$	0.285	0.6	304.721	$5\cdot10^{-2}$	73.08	$5\cdot10^{-1}$
261638	1059533	300.072	$1\cdot10^{-3}$	0.282	1.1	304.715	$2\cdot10^{-3}$	73.05	$4\cdot10^{-2}$

A parametric analysis has been conducted to investigate the performances of the receiver under different conditions for mass flow, inlet temperature, absorber tube materials, emissivity of the coating, irradiance, etc. In the analysis reported below, the thermal efficiency has been calculated through equation 1.13. The average temperature of the fluid on a section is calculated through:

$$\overline{T} = \frac{\int \rho C_p T\, \mathbf{u}\cdot\mathbf{n}\mathrm{d}A}{\int \rho C_p \mathbf{u}\cdot\mathbf{n}\mathrm{d}A} \tag{2.5}$$

where $\mathbf{u}$ is the velocity of the fluid, $\mathbf{n}$ is the normal of the surface, dA the section.

Figure 2.8 shows the thermal efficiency of the receiver tube varying the inlet flow velocity. The efficiency rises steadily until a turbulent regime has been established inside the two concentric tubes, about at $1\,m/s$. From this point, the heat transfer is maximum and the thermal efficiency is almost constant; as can be seen there are no thermal advantages using a velocity higher than $1\,m/s$. The optimal range of velocity has been selected as the one that maximize thermal efficiency and minimize pressure losses.

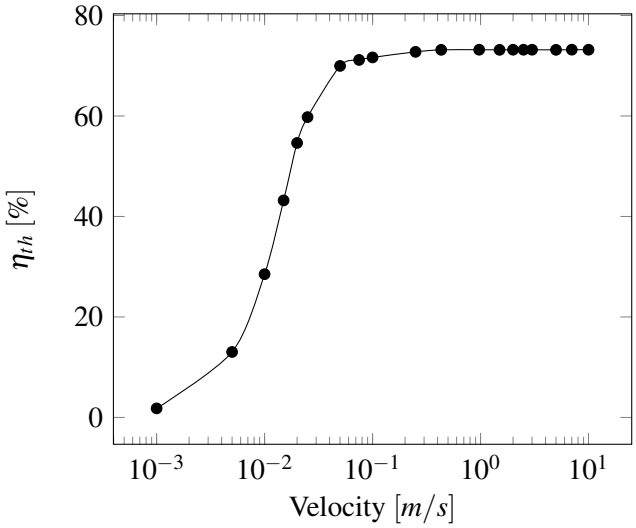

Figure 2.8: Thermal efficiency varying the inlet velocity $DNI = 800\,W/m^2$, $T_{in} = 293.15\,K$, $T_{amb} = 293.15\,K$.

In figure 2.9 the pressure drop inside the receiver tube is reported varying the inlet velocity of the flow. Assuming to accept a maximum pressure drop on the receiver of $1\,bar$, the velocity range that allows to reach maximum efficiency and low pressure drop is restricted to $0.25 - 2\,m/s$.

In the next simulations the value of $1\,m/s$ has been imposed. It can be noted that a significant reduction in the pressure losses can be obtained changing the diameter of the inner tube to 4 mm; in this way the external duct has a bigger hydraulic diameter and less pressure drop.

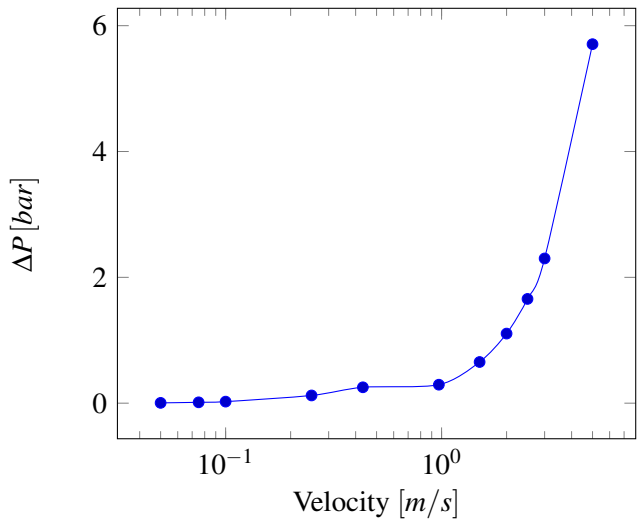

Figure 2.9: Pressure drop for different inlet velocities. Boundary conditions: $DNI = 800\,W/m^2$, $T_{in} = 293.15\,K$, $T_{amb} = 293.15\,K$.

Since the receiver tube is made up by two concentric tubes, it has been investigated whether the thermal efficiency was influenced by choosing as inlet tube the inner or the outer tube. No difference in thermal efficiency have been found between the two different configurations. The inner tube has been selected as the inlet tube.

In figure 2.10 is shown the average fluid temperature along the tube of the supply and return flow. As can be seen the maximum of fluid temperature is located before the outlet of the tube because of the heat transfer between the supply and the return fluid.

The distribution of temperature along the circumference of the tube is shown in figure 2.11 where only one half of the absorber tube is reported, since the irradiance distribution is symmetrical. As can be seen the variations along the circumference are small (3°C). This is due to the limited value of the concentration ratio of the collector and to the value of the rim angle chosen that uniforms the solar flux on the surface of the absorber.

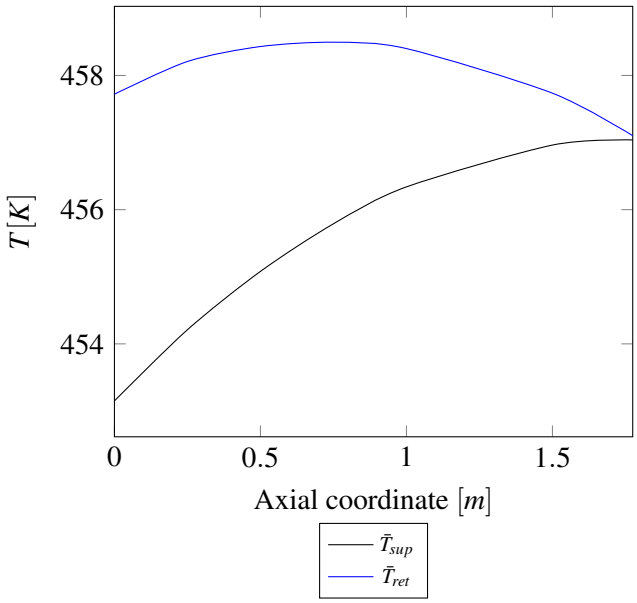

Figure 2.10: Average temperature of the supply and return flow along the length of the tube for $u = 1\,m/s$, $T_{in} = 453.15\,K$, $DNI = 800\,W/m^2$, $T_{amb} = 293.15K$.

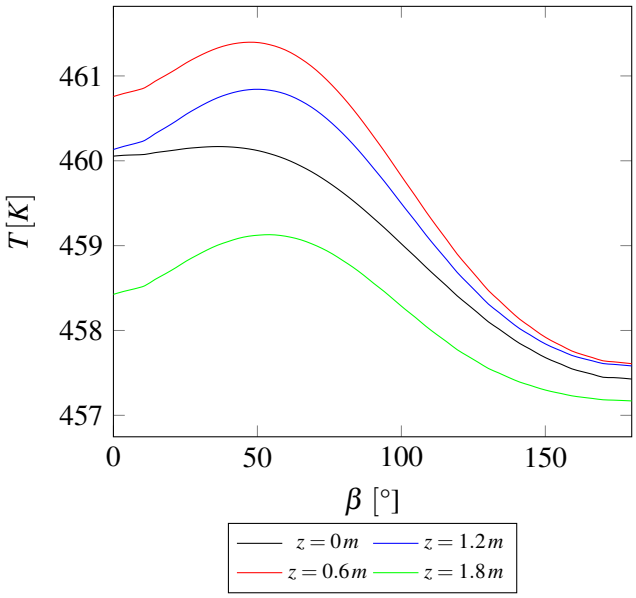

Figure 2.11: Profile of the circumferential temperature of the absorber tube for different points of z axis. On the abscissa is reported the angle measured from the lower vertical position of the tube. $u = 1\,m/s$, $T_{in} = 453.15\,K$, $DNI = 800\,W/m^2$, $T_{amb} = 293.15K$.

Figure 2.12 shows how the emissivity of the coating deposited on the absorber tube, influences the thermal efficiency of the receiver. The absorbance of the coating in the solar spectrum has been fixed in the optical analysis to 95%. A selective coating is needed since coating with high emissivity in the infrared, such as 50% and 30% of emissivity, lead to unacceptable heat losses. Moreover, comparing the performances at 240°C of an optimum selective coating (5% of emissivity), and a medium selective coating (15% of emissivity), the deviation in efficiency between them is only 3%. Thus, it is possible to choose a more economic coating without a significant loss in thermal performances. In these simulations the emissivity has been kept constant with temperature; in reality, the emissivity rises with the temperature of the coating.

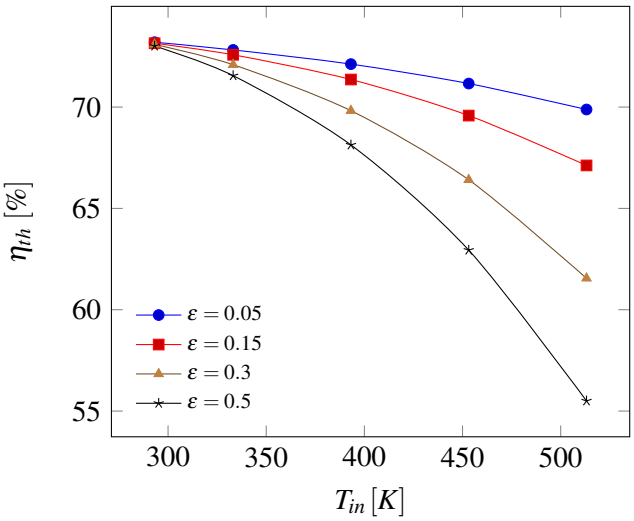

Figure 2.12: Thermal efficiency versus inlet temperature for different values of emissivity for $DNI = 800\,W/m^2$.

Figure 2.13 shows the thermal efficiency versus fluid inlet temperature. The dot line represents the optical efficiency of receiver, calculated by ray-tracing software, fixing the reflectivity of the mirror, the transmittance of the glass and the solar absorbance of the coating. The selective coating used for this simulation has emissivity in the infrared equal to 0.12. The drop in thermal efficiency at 240°C due to heat losses is only 6% thanks to vacuum in the annulus and to selective coating.

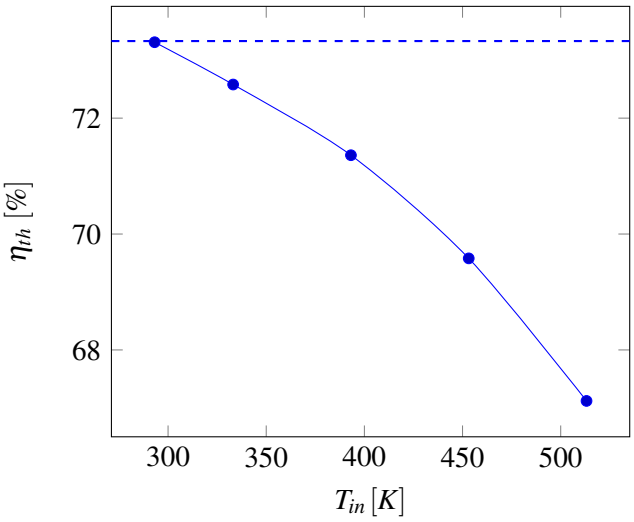

Figure 2.13: Efficiency curve versus inlet temperature; $DNI = 800 W/m^2$, $\dot{m} = 0.02 kg/s$, $T_{amb} = 293.15K$. The horizontal line is the peak optical efficiency of the collector.

The increase of temperature inside the collector varying the inlet fluid temperature for different conditions of solar irradiance is reported in Figure 2.14. For an inlet fluid temperature of 20°C a rise of about 5 °C is predicted at 800 W/m^2 .

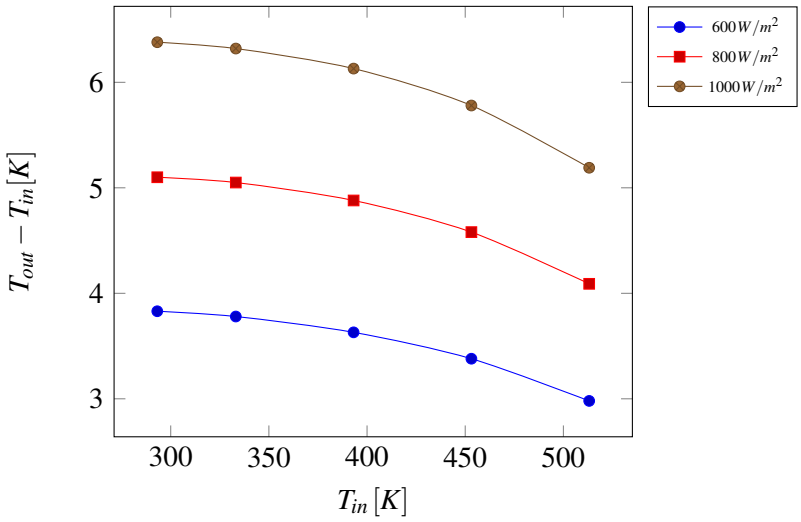

Figure 2.14: Temperature rise versus inlet temperature for different value of DNI, $\dot{m} = 0.02\,kg/s$, $T_{amb} = 293.15K$, $\varepsilon = 0.12$.

The variation of efficiency with temperature varying the irradiance on the aperture is reported in figure 2.15. As expected, the efficiency drops with the reduction of the DNI on the aperture.

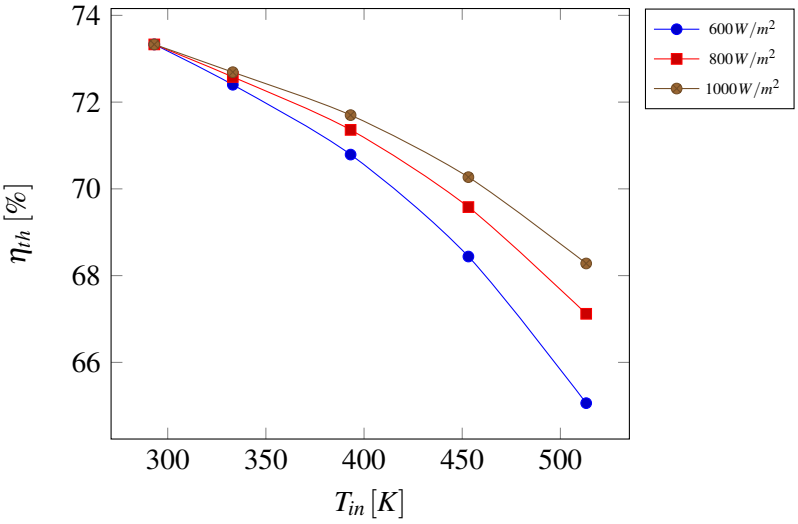

Figure 2.15: Efficiency versus inlet temperature for different value of DNI, $\dot{m} = 0.02 kg/s$, $T_{amb} = 293.15K$, $\varepsilon = 0.12$.

Simulation have been run investigating the influence of the external temperature and of the velocity of the wind. As expected, thanks to the vacuum envelope, no significant variations have been showed.

Steel, copper and aluminium have been investigated as absorber material; it has been found that the different thermal conductivity of the materials does not influence the thermal efficiency of the receiver tube.

A structural mechanic FEM model has been realized to verify the thermal stresses on receiver tube due to the non-uniform incident solar flux. The stresses evaluated by the numerical model are under 30 MPa, as can be seen in Figure 2.16, well below the yield stress of the materials. The vertical displacement due to thermal stress are reported in Figure 2.17. The inner absorber tube leans on the outer tube since it is free to move. The outer absorber tube properly constrained with springs to the glass tube, remains in the initial position without moving away from focus position.

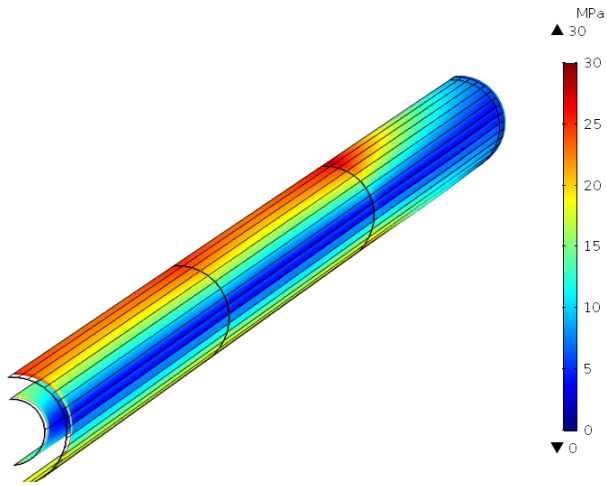

Figure 2.16: Von Mises stress on the outer absorber tube. For $1000\,W/m^2$, $T_{in} = 453.15\,K$.

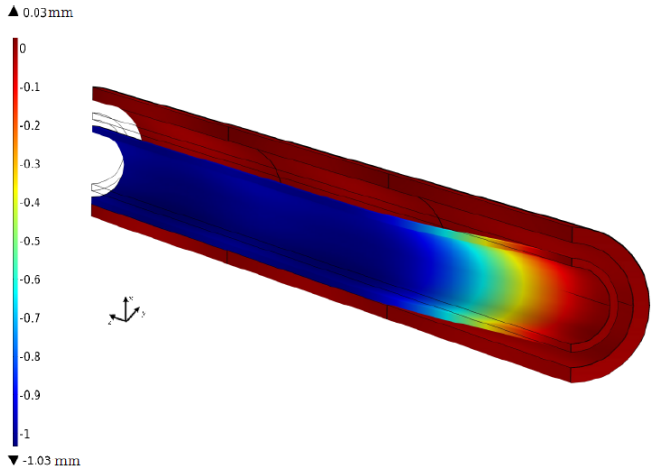

Figure 2.17: Vertical displacement of the outer and inner absorber tubes due to thermal stresses. For $1000\,W/m^2$, $T_{in} = 453.15\,K$.

Chapter 3

The prototype of m-PTC and the indoor test bench

3.1 The prototype of m-PTC

A prototype of a small size parabolic trough collector, called m-PTC (micro-PTC) has been realized following the results and the indications of the numerical analyses (Figure 3.1).

The m-PTC is characterized by extremely small size: it possesses an aperture width of just 420 mm and it is 1800 mm long. The parabolic mirror has a rim angle of 100° that permits to reduce the weight of optical errors and to increase the acceptance angle of the reflected radiation. The receiver tube, characterized by an external diameter of 10 mm, has been realized by a highly specialized company in the sector of the solar collector. The m-PTC is innovative for the dimensions since it is much more compact and transportable respect than the parabolic trough collectors developed to date. Furthermore, the system aims to achieve high levels of thermal efficiency, better than the standard solar thermal collectors.

Figure 3.1: The m-PTC.

The receiver tube possesses an innovative design: is made by two concentric ducts where the heat transfer fluid flows, letting the flow enter and exit just by one side. This geometry solution takes some advantages respect to the standard, in which the fluid pass through the tube from one side to the other: accepting a little higher drop in pressure, it is much simpler and also more economical to build. In fact one closed edge is realized just sealing the glass on itself during the crystallization and the glass-to-metal junction is applied one side. Decreasing the number of those elements, which represent a critical aspect for solar absorbers in general, also lead to reduce the risk of loosing vacuum conditions in long term time. Furthermore, the one-end configuration of the receiver has advantages in maintenance operations permitting to replace the receiver tube easily in case of breaking.

The absorber tube has a diameter of 10 mm (1 mm thickness); the smaller concentric tube has an internal diameter of 5 mm (0.5 mm thickness). A selective Cermet absorber ($\alpha = 0.94$ and $\varepsilon = 0.12$ at ambient temperature) has been deposited on the absorber tube to increase absorption of solar radiation and re-

duce radiative losses. Since the numerical analysis have not be found significant differences in the thermal and structural behavior of the different materials for the conditions of interest, copper has been chosen as absorber material since the major availability on the market of pipes of small diameter and the simplicity in the assembly of connections of the pipes. The absorber tube is surrounded by a glass envelope coated by anti-reflective layer to prevent reflection of the solar radiation by the surface of the glass. In order to reduce the heat loss of receiver, the annulus between glass and copper tube is evacuated, with a good degree of vacuum ($10^{-4}\,mbar$). A getter is present inside the annulus to absorb hydrogen and to maintain vacuum. In order to match the different thermal expansion of the glass and of the copper and to improve the sealing, a layer of Kovar (iron-nickel-cobalt alloy) has been inserted since the thermal expansion coefficient of the Kovar is similar to the glass and the strength of glass to Kovar seals is much better than glass to copper. The receiver can use pressurized water or silicon oil as heat transfer fluid.

The features of the parabolic collector realized are reported in table 3.1. The concentration ratio of the collector, the ratio between the area of the mirror against the area of the absorber tube, is 14. The mirror is made of aluminium with a value of specular reflectivity of 0.88. The collector tracks the sun through a 1-axis tracking system with a sun sensor realized inside the group of research.

Table 3.1: Features of m-PTC

Parabolic Mirror	Aluminum, $l = 1800\,mm$, $a = 420\,mm$, $\phi = 100^{\circ}$ $\rho = 88\%$
Glass	Pyrex Transmittance $\tau = 0.95$ Absorbance $\alpha_{sol} = 0.02$
Absorber	One-end receiver, copper, external diameter $10mm$
Selective coating	Cermet $\alpha_{vis} = 0.95$ $\varepsilon_{IR} = 0.12$

Four springs support both the pipes in glass cylinder and keep them aligned in the reflector focus as shown in figure 3.2.

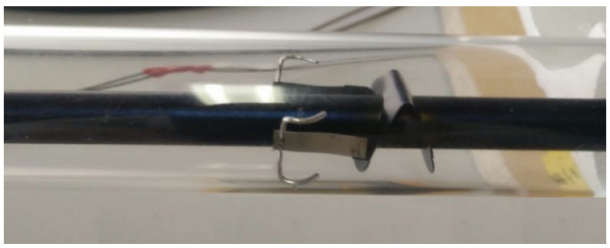

Figure 3.2: The receiver tube and the supports for the absorber tube.

3.2 The test bench for heat loss measurement

At first, an indoor test bench has been realized in order to test the receiver tube and verify if the manufacturing quality of components and the overall performance

were as requested.

To test the performance of the receiver tube of parabolic trough, the thermal losses of the receiver tube have to be measured.

In recent years, several test benches to measure the thermal losses of the receiver tubes have been realized by the major centers of research on concentrating collectors: ENEA, NREL, DLR, PSA [38, 56, 57, 58, 59, 60, 61].

Three different modes to measure the heat losses are possible based on the stationary equilibrium, on the quasi-stationary equilibrium and on the surface temperature measurement of the absorber [62]. In practice, only the stationary method is used because it is the only that can provide precise measurement of the heat loss. For the stationary method, the typical heat loss testing technique is based on the use of an electric heater, usually a cartridge heater, to heat up the absorber tube that it is placed in laboratory, not irradiated by the Sun (off-sun condition) [57]. The power of the heater is raised until the desired temperature of the absorber has been reached and the thermal equilibrium is established in the receiver tube. In stationary conditions, the heat loss is equal to the electric power required to maintain the system in equilibrium:

$$\dot{Q}_{Loss} = \dot{Q}_{Electric} \tag{3.1}$$

The measurement is evaluated at steady state of quasi-constant absorber temperature and heating power. The temperature of the absorber tube is monitored by several thermocouples placed in different locations. A homogenization tube made by copper or brass is usually placed between the heater and the absorber to homogenize the temperature of the absorber.

Because of the small size of components, the common layout with the cartridge heater was not suitable in this case. Therefore, a slightly different testing method, based on the joule effect, generated directly, is used (figure 3.3). A rigid copper bar, which is insulated by a dielectric sleeve is inserted in the absorber tube. The end of the bar is in contact with the external absorber tube in order to establish an electrical circuit in which the two different poles (negative and positive) are located at the beginning of the system. In this configuration, Joule effect is generated directly using a constant voltage power supplier. At thermal equilibrium: $\dot{Q}_{Loss} = VI = RI^2$.

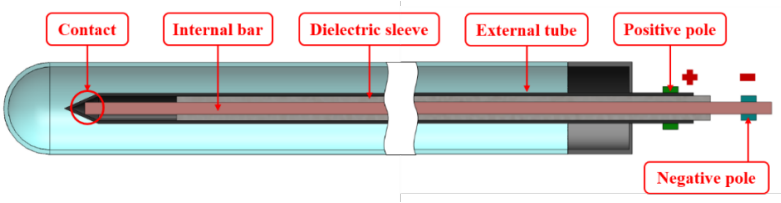

Figure 3.3: Scheme of the electrical branch made with the external tube of the receiver.

Several sensors are necessary to monitor and measure the main characteristics of the system. A hall effect transducer is used to measure the supply current (calibrated with an error $< 0.1\%$ of MV). Temperature sensors, set up by 3 type T thermocouples and 2 RTDs are arranged as in Figure 3.4. The thermocouples are fixed around the dielectric sleeve and the small clearance between the absorber and the bar guarantees the contact with the internal surface of the outer tube. The thermocouples have been placed in three different axial positions (at the beginning, in the middle and at the end of the absorber tube), to check during operations if the tube was uniform in temperature. The flat RTDs are located at the beginning of bar and on the surface of the glass tube at about 1 m from the inlet. Furthermore, a data acquisition systems is used to acquire the overall signals and voltage in the circuit with global error $< 1\%$ of MV.

At the open end of the receiver a coil heater is placed to balance the axial conduction heat loss. Furthermore the open end is insulated in order to reach a condition of adiabaticity at the end.

The heat losses of evacuated receiver tube have been deeply investigated. Two configurations of receiver tube have been tested: evacuated tube and non-evacuated tube. A receiver tube has been modified making a hole in the glass to fill the annulus with air at ambient pressure in order to compare its heat losses with the evacuated receiver.

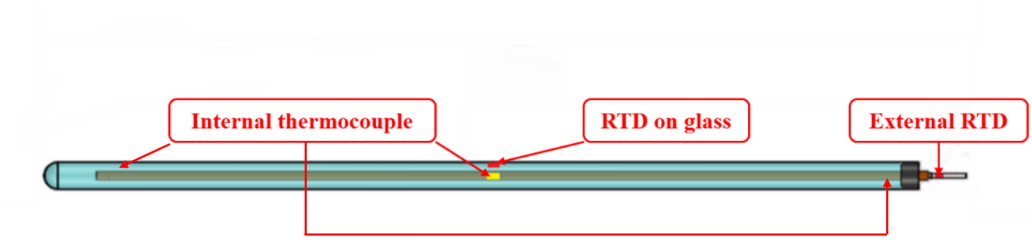

Figure 3.4: Position of the temperature sensors.

3.3 Heat loss results

First of all, some preliminary tests have been conducted to check if the absorber tube was heated uniformly, finding less than 5°C of difference in the temperature recorded along the tube by the thermocouples. Furthermore, it has been evaluated the thermal gradient close to the open end of the receiver to check if the condition of adiabaticity was reached. Successively, the measurement of heat losses have been realized. Fixing the value of voltage, the absorber tube has been heated up to the desired temperature. When thermal equilibrium has been well established, monitoring that temperature of the absorber tube was constant in the accuracy of thermocouples ($\pm 1°C$) for a large interval of time (20 minutes), the equilibrium power is recorded and thermal loss is derived summing the thermal power due to the Joule effect and the thermal power due to the coil heater. The value of the voltage drop and of the current have been recorded every second; filtering and average operations on data have been performed.

In Figure 3.5, thermal losses are shown as a function of the difference between absorber temperature and ambient temperature. Test have been conducted up to the absorber temperature of $240\,°C$ for the evacuated tube and up to 180°C for the non evacuated receiver.As can be noted, the experimental point of the evacuated receiver has a polynomial trend (radiative losses) and the non evacuated thermal loss has a linear trend since convective losses are present. The experimental points have been obtained averaging several set of measurements ($>$ 10 measurements

for each point).

It is worth to notice that for $160\,°C$ of difference between absorber and ambient temperature, the thermal losses of the non evacuated receiver are 4 time higher than those of the evacuated receiver, $95.4\,W$ for the non evacuated against $23.5\,W$ for the evacuated tube. The value of $23.5\,W$ corresponds to the heat loss per square meter related to the aperture area of $30.5\,W/m^2$. The receiver realized by Schott [58]for high temperature applications (up to $400\,°C$) is characterized by a coating of emissivity of 0.07 at $180\,°C$. Comparing the thermal losses related to the aperture area of the two receivers, the heat losses of Schott receiver tube are lower (about $8\,W/m^2$) thanks to the better performances of the selective coating.

For the evacuated receiver five different receiver tubes have been tested, finding results in agreement with each other.

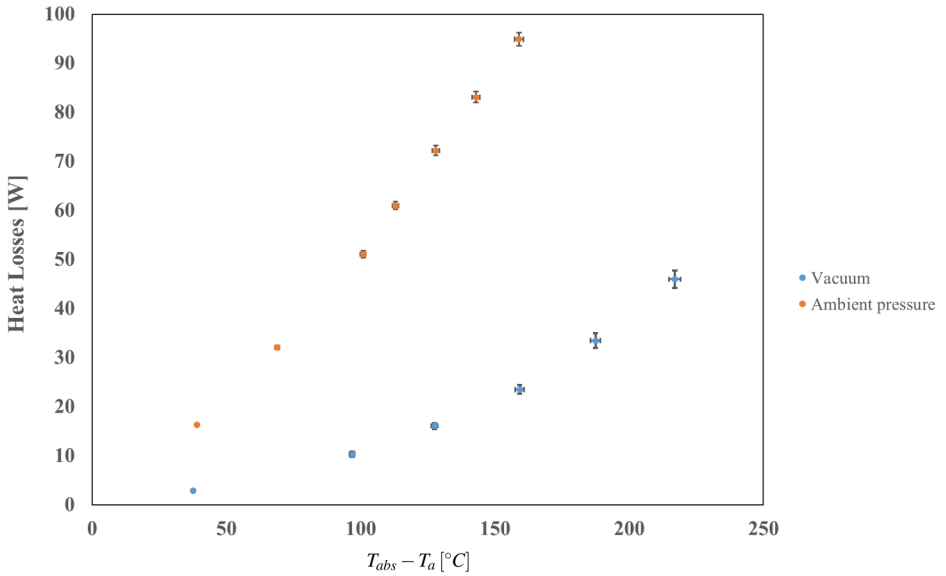

Figure 3.5: Thermal loss versus the difference between the internal and ambient temperature.

The variation of the glass temperature is reported in figure 3.6. For vacuum

case, the temperature is always below 30°C; for non evacuated case it rises up to 60°C for an absorber temperature of 180°C.

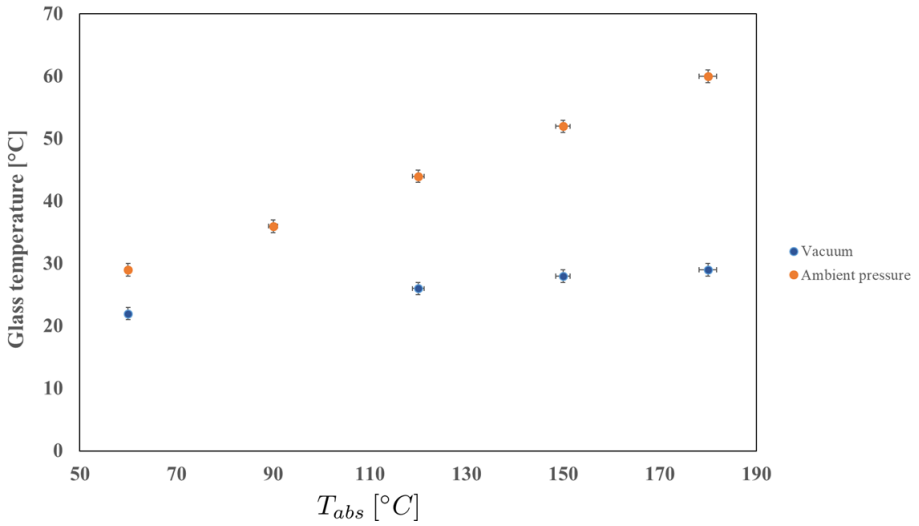

Figure 3.6: Glass temperature for non evacuated and evacuated tubes.

3.4 Calculation of the emissivity

The experimental results of off-sun heat loss test have been compared with the outcomes of numerical simulations. The FEM model has been slightly modified to represent properly the experimental configuration of off-sun heat loss test. Only the heat transfer inside the receiver has been modeled with no fluid flow inside the absorber; it has been imposed no solar flux on the absorber tube and a fixed thermal flow on the absorber. The numerical model predicted precisely heat losses at low temperature, below 60°C of the absorber temperature, but underestimated heat losses at high temperature with values well below the experimental error bars. This was due to the fact that in the simulations the emissivity of coating had been fixed to the value at ambient temperature, $\varepsilon = 0.12$, provided by the manufacturer

of the receiver and verified by the group of research with a spectrophotometer, since his trend with temperature was not known. Therefore, the model has been upgraded to describe correctly the increase of emissivity with absorber temperature. In order to obtain the estimation of emissivity at the maximum temperature of heat loss test, unknown experimentally, the emissivity in the numerical model has been varied until the numerical heat loss were in agreement with experimental one, inside the experimental error bars. Knowing the emissivity value at ambient temperature and the value at 240°C, it has been possible to approximate the variation of emissivity with temperature through a linear fit:

$$\varepsilon = 5.45 \cdot 10^{-4} \cdot T - 3.96 \cdot 10^{-2}$$

with T expressed in Kelvin and $T \geq 293.15$K.

Using the value of emissivity from the linear fit, the numerical simulations have been run again for the range of temperature of interest (fig. 3.7). All the experimental values for thermal loss are well predicted by the heat transfer model since the numerical outcomes lie in the experimental error bars.

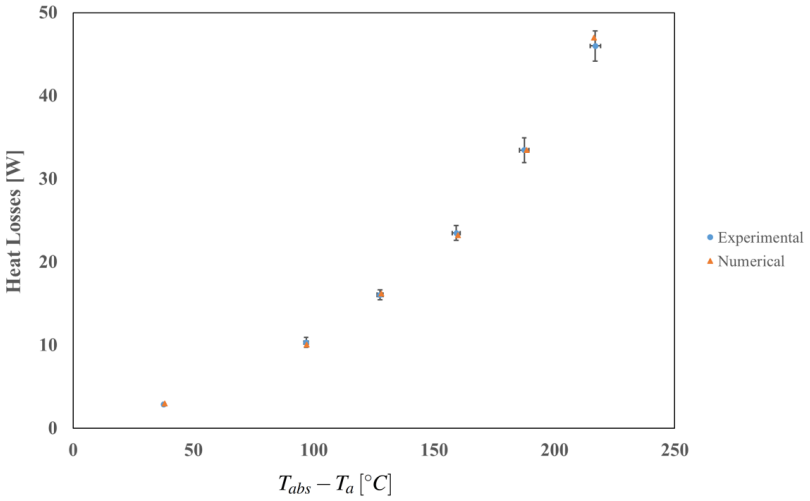

Figure 3.7: Comparison between the numerical and experimental results

Chapter 4

The efficiency test of m-PTC

4.1 The test rig

A test rig has been designed to test the small parabolic trough collector under on-sun conditions and to obtain the efficiency curve of the collector.

The test rig must be able to determine the main parameters of the collector (the peak optical efficiency, the thermal efficiency, the incidence angle modifier) respecting and following existing standard procedure for test on concentrating collector. There are several standards (EN 12975-2, ISO 9806:2017, ASTM E905-87:2013) but there is no uniformity about testing conditions (section 1.7). Two kind of test are possible for concentrating collectors: the steady (or quasi-steady) state method and the quasi-dynamic method. The requirements of the steady state method are more strict than of the quasi-dynamic method as reported in tab 1.3 for what concerns the permitted fluctuations of inlet temperature, irradiance and mass flow rate. The test rig has been designed to meet the requirements of the quasi-steady stationary test.

4.1.1 Main components of the test rig

The test bench is composed by an Azimuth Platform, where the collectors are placed, and by a closed loop hydraulic circuit.

The rotating platform allows to follow the sun along the azimuth direction. Coupled with the altitude tracking installed on the collectors, the parabolic collectors possess a 2-axys tracking. This permits to run test continuously during the whole day with an incidence angle on the collector equal to zero. In this manner, test are not limited to the short periods of time where the incidence angle is close to zero (i.e. solar noon for a PTC with alignment along East West) and the time needed for the complete characterization of the collector is reduced considerably. Moreover, through the 2-axys tracking, since IAM is always equal to 1, it is more easy to separate and distinguish the contribution of the optical losses from the thermal losses. For these reasons, a rotating platform, suitable to place four small parabolic trough collectors, has been designed and realized. The sun is therefore tracked by an alt-azimuth 2-axis tracking.

The azimuth platform, fig. 4.1, is suitable to accept different modules of panels: photovoltaic, thermal, hybrid, etc.

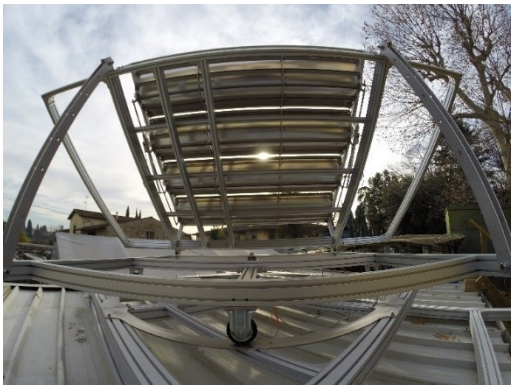

Figure 4.1: The rotating platform.

The azimuthal movement is carried out by means of a gear-motor equipped with an encoder, while the elevation movement of the platform is fixed with an adjustable angle in the range 0-45°. The elevation movement could be properly modified with electric pistons connected to the collectors directly. The features of the rotating platform are reported in table 4.1.

Table 4.1: Features of the rotating platform

Testing platform	
Width	2.2 m
Length	2 m
Azimuth range	-110°, $+110^\circ$
Tilt range	$0^\circ - 45^\circ$
Azimuth tracking accuracy	$\leq 0.1^\circ$
Elevation tracking accuracy	$\leq 0.1^\circ$

A module composed of 4 small parabolic collectors is installed in the mentioned test bench. The collectors are connected in parallel configuration. The series configuration has been avoided in order to limit the total pressure drop on the collectors. Furthermore, this modular arrangement has been considered suitable for the integration and the installation of the collectors on the roofs. The axis of the collectors are aligned along E-W direction and with a kinematics for tracking the sun in one direction (elevation). The vertex of four mirrors are connected through two metal bars at the edges and they are moved by two linear actuators (fig. 4.2). Compared to the standard parabolic trough collector, a novel system of tracking has been implemented: the rotation axis and absorber tube coincide and so the absorber is in a fixed position during operation, avoiding flexible pipe connections. Furthermore, since it is planned to cover the collectors with glass covers to repair them from soiling and to permit a simpler cleaning, in this configuration the center of mass of the collector coincide with the receiver tube, reducing the total torque necessary to move the collector.

Figure 4.2: Linear actuator.

The Sun is tracked by a specific sensor which has been developed inside the group of research and tested. It is a wide angle light detector built with two calibrated photodiode elements with a surface area $2x2\,mm^2$, separated by a shadowing opaque plate (fig. 4.3). The sensor is aligned with the aperture area of the mirrors, i.e. the normal to the sensor is parallel to the normal to the aperture area. If the sun rays are normal to the aperture plane, both the photodiodes give the same voltage output (0-5 volt range). On the contrary, if the opaque plate shade one of the elements, a voltage imbalance is measured. A proper hardware and software based on Arduino and Python platform has been developed in order to realized a closed-loop control, to monitor the sensor and drive the linear actuators for tracking the Sun in the right direction. The accuracy of sensor to track the sun has been verified through the use of a digital inclinometer to be less then 0.1°.

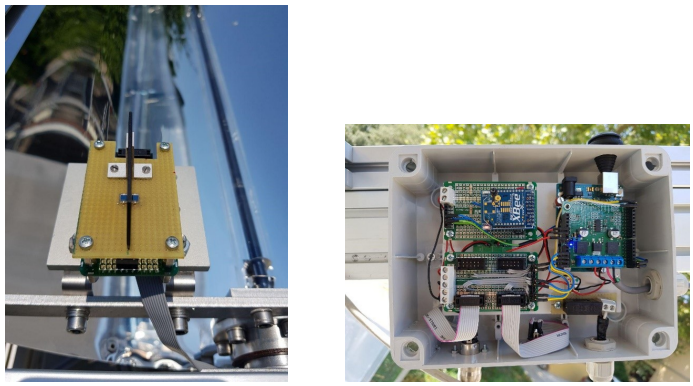

Figure 4.3: On the left Sun positioning sensor. On the right Arduino platform to monitor the sensor and supply the linear actuators.

The collector has been tested using pressurized water as heat transfer fluid. In order to meet the requirement for the quasi-stationary test, the test-loop is characterized by:

- a feed-water system;
- a heating system to warm the fluid up to desired temperature;
- a cooling system to maintain stationary conditions in the circuit;
- an instrumentation and control system.

The P&I of the test bench is illustrated in figure 4.4, underlining two different hydraulic circuit (red and blue) divided by a heat exchanger (Cooler). The red side is designed to be connected to the solar collector and to work with pressurized hot water at medium temperature (up to 200°C and 16 bar). The blue side assures the dissipation of the heat gained from the Sun and contains the main control system to stabilize the collector inlet temperature. The components in this side operate at low temperature and pressure levels inducing minor stresses and safer conditions.

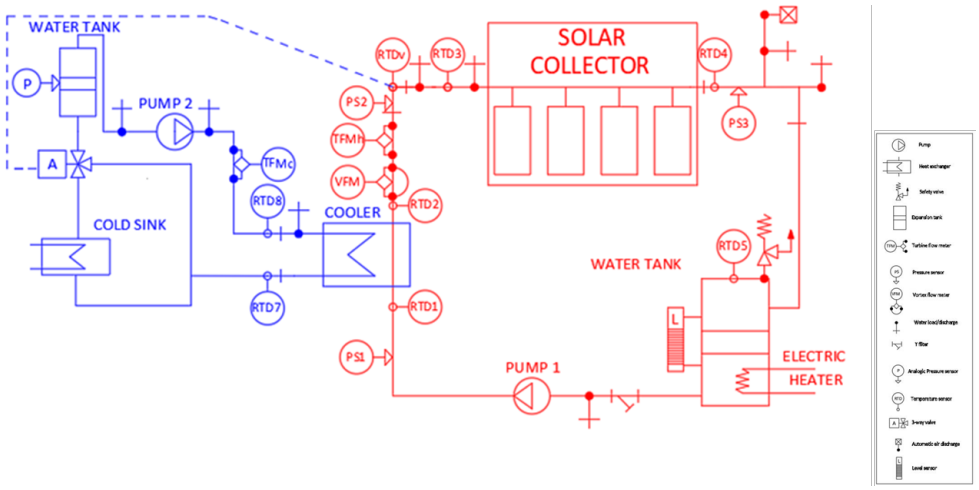

Figure 4.4: P&I of the test bench.

The test bench is installed in Florence, at Department of Engineering (43°47'52.0" N, 11°15'15.2"E). A summary of the main features of test rig is reported in table 4.2.

Table 4.2: DNI resource in Florence and main features of the test rig realized.

DNI in Florence	$1333\ \left[kWh/\left(m^2 \cdot y\right)\right]$
Test rig	
Number of PTC installed	4
Operating temperature	$10°C < T < 200°C$
Maximum pressure	16 bar
2-axys tracking	

4.1.2 Test loop design

Pump

Since the small dimension of the diameter of absorber tube, the mass flow of the circuit has to be kept quite low (section 2.2). Considering a maximum inlet velocity of 2.5 m/s, the total volumetric flow for one collector is about 180 l/h. Furthermore, supposing to test 4 collectors in parallel, with the reference inlet velocity of about 1 m/s, the total volumetric flow is 240 l/h. For this reason a sliding vane pump designed for low volume flow (maximum 250 l/h) has been selected (fig. 4.5). The pump is able to work up to 250°C at a pressure of 25 bar.

Figure 4.5: The sliding vane pump.

Expansion tank

An expansion tank is needed for the expansion of water and to control the pressure inside the circuit. An amount of 35 l of water has been considered sufficient for thermal inertia. Circuit pressurization is done by introducing air into the top cavity of the tank.

The volume of water inside the tank is 35 l and in the circuit is about 5 l.The coefficient of dilatation of water between 20°C and 190°C is 0.1360. It means that

the expected increase of water volume is about 5.5 l.

For this reason a 50 l tank has been selected (fig. 4.6).

Figure 4.6: The expansion tank.

Heating system

In order to warm up quickly the heat transfer fluid, an electric resistance heater has been installed inside the tank with an on/off control system. The electric heater has been sized considering that test should be performed up to 190°C. Accepting that the time required to heat the fluid inside the tank and the wall of tank up to the maximum temperature is about 1.5h, the electrical power of the heater needed is:

$$\dot{Q}_{heating,elec.} = \frac{\frac{V_w \rho_w C_{P,w} \Delta T_w}{\Delta t} + \frac{V_{tank} \rho_{tank} C_{tank} \Delta T_{tank}}{\Delta t}}{\eta_{heat}} \tag{4.1}$$

where Δt is the required time to heat up both the water and the tank, ΔT_w and ΔT_{tank} are the temperature increase in the water and the tank, V_w and V_{tank} are the volume of water and tank to be heated. For this application, $V_w = 0.050\,m^3$, $V_{tank} = 0.01\,m^3$, $\Delta T_w = \Delta T_{tank} = 170\,°C$, $\Delta t = 1.5h$, $\eta_{heat} = 0.85$, water properties are evaluated at the average of $20\,°C$, 1 bar and $190\,°C$,15 bar. The power of

the electric heater needed is about 8 kW. 9 electric resistance of 1 kW has been installed inside the tank.

Cooling system

In order calculate the cooling power needed, the cooling power has to be equal to the maximum thermal heat gained by collector. Assuming a maximum DNI of $1000\,W/m^2$ and a peak optical efficiency of 75%:

$$1000\,W/m^2 \cdot 2.856 \cdot m^2 \cdot 0.75 \cong 2150\,W.$$

The plate heat exchanger has been designed to balance the thermal power gained by the water of the main circuit in the collectors.

4.1.3 Measurement sensors

Several sensors have been placed strategically along the circuit to measure the flow rate, the temperature and the pressure of the fluid.

The quality of measurement sensors deeply influences the final uncertainty associated to the variables that have to be calculated such as useful thermal power and efficiency. A study realized by Hofer et. al. [63] shows which variables influence most the global uncertainty of the system. It has showed that, for small size concentrating collectors working at 150-200°C, with a temperature drop of 20°C on the collector, equipped with high precision sensors, the uncertainty on thermal power can depend for the 70% by uncertainty on temperature. For this reason particular attention has been focused on the temperature sensors. The best accuracy sensors for temperature, RTD Pt100 1/10 DIN, with four wire connections, have been used and have been opportunely calibrated. Two of them have been placed at the inlet and at the outlet of the collectors to measure the temperature drop on the collectors; the other temperature sensor have been placed along the circuit as can be seen in figure 4.4.

The meteorological data are measured through a two axes sun tracker (fig. 4.7) composed by a pyrheliometer and by two pyranometer, for the measurement of direct, global and diffused radiation. A thermos-hygrometer and an anemometer

complete the system, measuring outdoor temperature and humidity, wind direction and intensity. The sun tracker is installed on the roof of the department of engineering in Florence, very close to the test bench (less than 100m).

Figure 4.7: The two axes sun tracker with one pyrheliometer and two pyranometer.

The features of sensors are reported in table 4.3. To record the measured values from the sensors, commercial data logger (dataTaker DT80) has been used during the test.

Table 4.3: Sensors used in the test bench.

Temperature sensors for HTF	RTD Pt100 1/10 DIN, 4 wire Tolerance $0.03 + 0.0005 \cdot T$, $0.03 - 0.12$°C @ $0 - 180$°C
Flowmeter	Vortex flowmeter Accuracy 0.75% o.r.
Pressure sensor	membrane transducer Accuracy 0.25% FS BSL a 25°C Measurement range 0-15 bar
Temperature sensor for T outdoor	RTD Pt100 1/10 DIN, 4 wire, Tolerance$0.03 + 0.0005 \cdot T$, $0.03 - 0.12°C$ @ $0 - 180$°C
Sun tracker (Solys 2)	First class pyrheliometer with accuracy <1% Pyranometer Pyranometer with shading ball
Acquisition system	Datataker DT80 Frequency of acquisition every 3s

4.1.4 Data acquisition

To manage all the acquisitions and data recording process, it has been programmed with LabVIEW environment. A customized graphical user-interface (fig. 4.8) has been developed properly and used to monitor in real time the measured quantities and possible alarms of cold and hot circuit.

The program has these features:

- A graphical display of the principal variables monitored.
- It allows to save data acquired during the test in excel format.

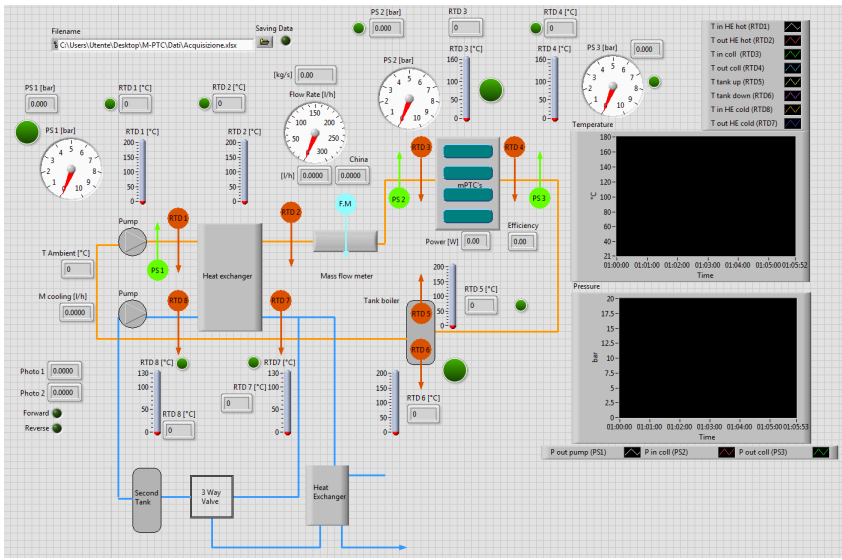

Figure 4.8: The graphical user-interface for monitoring the test rig in LabVIEW.

- It calculates from data collected some parameters (heat output, thermal efficiency) to have a preliminary evaluation of the system.
- It points out when a measured quantity (e.g. temperature, pressure) exceeds the permitted value.

4.1.5 Operations of the system

In the hot circuit, the pumped water reaches the tested solar collectors after passing through the main heat exchanger (cooler). Four collectors connected in parallel are mounted on the platform and thus can be tested simultaneously. The cold circuit is used to control the solar collector inlet temperature automatically, in a precise way. This cooling system was designed using water at barometric pressure as cooling fluid. The cold circuit is composed of a water tank, pump, heat exchanger and 3-way valve. The double-pipe countercurrent flow heat exchanger was considered to control the thermal power gained by the water of the

hot circuit through the collectors and reduce the outlet temperature keeping the inlet constant. High-pressure hot water of the main circuit flows through one side of the plate heat exchanger while the cooling water at ambient temperature flows through the other side at aqueduct pressure. The 3-way valve (modulating control valves) manages mass flow by magnetic actuators and impose two different hydraulic branches: it has a fast positioning ($< 2sec$), high-resolution (1:1000) and it is controlled by a RTD1000 signal. This sensor is placed at the collector inlet and it checks the temperature during the test in real time. If the inlet temperature of the solar collector increases due to solar radiation, the water is diverted by the 3-way valve to a cold sink through another plate heat exchanger and the hot water is cooled down consequently, otherwise it is recirculated. The constant cold sink is represented by one tank of about $200\,m^3$ water at ambient temperature. When test are performed at high temperature, the electrical resistance are turn on to warm up faster the heat transfer fluid.

4.2 Test of thermal efficiency

4.2.1 Procedure and first tests

A list of operations have been repeated every day before running the tests.

- The surface of the reflectors and of the receiver tubes have been cleaned carefully from the accumulated dusts and dirt. Mirror soiling can seriously reduce the optical performance of collectors.
- It has been checked that the sun-tracking sensor was parallel with the aperture plane of the mirror through an inclinometer.
- It has been verified that no air pockets were present in the collectors through the opening of the valve. The presence of air reduces dramatically the efficiency of the collector.
- The tank in the hot circuit has been filled up from the water supply up to well-defined level. The system has been pressurized through the air compression system.

Preliminary test have been conducted without thermal insulation in order to verify possible leakages in piping and connections. No leakages have been detected. Afterward, the header pipes have been insulated.

The first experimental test on the collectors is carried out during a clear sky day and a part of the recorded data is presented in figure 4.9 as a function of the time (about 10 minutes). The direct normal irradiance (DNI) has an average value of 775 W/m^2, ambient temperature is 29.7°C and the main pump circulates the water from tank to the m-PTC. Four collectors have been tested simultaneously. The main pump frequency for this purpose is fixed by an inverter at 25 Hz, corresponding to about 128 l/hr, corresponding to a velocity of about 0.5 m/s inside the receiver tuber. The flow rate of the water passing through the pipes is kept at constant value during the test with a variation under 1%. The pressure of the system is controlled by the expansion tank. Temperature, pressure, flow rate and DNI are measured directly; other main parameters such the thermal power output and the thermal efficiency are derived in real time to evaluate the performance of the collector.

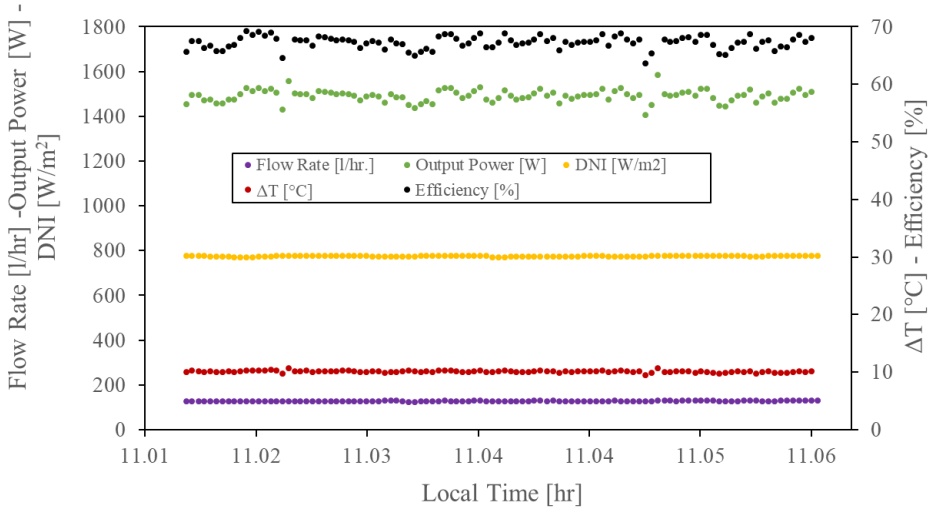

Figure 4.9: The main test parameters as a function of time.

In figures 4.10-4.11 one example of peak optical efficiency test is reported: the inlet temperature of collector is very close to ambient temperature, so thermal losses are small, and the angle of incidence on the collector is equal to zero thanks to the two axis tracking. The time period of the test is about 10 minutes. All the variables (inlet temperature, volume flow, DNI, ambient temperature) are very stable during the test interval, thus the system is in stationary conditions. In figure 4.10 the DNI, the thermal power and the efficiency of the collector are reported. The average value of DNI is 746 W/m^2 with maximum variation of DNI during the test of 26 W/m^2. The average efficiency of the collector, referred to the aperture area, is 69%. The rise in temperature on the collector is around four degrees as shown in figure 4.11.

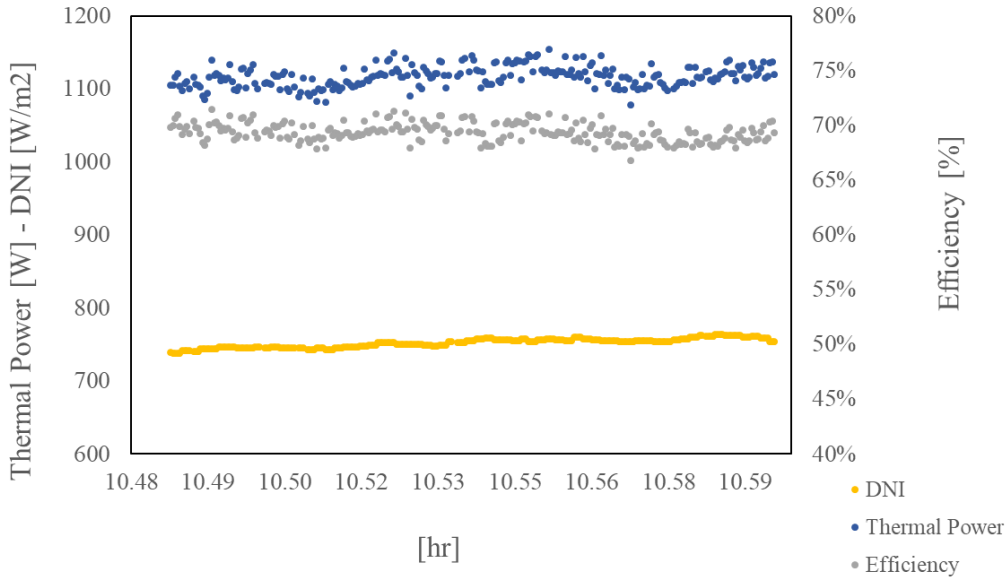

Figure 4.10: DNI, thermal power and efficiency during a peak optical efficiency test.

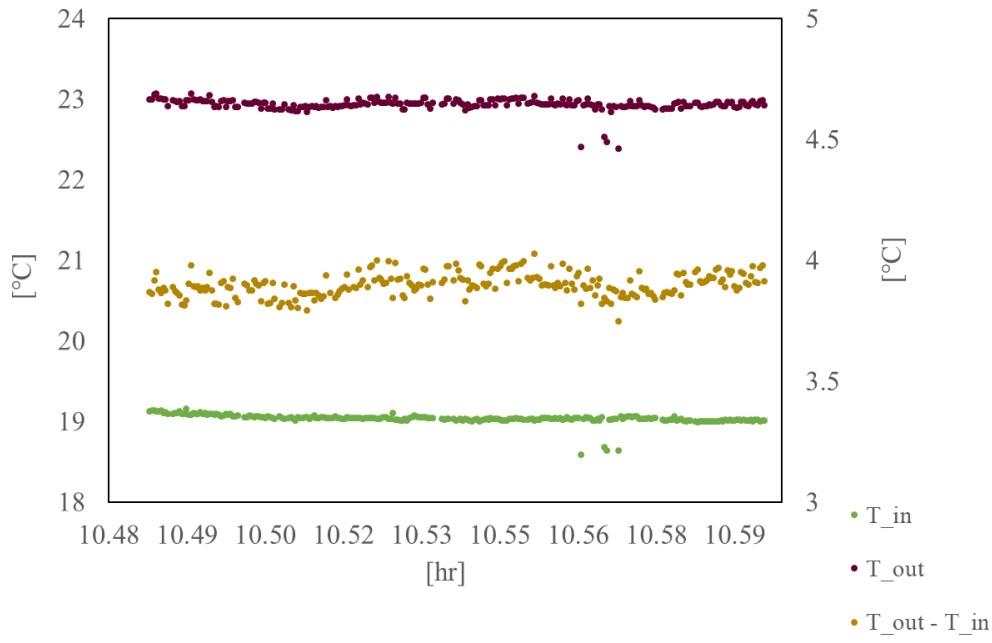

Figure 4.11: Inlet temperature, outlet temperature, difference between outlet and inlet during a peak optical efficiency test.

As can be seen in table 4.4, thanks to the control system, the inlet temperature is very stable; the average value is 19.04 °C, with extremely small deviations from the mean. The 95% of the measures of inlet temperature are at $\pm 0.06°C$ from the mean. The other variables are stable too. All the variables respect the limitations imposed by quasi-steady test (tab. 1.3).

Table 4.4: Mean, maximum, minimum value, range of data and 2 standard deviation for the peak optical efficiency test. Number of collectors under test: 3.

Variable	$DNI\left[W/m^2\right]$	$T_{amb}[^\circ C]$	$T_{in}[^\circ C]$	$\dot{V}[l/h]$	$\Delta T[^\circ C]$
Mean value	752.00	23.28	19.04	246.52	3.90
Max. value	763.20	24.77	19.15	248.74	4.03
Min. value	737.30	22.04	18.99	244.10	3.79
Range of data	25.90	2.73	0.16	4.64	0.23
2σ	12.62	1.25	0.06	1.92	0.10

4.2.2 Calculation of the uncertainty

The calculation of the errors on the measured quantities has been carried out following the rules reported in the Appendix.

The propagation of the errors for the thermal efficiency, assuming the quantities independent, is:

$$\begin{aligned} u_c^2(\eta_{th}) = &\left(\frac{\partial \eta_{th}}{\partial \dot{V}}\Delta\dot{V}\right)^2 + \left(\frac{\partial \eta_{th}}{\partial T_{in}}\Delta T_{in}\right)^2 + \left(\frac{\partial \eta_{th}}{\partial T_{out}}\Delta T_{out}\right)^2 + \\ &+ \left(\frac{\partial \eta_{th}}{\partial \rho}\Delta\rho\right)^2 + \left(\frac{\partial \eta_{th}}{\partial C_p}\Delta C_p\right)^2 + \left(\frac{\partial \eta_{th}}{\partial DNI}\Delta DNI\right)^2 \end{aligned} \tag{4.2}$$

where it has been assumed that the volume flow, and not the mass flow, is measured as in this experimental setup.

Density and specific heat are polynomial functions of the average temperature of the fluid, and so, the uncertainty on the density for instance, expliciting the dependence from average temperature is:

$$\Delta\rho = \frac{\partial \rho}{\partial T_m}\Delta T_m$$

.

Since $T_m = \frac{T_{in}+T_{out}}{2}$, the quantities are not independent and it is not correct in theory to apply equation 4.2.

The correct propagation is obtained expliciting the dependence from T_{in} (and T_{out}) of ρ and C_p and then differentiating respect T_{in} (and T_{out}). For instance:

$$\frac{\partial \eta_{th}}{\partial T_{in}} = \frac{\partial (\dot{V} \rho(T_{in}) C_p(T_{in}) T_{in})}{\partial T_{in}}$$

The equation for the combined uncertainty is:

$$u_c^2(\eta_{th}) = \left(\frac{\partial \eta_{th}}{\partial \dot{V}} \Delta \dot{V}\right)^2 + \left(\frac{\partial \eta_{th}}{\partial T_{in}} \Delta T_{in}\right)^2 + \left(\frac{\partial \eta_{th}}{\partial T_{out}} \Delta T_{out}\right)^2 + \left(\frac{\partial \eta_{th}}{\partial DNI} \Delta DNI\right)^2 \tag{4.3}$$

The number of operations to be performed in this case are much more than the uncorrelated case.

Hofer et. al. [63] have shown that using the simplified equation 4.2 instead of the correct equation 4.3, produce negligible differences.

For this reason the uncorrelated equation has been used.

In table 4.5 is reported the result of uncertainty calculation associated to thermal efficiency for the low temperature case of table 4.4.

The error associated to density has been obtained considering the uncertainty due to the average temperature and the uncertainty due to the knowledge of the fluid properties of the water $u^2(k_c)$:

$$u^2(\rho) = \left(\frac{\partial \rho}{\partial T_m}\right)^2 \cdot u^2(T_m) + \rho^2(T_m) \cdot u^2(k_c) \tag{4.4}$$

The equations used to calculated the properties of water are taken from [37]. The uncertainty of water properties is about 0.02 % [37]. The same procedure has been applied to specific heat.

Table 4.5: Calculation of the uncertainties for the case of table 4.4. The variable x_i stands for $T_{in}, T_{out}, \dot{V}, \rho, C_p, DNI$.

Variable	T_{in}	T_{out}	$\dot{V}$	ρ	C_p	DNI
$u_A(x_i)$	$0.004\,°C$	$0.005\,°C$	$0.060\,l/h$			$0.391\,W/m^2$
$u_B(x_i)$	$0.023\,°C$	$0.024\,°C$	$1.068\,l/h$			$4.308\,W/m^2$
$\left(\frac{\partial \eta_{th}}{\partial x_i} \cdot \frac{1}{\eta_{th}} \cdot u(x_i)\right)^2$	$3.5 \cdot 10^{-5}$	$3.9 \cdot 10^{-5}$	$1.8 \cdot 10^{-5}$	$4.8 \cdot 10^{-7}$	$6.5 \cdot 10^{-7}$	$1.00 \cdot 10^{-4}$

The expanded uncertainty on thermal efficiency has been obtained imposing a coverage factor $k = 2$, corresponding to a level of confidence of 95%. The results are reported in table 4.6.

Table 4.6: Example of peak efficiency test and standard error associated.

	Best estimate	Standard Error
η_{th}	69.0 %	1.9 %

The contributions to the uncertainty on thermal efficiency are reported in figure 4.12. As can be observed, in this case the major contribution to the uncertainty is due to the measurement of DNI. The uncertainty on temperature weighs for 40%. It is a relevant contribution and it is expected that it rises with temperature since the accuracy of RTD sensors decreases. Moreover, at high temperature, the temperature rise on the collector decreases due to the increase of the heat losses and therefore the measurement of temperature becomes even more critical. In order to limit the weight of temperature measurement, it has been lowered the volume flow increasing the temperature drop.

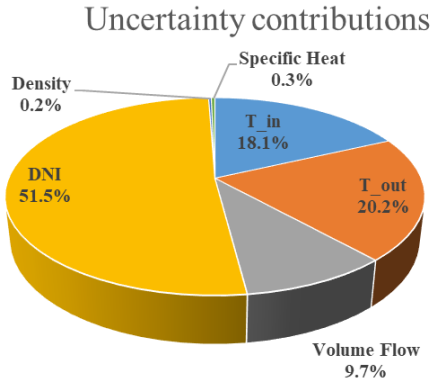

Figure 4.12: Uncertainty contributions of measured quantities to thermal efficiency.

Tests have been run to verify the minimum volumetric flow for the single collector to guarantee maximum thermal efficiency (figure 4.13). The experimental points have been obtained for similar conditions of inlet temperature, close to ambient temperature, and irradiance: $\frac{T_m - T_a}{G_b} < 0.01\,K \cdot m^2/W$ for all the experimental points. As can be seen, in the range between $30 l/h$ and $180 l/h$, corresponding to the velocity of $0.5 - 2.5\,m/s$ inside the inner tube, the thermal efficiency, considering the errors associated to the measurement, is essentially constant. In order to limit the weight of temperature measurement, it has been selected the volume flow of $45 l/h$ to have a higher temperature rise on the collector.

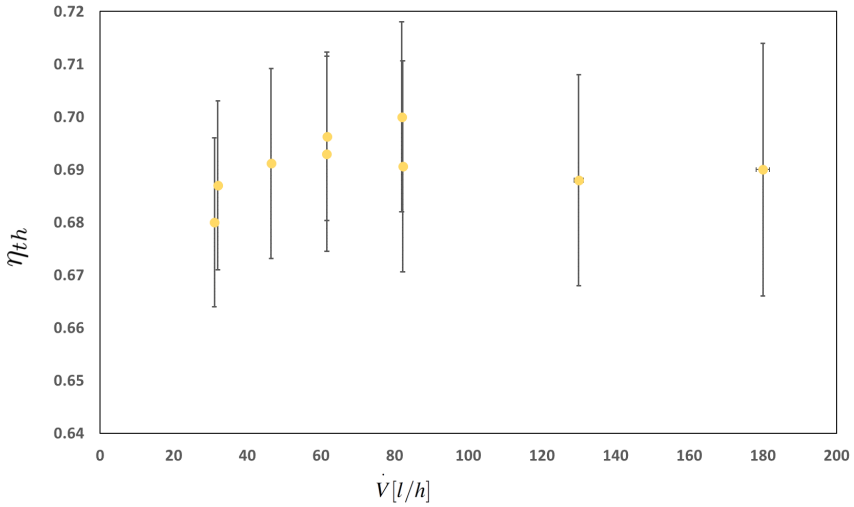

Figure 4.13: Thermal efficiency varying volumetric flow.

4.2.3 Efficiency test

Several tests have been run under different conditions of inlet temperature and of irradiance. Tests have been conducted up to a fluid temperature of 150°C with clear sky conditions. The results are reported in figure 4.14.

About 40 experimental point are shown. Each point represents a test of minimum 10 minutes of length. The errors have been calculated as reported in the section 4.2.2.

It is noted that the results are scattered, i.e. with similar boundary conditions (inlet temperature, DNI, mass flow), different outputs have been obtained. For instance, at ambient temperature several points give an estimation of efficiency of 69% and others give an estimation of 62%, outside the error bars. Furthermore, the drop in efficiency is very high: at 140°C for $800\,W/m^2$, the thermal efficiency is 55%.

In order to understand the results obtained, a comparison with the experi-

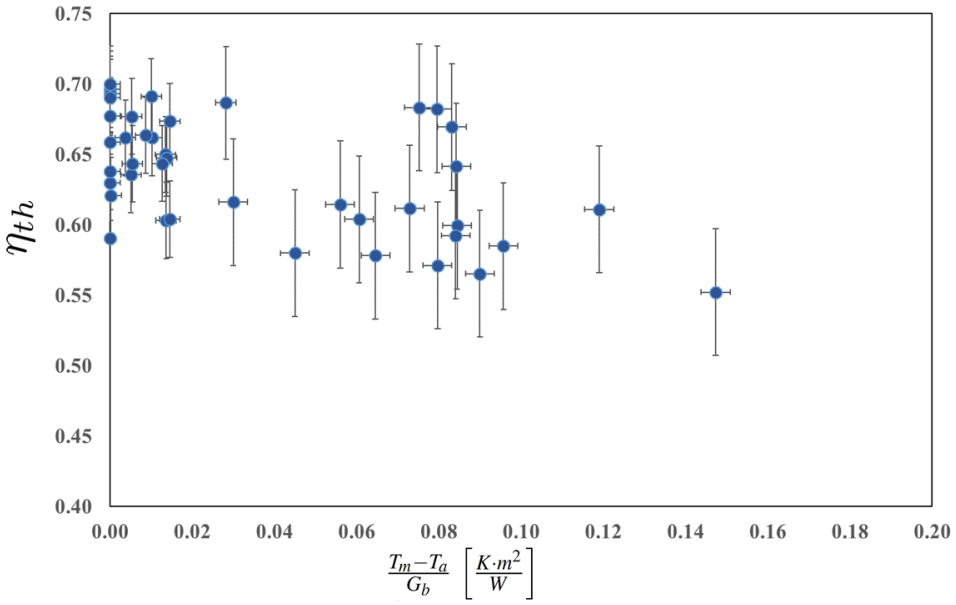

Figure 4.14: Results of the first experimental test.

mental heat loss results has been realized. Indeed, from heat loss outcomes it is possible to obtain the efficiency curve. It is worth to notice that the heat losses measured off-sun, in laboratory, can be slightly different from the heat loss measured on-sun, as reported in [39], and then, this difference can also be present for the values of efficiency obtained. The comparison between the efficiency values obtained off-sun and on-sun made here, is only to have a rough estimation of the goodness of experimental efficiency data. The efficiency curve derived from heat losses, assuming an optical efficiency of 69% and a DNI of $850\,W/m^2$ is reported in figure 4.15. As can be seen a drop in efficiency of about only 4% is expected at 150°C above ambient temperature.

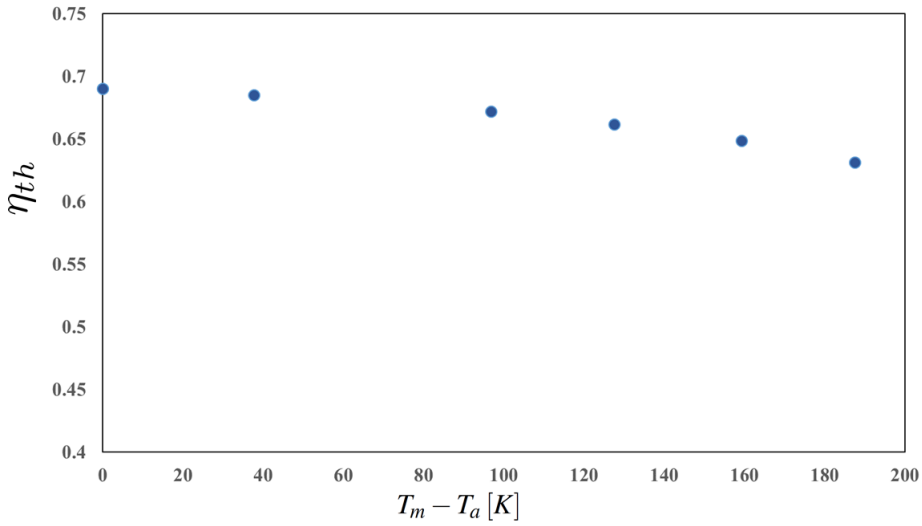

Figure 4.15: The efficiency curves obtained by heat loss results.

The two curves of efficiency for off-sun test and for on-sun test are reported in figure 4.16. As can be seen, the curves that fit the data are very far from each other and are characterized by different slopes. In general, the results of thermal efficiency test are characterized by a considerably lower efficiency. For instance a difference of about 10% in thermal efficiency, 65% against 55%, is present at 150°C of temperature difference above ambient temperature. This discrepancy between the outcomes can not be explained simply by the fact that the estimation of thermal efficiency obtained through off-sun test is a rough estimation of the real thermal efficiency. Therefore, the results of outdoor test are not in agreement with the heat loss results. The reason of this mismatch has been deeply investigated.

Several causes could have determined the discrepancy between efficiency results: optical losses, heat losses, unknown systematic errors.

First of all, since scattered results appear even at low inlet fluid temperatures, the optical losses due to tracking errors and disalignment have been investigated. During the test, it has been verified through an inclinometer that the sun sensor

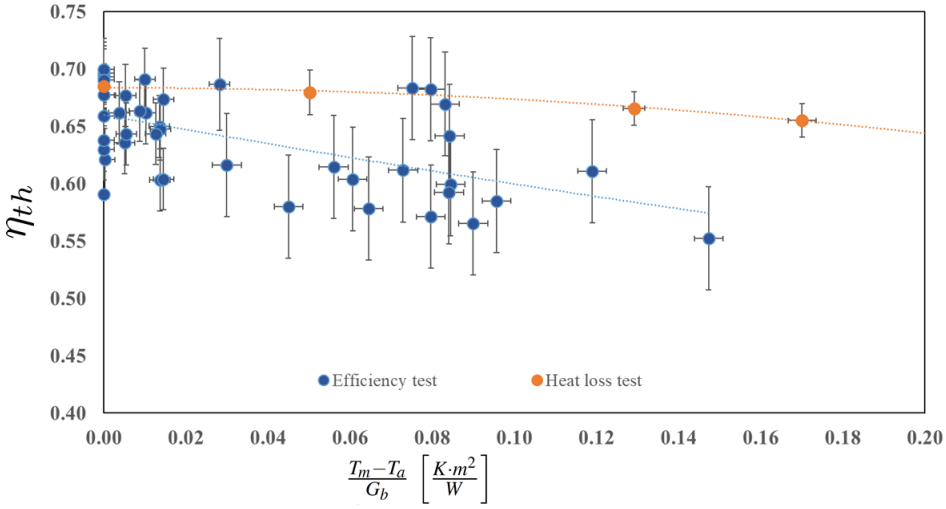

Figure 4.16: Comparison between the results from efficiency test performed outdoor and the efficiency calculated through heat loss test performed in lab.

was pointing to the sun with good accuracy ($< 0.1°$).

Since the difference in the two curves of figure 4.16 rises with temperature, it has been considered that this behavior was due to the rise of heat losses caused by to the loss of vacuum inside the receiver tube. For this reason, the conditions of the vacuum of receiver tubes have been checked. First of all, the getter inside receiver tubes was intact. Furthermore, through a IR camera the temperature of the glass tubes of receiver has been measured; an example of these measurements is reported in figure 4.17. For a fluid temperature inside the receiver of 105°C, the temperature of the glass (the black area in the figure), is about 20°C. If vacuum was lost, a temperature of the glass almost two times higher was expected as can be seen in figure 3.6.

All the receiver tubes under test have been investigated by IR camera; the measurements have shown that the vacuum had not been lost.

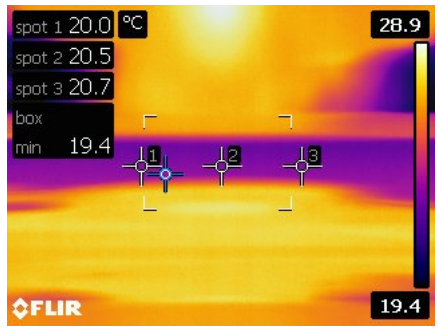

Figure 4.17: IR pictures of a small section of receiver tube.

Furthermore, analyzing the data of tests, it has been observed that the fluctuations in inlet temperature exceed the suggested limits prescribed by the standard for temperature above 80°C. In order to have a better control of inlet temperature, the resistance heater inside the tank, ruled by on/off control in the first phase of the experimental test, has been coupled to a variac. This component allows to vary continuously the tension across the resistances and so it permits to have a finer control of the thermal power delivered to the fluid inside the tank. Furthermore, due to the distance between the heat exchanger and the inlet of the collector, about 8 m, and to the heat losses along the pipes, fluctuations in temperature at the inlet of collectors were still present with the voltage regulation of the heater inside the tank. For this reason a finer control in proximity of the inlet of the collectors has been necessary. Five silicon heater mats, flexible devices made from silicon rubber, with a total power of 500W have been installed on the header pipe just before the inlet of collector where RTD sensor is placed. The supply voltage of the heater mats is controlled by a variac.

Finally, two systematic errors have been found. The former is related to the positioning of RTD sensors. RTD sensors were installed in the supply pipe and return pipe close to the inlet and the outlet of receiver tube since it was difficult to place closer to the receiver tubes. However, with this configuration a systematic error is introduced since the inlet RTD registers a temperature that is higher than the real inlet temperature of the receiver and the outlet RTD records an outlet temperature lower that the real outlet receiver temperature, underestimating the

temperature rise on the collectors. This effect is more pronounced at high temperature.

Calculating the heat losses of the header tube with the heat transfer equations [64]:

$$\dot{Q} = \frac{T_f - T_a}{R} \tag{4.5}$$

where $R = \frac{\ln(r_2/r_1)}{2\pi L k_1} + \frac{\ln(r_3/r_2)}{2\pi L k_2} + \frac{1}{hA}$.

T_f, T_a are the average fluid temperature and ambient temperature, r_1,r_2,r_3 are the internal radius of the pipe, the external radius of pipe, the external radius of the insulation material, k_1, k_2 are the thermal conductivity of copper pipe and insulation material, h is the convection heat transfer coefficient between air and the pipe, L is the length of the header tube, A is the surface area of the insulation material.

For $L = 2.3$ m and a volumetric flow of $120 l/h$, using the thermal power loss obtained from previous equation, it is possible to calculate the temperature drop along the pipe: about $0.3\,^{\circ}C$ is expected for $120\,^{\circ}C$ as inlet fluid temperature. If the temperature rise along the collector is for instance 8°C, the underestimation due to heat losses produces an error of 4%.

To solve this issue, the test bench has been slightly modified to allow the installation of new RTDs sensors closer to the receiver tubes.

Another source of systematic error has been detected in the volumetric flow sensor due to a drift in the volumetric flow measured. This phenomenon was responsible also for the scattered results at ambient temperature. Thus, the sensor has been replaced by a Coriolis flow meter sensor with an accuracy of 0.25% of reading.

After the individuation of the systematic errors and the improvements of the test rig, new tests have been run.

4.3 New results of efficiency test

In figure 4.18, the results obtained by the new tests are reported; there are 21 steady-state operation points. As can be seen, compared to the data of the previous

tests (fig. 4.14), data are less scattered. Moreover the errors associated to the measurement points are lower. The performances have been investigated up to a inlet fluid temperature of $165\,°C$. The irradiance during the tests has been in the range between $800\,W/m^2$and $950\,W/m^2$. The mass flow have been kept constant to a value of $45\,kg/h$ per collector.

The absolute errors, with a coverage factor k=2, associated to the measurement of peak optical efficiency is about 1.8%.The maximum absolute error on thermal efficiency at high temperature is around 3.5%; in the first test was 5%.

This improvement in precision is due to the major stability in temperature and to the Coriolis flowmeter.

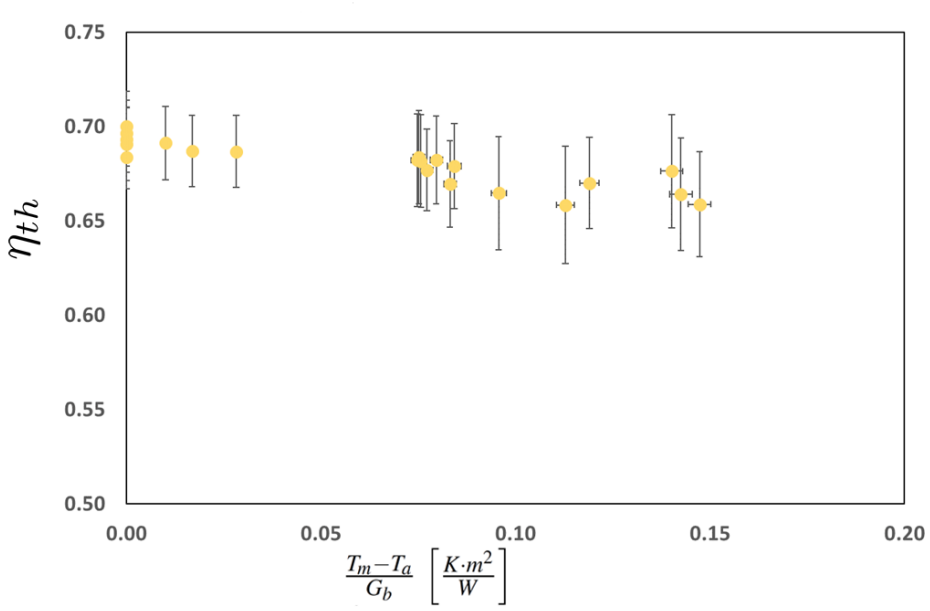

Figure 4.18: Experimental results of the new tests.

Comparing the results with the efficiency curve obtained from the heat loss test, figure 4.19, it can be observed that the experimental points are in good agree-

ment with the prevision of indoor test.

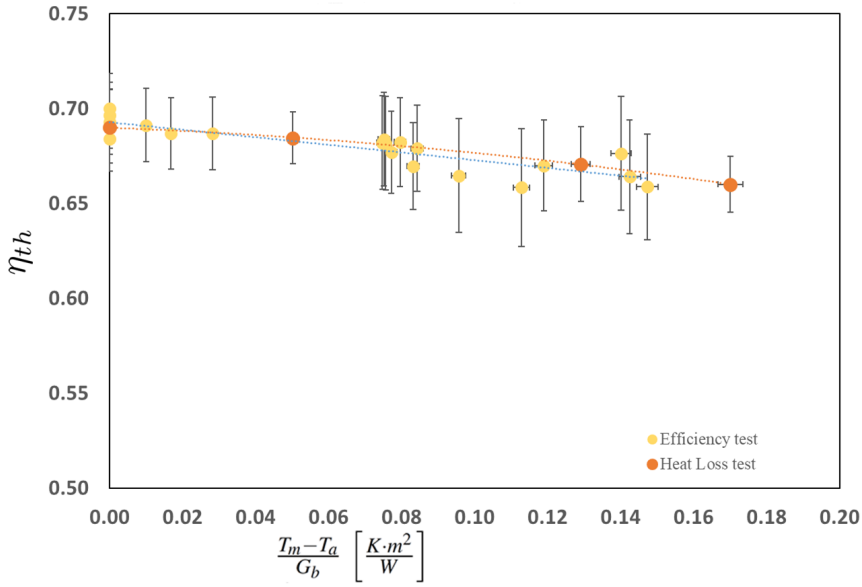

Figure 4.19: Comparison between the results from efficiency test performed outdoor and the efficiency calculated through heat loss test performed in laboratory.

4.4 Fitting of the data

The experimental data have been fitted through a multiple linear regression (MLR) based on weighted least squares (WLS) [37, 65, 66, 67, 68]. The procedure is reported in the appendix.

The regression parameters obtained are shown in table 4.7.

Table 4.7: Regression parameters and associated errors.

Parameters	Estimate	Standard Error
η_0	0.6907	0.0060
$a_1[W/(m^2K)]$	-	-
$a_2[W/(m^2K^2)]$	0.0023	0.00095

The efficiency curve of the collector is:

$$\eta_{th} = 0.6907 - 0.0023 \cdot \frac{(T_m - T_a)^2}{G_b} \tag{4.6}$$

In figure 4.20 is reported the experimental data points and the efficiency curve of the collector.

In order to calculate the thermal efficiency for a given point, the propagation of errors respect the fit parameter is needed. Also the covariance between the fit parameters is important.

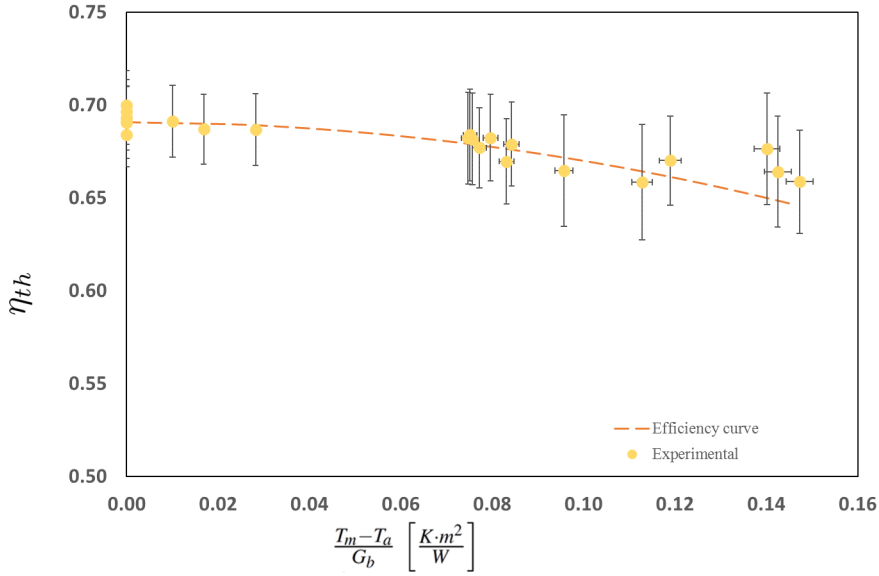

Figure 4.20: Experimental data point and efficiency curve of the collector.

As reported in the appendix, the matrix $Z = (K^T K)^{-1}$ on the diagonal, z_{jj}, contains the variances of the fit parameters, while the off-diagonal elements are the covariances ($z_{ij} = z_{ji}$) of the fitted coefficient.

The Z matrix obtained is:

$$\begin{bmatrix} 3.58 \cdot 10^{-5} & -3.45 \cdot 10^{-6} \\ -3.456 \cdot 10^{-6} & 9.03 \cdot 10^{-7} \end{bmatrix} \tag{4.7}$$

Using the expression for propagation of errors, it is possible to determine the errors associated to the thermal efficiency estimated through WLS fit.

The peak optical efficiency of the m-PTC, obtained from the efficiency curve is 69 % with an absolute error associated of 1.2%.

The uncertainty on thermal efficiency depends on the reduced temperature

difference of the operation point. The efficiency curve of the collector predicts 63% of efficiency at fluid temperature of 180°C and 1000 W/m^2, with an error associated of $\pm 4\%$. It is worth noting that this value has been extrapolated, and so it is is not a rigorous result. However, since test have been run up to 165°C, the deviations from the value calculated are expected low.

The peak optical efficiency obtained from experimental results is 69%, while the optical analysis predicted 73% for the value of the peak optical efficiency (section 2.1).

Since it has been checked that the tracking system has been working with good accuracy (section 4.2.3), the reduction of optical efficiency could be due to a decrease of the intercept factor and due to the reduction of the optical properties of the materials.

The assembly operations of the parabolic mirror on the structure have probably caused micro and macro deformations of the mirrors from the ideal parabolic shape; this has induced the increase of optical errors and the reduction of intercept factor value. This explanation is supported also by the first results of the deflectometry study made by our group of research on m-PTC that estimate an intercept factor of 90%. The reasons of the possible decrease of optical properties, transmittance of the glass and coefficient of absorption of the coating is unknown.

It can be noted that the most relevant losses of the m-PTC are optical losses, that weighs for the 31% of the losses, while the heat losses account only for 6% at 180°C. This fact suggests that the strategy to improve the performances of the collector would be based on lowering the optical losses, using a higher efficient material for the mirror.

4.5 Validation of FEM model

The termofluidodynamic model, realized to design the receiver tube, has been updated including the trend of emissivity with temperature (section 3.4) and the value of peak optical efficiency obtained from the experimental results. Numerical simulations have been run again imposing the values of the experimental points for the main boundary conditions (solar irradiance, inlet mass flow, inlet temperature, ambient temperature). The experimental results have been compared with

the numerical outcomes in order to validate the FEM model. In figure 4.21, the comparison between the experimental thermal efficiency points and the numerical ones is reported. Only seven points have been reported for clarity. As can be seen, the numerical outcomes lies in the error bars of the experimental results.

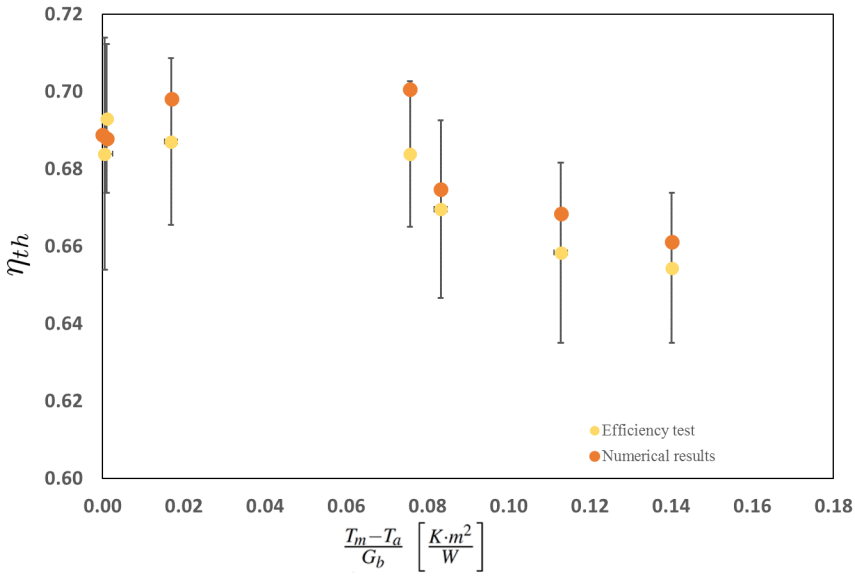

Figure 4.21: Comparison of the experimental and numerical results.

The FEM model predicts well the outlet temperature and thus the temperature rise along the collector as can be seen in table 4.8.

Therefore, the termofluidodynamic model has been validated.

Table 4.8: Experimental and numerical values of outlet fluid temperature.

$T_{in}[^{\circ}C]$	$DNI\,[W/m^2]$	$T_{out,exp}[^{\circ}C]$	$T_{out,num}[^{\circ}C]$
18.77	861	(26.89 ± 0.06)	26.85
20.22	812	(27.79 ± 0.06)	27.84
31.50	912	(39.58 ± 0.06)	39.63
81.62	801	(89.03 ± 0.08)	89.12
94.60	845	(102.25 ± 0.10)	102.30
122.08	902	(129.96 ± 0.13)	130.11
136.7	811	(143.78 ± 0.15)	143.91

Chapter 5

Evaluation of the annual performances

5.1 Production of heat at medium temperature

One of the most interesting sectors where the m-PTC could find application is the production of heat at medium temperature for industrial purposes since many industrial activities require temperature above 100 °C (table 1.1). In order to evaluate the production of heat realized by m-PTC and compare it with other solar collectors, a model in TRNSYS 17 has been developed. Two collectors have been compared to the m-PTC: the evacuated tube with compound parabolic reflector (CPC) and the linear Fresnel collector. Since there is only one small size parabolic trough that has been certified by Solar Keymark, as reported in section 1.3, and it is characterized by lower value of optical efficiency and higher value of thermal losses compared to m-PTC, it has not been used for comparison.

For the m-PTC, the model describes a module of 4 collectors connected in parallel since a modular arrangement has been considered for the installation on the roofs. In fact this arrangement, together with the one-end configuration of the receiver tube, allows in case of breaking or damage of the receiver tube easy operations of substitution without stopping the production of heat. The parameters for the efficiency curve used in simulations are taken from table 4.7; for the IAM

coefficient, the results of optical simulation with Soltrace have been used. Mutual shadows between the collectors have been determined through TRNSYS; also the end loss have been taken into account.

The evacuated tube solar collector with CPC and the linear Fresnel collector considered, represents the state of art for their technology, presenting high thermal efficiency and low thermal losses. The evacuated solar collector is the Sky Pro 18 produced by Kloben [19]. The linear Fresnel collector is LF-11 realized by Industrial Solar [5]; the absorber tube is made by Schott and is suitable to reach 400°C. The dimensions of Fresnel collector are significantly larger than m-PTC, but it has been installed on industrial roofs for process heat [5]. The features of the collectors are in table 5.1. The efficiency parameters are referred to the aperture area. The IAM equations of the collectors have been implemented in the model.

Table 5.1: Features of the m-PTC, the evacuated collector and the linear Fresnel collector.

	m-PTC	Evacuated collector	Fresnel collector
η_0	0.691	0.718	0.635
$a_1 \left[W/\left(m^2 \cdot K\right)\right]$	-	1.063	0.0265
$a_2 \left[W/\left(m^2 \cdot K^2\right)\right]$	0.0023	0.005	0.00043
Gross area $[m^2]$	3.88	3.85	30.45
Net area $[m^2]$	3.04	3.43	22

The simulations have been run for four different locations in Europe: Stockholm (59°21'N 18°04´E), Paris (48°51´N 2°21´E), Florence (43°46´N 11°15´E) and Seville (37°26´N 6°05´W), characterized by different values of global horizontal irradiance (GHI) and direct normal irradiance (DNI). It has been assumed that the collectors face the South. The evacuated tube and the m-PTC are tilted respect the horizontal plane about 15° less the latitude of the place (40° tilted for Stockholm, 30° for Paris, 25° for Florence and Seville); the linear Fresnel collector instead can not be tilted. The m-PTC and the Linear Fresnel collector have the axis of tracking aligned along North-South and they track the Sun on East-West

direction. In table 5.2, the values of GHI and DNI are reported. The weather data come from the Meteonorm database included in TRNSYS 17.

Table 5.2: Global horizontal irradiance and direct normal irradiance for the locations selected.

	Stockholm $[kWh/(m^2 \cdot yr)]$	Paris $[kWh/(m^2 \cdot yr)]$	Florence $[kWh/(m^2 \cdot yr)]$	Seville $[kWh/(m^2 \cdot yr)]$
GHI	980	1043	1447	1755
DNI	1027	793	1333	1848

Since the collectors are tilted or they follow the Sun through a one axis tracking system, the amount of radiation available on the collectors is different from the values of GHI and DNI. The global irradiance (GI) on the collector is reported for evacuated collector, and the direct normal irradiance on the collector is reported for the two concentrating collectors (tab. 5.3). The GI on the evacuated collector is higher than GHI thanks to the tilt angle. As can be seen, the DNI projected on the collector, that comprises only cosine losses for Fresnel collector and cosine losses and mutual shading for m-PTC, is considerably lower from the solar resource. It has been calculated that for m-PTC, mutual shadows between the four collectors account for a reduction of about 20% of the solar resource available during an year. Despite this reduction is relevant, if the distance between the collectors is increased the energy collected by the m-PTC decreases since gross area rises.

Table 5.3: Effective irradiance on the collectors.

	Stockholm $[kWh/(m^2 \cdot yr)]$	Paris $[kWh/(m^2 \cdot yr)]$	Florence $[kWh/(m^2 \cdot yr)]$	Seville $[kWh/(m^2 \cdot yr)]$
GI on evacuated	1199	1150	1604	1954
DNI on Fresnel	808	660	1138	1609
DNI on m-PTC	787	613	1043	1459

Assuming to produce heat at 120 °C, a constant inlet temperature of 120°C

has been fixed; the results are reported in table 5.4. Since the area of the solar collectors is different, it is reported the yearly heat produced by the solar collectors on the gross area, i.e. the area actually occupied by the collector.

Table 5.4: Comparison of the yearly heat produced at 120°C by the collectors evaluated for the locations selected.

Useful heat produced on gross area				
	Stockholm $[kWh/(m^2 \cdot yr)]$	Paris $[kWh/(m^2 \cdot yr)]$	Florence $[kWh/(m^2 \cdot yr)]$	Seville $[kWh/(m^2 \cdot yr)]$
Evacuated coll.	327	306	529	728
Fresnel coll.	333	276	486	737
m-PTC	415	325	554	782

As can be seen the m-PTC produces more heat than the other collectors for the four locations. The amount of the useful heat produced by the m-PTC rises with the amount of the DNI of the place. For this reason for high values of DNI, the benefit using m-PTC collector is more pronounced. The linear Fresnel collector, even if it presents higher efficiency than evacuated tube, for places characterized by low DNI (Paris), collects less heat since the ratio net area on gross area is low. It is interesting to note that for locations characterized by low values of DNI but with dry and cold climate, like Stockholm, concentrating collectors have considerably better performances than solar thermal ones thanks to the minor heat losses also at 120°C.

The simulations assuming the inlet temperature of 180°C are reported in table 5.5. As can be seen, the gap between the performances of the m-PTC and the evacuated tube, compared to table 5.4, rises since the m-PTC is characterized by higher efficiency at high temperature. It is noted that the m-PTC during an year, in Paris and Stockholm collects more than twice the heat of the evacuated collector thanks to the reduced heat losses at 180°C. Therefore, it can be successfully installed in cold regions for industrial process heat. In Florence and in Seville collects almost twice the heat produced by the evacuated collector.

Table 5.5: Comparison of the yearly heat produced at 180°C by the collectors evaluated for the locations selected.

	Useful heat produced on gross area			
	Stockholm $[kWh/(m^2 \cdot yr)]$	Paris $[kWh/(m^2 \cdot yr)]$	Florence $[kWh/(m^2 \cdot yr)]$	Seville $[kWh/(m^2 \cdot yr)]$
Evacuated coll.	166	151	298	444
Fresnel coll.	314	260	465	711
m-PTC	407	319	545	772

Finally, simulations have been run for an inlet temperature of 240°C and limited to the tracking collectors; the results are reported in table 5.6. Since the efficiency curve of the m-PTC collector have been extracted from data up to 165°C as inlet temperature, the results at 240°C have to be treated as approximated estimations. Even if the linear Fresnel collector is characterized by higher thermal efficiency than m-PTC at $240°C$ (60 versus 55, for $T_m - T_a = 220°C$ and $DNI = 800 W/m^2$ for normal incidence), the yearly performances are lower. This is due to lower values of optical efficiency for a large number of incidence angles described by the IAM coefficient and caused by several factors such as shading and blocking phenomenon between the mirrors. Furthermore, the incidence angle on the Fresnel collector is always higher because of the zero tilt angle of the reflective surface. The possibility to tilt the m-PTC, is the great advantage of the small size parabolic trough realized compared to Fresnel collectors.

Table 5.6: Comparison of the yearly heat produced at 240°C by the two collectors evaluated for the locations selected.

	Useful heat produced on gross area			
	Stockholm $[kWh/(m^2 \cdot yr)]$	Paris $[kWh/(m^2 \cdot yr)]$	Florence $[kWh/(m^2 \cdot yr)]$	Seville $[kWh/(m^2 \cdot yr)]$
Fresnel coll.	291	241	432	678
m-PTC	397	309	534	759

The analysis has permitted to show that m-PTC collects more energy than the other kinds of solar collectors. For 120°C as temperature process, for places with low- medium value of DNI there are little advantages in the production of heat using the m-PTC instead the evacuated tube; instead in cold and dry climate m-PTC is beneficial since it produces 25% of heat more than evacuated collector.

If the temperature of the process is higher, the gap between the performances of the collectors rises considerably. At 180°C, for Seville, the m-PTC produces 74% heat more than evacuated tube and about 9% more comparing it with the linear Fresnel. Rising the fluid inlet temperature up to 240°C, the m-PTC collects more useful heat respect the linear Fresnel collector: 36% more in Stockholm, 23% more in Florence, 11% more in Seville. Moreover, the dimensions of the Fresnel collector do not permit to integrate it in all the industrial contexts.

For these reasons, the m-PTC designed and realized turns out to be an interesting technology to produce heat at medium temperature (> 120°C). Besides, it has been proved with the numerical results that the installation of m-PTC for the production of heat at medium temperature is advantageous compared to the other technologies both for places in Europe with high values of DNI and for location with limited solar resource.

Furthermore, it has been compared the performances of the collectors for low temperature (80°C). The results are reported in figure 5.7. As expected, the evacuated collects more energy for all the location selected. This is due to the higher solar resource available for the thermal collector respect the concentrating collectors together with the low impact of heat losses at this range of temperature.

Table 5.7: Comparison of the yearly heat produced at 80°C by the four collectors evaluated for the locations selected.

Useful heat produced on gross area				
	Stockholm $[kWh/(m^2 \cdot yr)]$	Paris $[kWh/(m^2 \cdot yr)]$	Florence $[kWh/(m^2 \cdot yr)]$	Seville $[kWh/(m^2 \cdot yr)]$
Evacuated coll.	458	436	701	915
Fresnel coll.	345	288	498	750
m-PTC	419	329	558	786

5.2 Estimated costs

The cost sharing of the components of the prototype of m-PTC has been estimated and it is reported in table 5.8:

Table 5.8: Cost of one m-PTC module (four collectors).

Components	Cost [%]
Collectors	30
Receiver tubes	14
Frame	40
Actuators	16

As can bee seen the frame has a big impact on the final costs, about 40%.

The total cost of m-PTC has been estimated to be about $500\,\text{euro}/\text{m}^2$. The target cost of this collector should be around $300-350\,\text{euro}/\text{m}^2$ to be competitive against non-tracking collectors, therefore at moment the total costs are higher. Anyway, it is worth to notice that the m-PTC realized is only a prototype and a strong decrease of the costs can be expected in case of the industrialization of the product.

Chapter 6

Conclusions and future perspectives

The study has dealt with the design, the realization and the experimental test of an innovative small size parabolic trough collector, called m-PTC, suitable to produce heat at medium temperature ($100 - 250°C$) and to be integrated in the roof of industrial environments where the space for installation of solar collectors is in general limited.

The design phase that has preceded the realization of the prototype, has allowed to fix and optimize the main parameters of the system through the development of numerical models. The optical analysis, through Monte Carlo ray tracing technique, has permitted to optimize the dimensions of the collector components: the width of the parabolic mirror and the diameter of receiver tube have been fixed. Through the analysis of the optical errors, the optimum rim angle of the parabola has been selected. The radiation distribution on the absorber tube has been calculated and used as boundary condition in the finite element model of the receiver tube. A termofluidodynamic FEM model of the receiver tube has been realized to fully understand the physics of the system and identify the relevant parameters. An optimization analysis has been carried out to fix the main components of the receiver tube such as absorber material and coating emissivity. The numerical model has allowed to obtain details, such as the optimal mass flow and

the rise in temperature along the collector, that have been used for the realization of the prototype and for the design of the test rig for outdoor test. A structural finite element model has been realized in order to compute the thermal stress on the absorber tube.

Following the indications of the numerical models the prototype of an innovative parabolic trough collector has been realized. First of all, the m-PTC collector is innovative for its dimensions: it is characterized by extremely small size since it has been designed to be suitable for the integration on the roofs of industrial environments where the space for installation of solar collectors is in general limited. For these reasons, it is much more compact and transportable respect than the parabolic trough collectors developed to date. It possesses an aperture width of just 420 mm and it is 1800 mm long. The parabolic mirror has a rim angle of 100° that permits to reduce the weight of optical errors and to increase the acceptance angle of the reflected radiation. The concentration ratio of the collector, the ratio between the area of the mirror against the area of the absorber, is 14. The receiver tube, characterized by an external diameter of 10 mm, has been realized by a highly specialized company operating in the sector of solar collectors. Another relevant aspect of the m-PTC is that the collector aims to achieve performances higher than solar thermal collectors in the temperature range of $100 - 250$°C. This has been made possible thanks to the thermal properties of the evacuated receiver tube, to the high quality of the materials used for the receiver tube (e.g. the selective coating) and thanks to the design solutions adopted. Furthermore, the receiver is characterized by a configuration formed by two concentric tubes so that the fluid inlet and output are at the same side (one-end receiver). This configuration presents several advantages respect the standard one since it is more robust, more simple to realize and less expensive since it possesses fewer number of sealings.

An indoor test rig has been realized to test the thermal performances and to verify the good quality of the receiver. The measurement technique of heat losses is based on Joule effect. For an absorber temperature of 180°C it has been measured 23.5 W of heat loss. This result has confirmed the good quality of the receiver tube. Through the comparison of the experimental results with the FEM model, the estimate of coating emissivity with temperature has been obtained.

In order to fully characterize the collector, a test rig for outdoor test on the parabolic collector has been designed. The test bench has been carefully projected

in order to satisfy the requirements imposed by the standard test on solar concentrating collector and the measurement instrumentation has been properly selected in order to minimize the uncertainty on the useful thermal power and on the thermal efficiency of the collector. The parabolic collectors have been mounted on a rotating platform in order to track the Sun with a two axis tracking system have the condition of zero incidence angle of the beam radiation on the aperture plane of the collectors.

Test have been run for different temperatures and different conditions of irradiance. An accurate analysis of the measurement uncertainties has been conducted; it has permitted to improve the test bench and the accuracy of measured variables.

The outcomes of test have been compared to the results of heat loss test carried out in laboratory and it has been verified that were in good agreement. The maximum experimental uncertainty on thermal efficiency is 3.5%. The data have been fitted through a multiple linear regression based on weighted least squares.

The peak optical efficiency of the m-PTC has been estimated to be 69%. The efficiency curve of the collector has been obtained, estimating $63 \pm 4\%$ of thermal efficiency at 180°C, significantly higher than the efficiency reported in literature for CPC collectors and for parabolic trough collector with an aperture width under 1 m.

The comparison of the experimental results with the numerical outcomes of the termofluidodynamic FEM model, has permitted to validate the model since all the numerical results lies in the experimental error bars.

An analysis with TRNSYS has been realized to evaluate the yearly performances of the m-PTC and to compare it with other solar collectors. It turns out that m-PTC is more efficient and produces more heat at medium temperature (>120°C) for all the locations analyzed. In particular at 180°C it collects respectively 74% and 9% more than the evacuated tube and the linear Fresnel collector for a location with $1850\,W/m^2$ of DNI. Furthermore, from numerical results, the installation of m-PTC is interesting also for locations characterized by high latitude and dry climate since m-PTC can be easily mounted tilted. Finally, based on the components and the materials used, the cost sharing and the total costs of m-PTC have been reported (about $500\,\text{euro}/\text{m}^2$).

In light of the results, the m-PTC realized has proven to be suitable to produce heat at medium temperature with high efficiency. Thanks to the design, the col-

lector overcomes the main limitations of concentrating collectors for process heat, being small, easy to integrate on the roofs and easy to maintain.

For what concerns the future activities on the m-PTC, they will be directed to new experimental tests, addressed to the reduction of the components of the collector and to the improvements of the performance of the collector. It is planned to complete the characterization of the collector running tests up to $200\,^{\circ}C$, measuring the performances of the collector varying the incidence angle and performing the dynamic test method on the collector. Indeed, since one of the main disadvantages of the prototype realized is the high number of the mechanical parts, it is foreseen the realization of a new prototype which the bearing structure is formed by composite materials, glass fibers and polyester resin. This could allows to realize a structure with a minor number of parts, easy to assemble and less time consuming for the mounting. The simplification in the structure is expected to bring also a relevant reduction of the costs of collector. Finally, since the major part of the losses is due to optical losses, around 31% at moment, new materials for the components will be investigated in order to improve the performances of the collector. In particular, the aluminum mirror could be replaced with a polymer based silver film, 0.1 mm thick, suitable for this application with a higher value of specular reflection coefficient (94%).

Bibliography

[1] IEA. IEA, Key world energy statistics. Retrieved october 2018. *http://www.iea.org/*.

[2] IPCC Report 2018. Retrieved october 2018. *http://www.ipcc.ch/*.

[3] Christopher B Field, Vicente R Barros, DJ Dokken, KJ Mach, MD Mastrandrea, TE Bilir, M Chatterjee, KL Ebi, YO Estrada, RC Genova, et al. Ipcc, 2014: Climate change 2014: Impacts, adaptation, and vulnerability. part a: Global and sectoral aspects. contribution of working group ii to the fifth assessment report of the intergovernmental panel on climate change, 2014.

[4] Renewables Ren21 et al. Global status report. *REN21 secretariat, Paris*, 2016, 2016.

[5] Pedro Horta and ISE FhG. Process heat collectors: State of the art and available medium temperature collectors. *Solar Process Heat for Production and Advanced Applications. IEA SHC Task*, 49, 2015.

[6] Md Tasbirul Islam, Nazmul Huda, AB Abdullah, and R Saidur. A comprehensive review of state-of-the-art concentrating solar power (csp) technologies: Current status and research trends. *Renewable and Sustainable Energy Reviews*, 91:987–1018, 2018.

[7] F Dinter and D Mayorga Gonzalez. Operability, reliability and economic benefits of csp with thermal energy storage: first year of operation of andasol 3. *Energy Procedia*, 49(0):2472–2481, 2014.

[8] DNI map. Retrieved october 2018. *https://solargis.com/maps-and-gis-data/overview*.

[9] A Fernandez-Garcia, E Zarza, La Valenzuela, and M Perez. Parabolic-trough solar collectors and their applications. *Renewable and Sustainable Energy Reviews*, 14(7):1695–1721, 2010.

[10] Anouk Honoré. Decarbonisation of heat in europe: implications for natural gas demand. 2018.

[11] N ECOHEATCOOL Werner, S Constantinesku et al. The european heat market: Workpackage 1. *Final Rep. Brussels: Euroheat & Power*, 2006.

[12] Soteris A Kalogirou. *Solar energy engineering: processes and systems*. Academic Press, 2013.

[13] Qiyuan Li, Cheng Zheng, Ali Shirazi, Osama Bany Mousa, Fabio Moscia, Jason A Scott, and Robert A Taylor. Design and analysis of a medium-temperature, concentrated solar thermal collector for air-conditioning applications. *Applied Energy*, 190:1159–1173, 2017.

[14] FJ Cabrera, A Fernandez-Garcia, RMP Silva, and M Perez-Garcia. Use of parabolic trough solar collectors for solar refrigeration and air-conditioning applications. *Renewable and Sustainable Energy Reviews*, 20:103–118, 2013.

[15] IRENA IEA ETSAP. Solar heat for industrial processes-technology brief. Technical report, Tech. Rep, 2015.

[16] Aránzazu Fernández-García, Loreto Valenzuela, Eduardo Zarza, Esther Rojas, Manuel Pérez, Quetzalcoatl Hernández-Escobedo, and Francisco Manzano-Agugliaro. Small-sized parabolic-trough solar collectors: Development of a test loop and evaluation of testing conditions. *Energy*, 152:401–415, 2018.

[17] TVP solar collector. Retrieved october 2018. *https://www.tvpsolar.com/*.

[18] Roland Winston, Lun Jiang, and Bennett Widyolar. Performance of a 23kw solar thermal cooling system employing a double effect absorption chiller and thermodynamically efficient non-tracking concentrators. *Energy Procedia*, 48:1036–1046, 2014.

[19] Kloben Sky Pro solar collector. Retrieved october 2018. *www.kloben.it*.

[20] KC Amanul Alam, Bidyut Baran Saha, and Atsushi Akisawa. Adsorption cooling driven by solar collector: a case study for tokyo solar data. *Applied Thermal Engineering*, 50(2):1603–1609, 2013.

[21] Inersur Linear Fresnel Collector. Retrieved october 2018. *http://www.inersur.com*.

[22] Aránzazu Fernández-García, Esther Rojas, Manuel Pérez, Ricardo Silva, Quetzalcoatl Hernández-Escobedo, and Francisco Manzano-Agugliaro. A parabolic-trough collector for cleaner industrial process heat. *Journal of Cleaner Production*, 89:272–285, 2015.

[23] N Janotte, S Meiser, D Krüger, E Lüpfert, R Pitz-Paal, S Fischer, and H Müller-Steinhagen. Quasi-dynamic analysis of thermal performance of parabolic trough collectors. In *SolarPACES 2009, 15th Solar Power And Chemical Energy Systems International Symposium*, pages 15–19, 2009.

[24] PTC Power Trough 110. Retrieved october 2018. *https://inventivepower.com*.

[25] Parabolic Trough Collector Trivelli energia. Retrieved october 2018. *http://www.seagroupe.com/*.

[26] Luigi Crema, Fabrizio Alberti, Ewa Wackelgard, Barbara Rivolta, Sebastian Hesse, Lorenzo Luminari, Drummond Hislop, and Brian Restall. Novel system for distributed energy generation from a small scale concentrated solar power. *Energy Procedia*, 57:447–456, 2014.

[27] Parabolic trough collector. IT Collect. Retrieved october 2018. *www.drvetter.de*.

[28] Database for applications of solar heat integration in industrial processes. Retrieved october 2018. *http://ship-plants.info/*.

[29] Institut fur Solarforschung enerMENA. Advanced csp teaching materials. Technical report, DLR, 2012.

[30] Michael DiGrazia, Randy Gee, and Gary Jorgensen. Reflectech® mirror film attributes and durability for csp applications. In *ASME 2009 3rd International Conference on Energy Sustainability collocated with the Heat Transfer and InterPACK09 Conferences*, pages 677–682. American Society of Mechanical Engineers Digital Collection, 2009.

[31] I Mack and JP Rossy. Cst receiver tube qualification, phase 1, investigation-final report. 2010.

[32] John A Duffie and William A Beckman. *Solar engineering of thermal processes*. John Wiley & Sons, 2013.

[33] En 12975-2. thermal solar systems and components - collectors - part 2: test methods. Technical report, Brussels: European committee for standardization (CEN), 2006.

[34] Astm. e905-e987: standard test method for determining thermal performance of tracking concentrating solar collectors. Technical report, Pennsylvania: American Society for Testing and Materials International (ASTM), 2010.

[35] Srcc standard 600. test methods and minimum standards for certifying solar concentrating collectors. Technical report, Florida: Solar Rating and Certification Corporation (SRCC), 2010.

[36] Ansi/asharae standard 93. methods of testing to determine the thermal performance of solar collectors. Technical report, Atlanta: American Society of Heating, Refrigerating and Air-Conditioning Engineers (ASHRAE), 2003.

[37] Iso 9806. solar energy e solar thermal collectors e test methods. Technical report, Geneva: International Organization for Standardization (ISO), 2013.

[38] Vernon E Dudley, Gregory J Kolb, A Roderick Mahoney, Thomas R Mancini, Chauncey W Matthews, Michael Sloan, and David Kearney. Test results: Segs ls-2 solar collector. *Nasa Sti/recon Technical Report N*, 96, 1994.

[39] Vernon E Dudley, Lindsey R Evans, and Chauncey W Matthews. Test results, industrial solar technology parabolic trough solar collector. Technical report, Sandia National Labs., Albuquerque, NM (United States), 1995.

[40] Tiago Osório and Maria Joao Carvalho. Testing of solar thermal collectors under transient conditions. *Solar Energy*, 104:71–81, 2014.

[41] Stephan Fischer, Eckhard Lüpfert, and Hans Müller-Steinhagen. Efficiency testing of parabolic trough collectors using the quasi-dynamic test procedure according to the european standard en 12975. In *SolarPACES 13th Symposium on Concentrating Solar power and Chemical Energy Technologies*, 2006.

[42] Marco Larcher, Matthias Rommel, Andreas Bohren, Elimar Frank, and Stefan Minder. Characterization of a parabolic trough collector for process heat applications. *Energy Procedia*, 57:2804–2811, 2014.

[43] Peter Heller, Mirko Meyer-Grünefeldt, Miriam Ebert, Nicole Janotte, Bijan Nouri, Klaus Pottler, Christoph Prahl, Wolfgang Reinalter, and Eduardo Zarza. Kontas–a rotary test bench for standardized qualification of parabolic trough components. In *17th SolarPACES International Symposium on Concentrated Solar Power and Chemical Energy Technologies, Granada, Spain*, 2011.

[44] G Pierucci, D Fontani, P Sansoni, and M De Lucia. Shape optimization for parabolic troughs working in non-ideal conditions. *Energy Procedia*, 57:2231–2240, 2014.

[45] Tim Wendelin, Aron Dobos, and Allan Lewandowski. Soltrace: a ray-tracing code for complex solar optical systems. *Contract*, 303:275–3000, 2013.

[46] Laura Galuppi and Gianni Royer-Carfagni. Optimal cold bending of laminated glass. *International Journal of Solids and Structures*, 67:231–243, 2015.

[47] Moncef Balghouthi, Abdessalem Bel Hadj Ali, Seif Eddine Trabelsi, and Amenallah Guizani. Optical and thermal evaluations of a medium temperature parabolic trough solar collector used in a cooling installation. *Energy Conversion and Management*, 86:1134–1146, 2014.

[48] Ari Rabl. *Active solar collectors and their applications*. Oxford University Press on Demand, 1985.

[49] ZD Cheng, YL He, Jie Xiao, YB Tao, and RJ Xu. Three-dimensional numerical study of heat transfer characteristics in the receiver tube of parabolic trough solar collector. *International Communications in Heat and Mass Transfer*, 37(7):782–787, 2010.

[50] Ricardo Vasquez Padilla, Gokmen Demirkaya, D Yogi Goswami, Elias Stefanakos, and Muhammad M Rahman. Heat transfer analysis of parabolic trough solar receiver. *Applied Energy*, 88(12):5097–5110, 2011.

[51] Ya-Ling He, Jie Xiao, Ze-Dong Cheng, and Yu-Bing Tao. A mcrt and fvm coupled simulation method for energy conversion process in parabolic trough solar collector. *Renewable Energy*, 36(3):976–985, 2011.

[52] ZD Cheng, YL He, FQ Cui, RJ Xu, and YB Tao. Numerical simulation of a parabolic trough solar collector with nonuniform solar flux conditions by coupling fvm and mcrt method. *Solar Energy*, 86(6):1770–1784, 2012.

[53] AA Hachicha, I Rodríguez, R Capdevila, and A Oliva. Heat transfer analysis and numerical simulation of a parabolic trough solar collector. *Applied energy*, 111:581–592, 2013.

[54] Zhiyong Wu, Shidong Li, Guofeng Yuan, Dongqiang Lei, and Zhifeng Wang. Three-dimensional numerical study of heat transfer characteristics of parabolic trough receiver. *Applied energy*, 113:902–911, 2014.

[55] Weidong Huang, Peng Hu, and Zeshao Chen. Performance simulation of a parabolic trough solar collector. *Solar Energy*, 86(2):746–755, 2012.

[56] Frank Burkholder, Michael Brandemuehl, Henry Price, Judy Netter, Chuck Kutscher, and Ed Wolfrum. Parabolic trough receiver thermal testing. In *ASME 2007 Energy Sustainability Conference*, pages 961–970. American Society of Mechanical Engineers, 2007.

[57] Frank Burkholder and Charles F Kutscher. *Heat-loss testing of Solel's UVAC3 parabolic trough receiver*. Citeseer, 2008.

[58] Frank Burkholder and Charles F Kutscher. *Heat loss testing of Schott's 2008 PTR70 parabolic trough receiver*. Citeseer, 2009.

[59] José M Márquez, Rafael López-Martín, Loreto Valenzuela, and Eduardo Zarza. Test bench heatrec for heat loss measurement on solar receiver tubes. In *AIP Conference Proceedings*, volume 1734, page 030025. AIP Publishing, 2016.

[60] G Hoste and N Schuknecht. Thermal efficiency analysis of skyfuel's advanced, large-aperture, parabolic trough collector. *Energy Procedia*, 69:96–105, 2015.

[61] Sebastian Dreyer, Paul Eichel, Tim Gnaedig, Zdenek Hacker, Sebastian Janker, Thomas Kuckelkorn, Kamel Silmy, Johannes Pernpeintner, and Eckhard Luepfert. Heat loss measurements on parabolic trough receivers. *16th SolarPACES, Perpignon, France*, page 8, 2010.

[62] Eckhard Lüpfert, Klaus-J Riffelmann, Henry Price, Frank Burkholder, and Tim Moss. Experimental analysis of overall thermal properties of parabolic trough receivers. *Journal of solar energy engineering*, 130(2):021007, 2008.

[63] Annie Zirkel-Hofer, Stephen Perry, Sven Fahr, Korbinian Kramer, Anna Heimsath, Stephan Scholl, and Werner Platzer. Improved in situ performance testing of line-concentrating solar collectors: Comprehensive uncertainty analysis for the selection of measurement instrumentation. *Applied energy*, 184:298–312, 2016.

[64] Yunus A Cengel. *Heat and mass transfer*. Tata McGraw-Hill Education, 2007.

[65] Christian Müller-Schöll and Ueli Frei. Uncertainty analyses in solar collector measurement. *Tc*, 1000:7, 2000.

[66] V Sabatelli, D Marano, G Braccio, and VK Sharma. Efficiency test of solar collectors: uncertainty in the estimation of regression parameters and sensitivity analysis. *Energy Conversion and Management*, 43(17):2287–2295, 2002.

[67] Manfred Georg Kratzenberg, Hans Georg Beyer, and Sergio Colle. Uncertainty calculation applied to different regression methods in the quasi-dynamic collector test. *Solar Energy*, 80(11):1453–1462, 2006.

[68] Nicole Janotte, Eckhard Lüpfert, Robert Pitz-Paal, Klaus Pottler, Markus Eck, Eduardo Zarza, and Klaus-Jürgen Riffelmann. Influence of measurement equipment on the uncertainty of performance data from test loops for concentrating solar collectors. *Journal of Solar Energy Engineering*, 132(3):031003, 2010.

[69] IEC ISO and BIPM OIML. Guide to the expression of uncertainty in measurement. *Geneva, Switzerland*, 1995.

Appendix

Error theory

According to the Guide to the Expression of Uncertainty in Measurement [69] two types of uncertainty are generally distinguished: type A for experimental data that is characterized by repeated measurements of a quantity and type B for non-experimental data obtained from other sources such as experience or knowledge of the system or previously evaluated measurement data [68]. The two types of uncertainty are evaluated separately in terms of best estimate x_i and standard uncertainty u_i that fully describe the data.

Type A. For n repeated measurements under the same conditions, the best estimate for the expected value of the quantity is their arithmetic mean $\bar{x}_i$:

$$\bar{x}_i = \frac{\sum_{k=1}^{n} x_{ik}}{n} \tag{1}$$

and the uncertainty is the standard deviations of the mean:

$$u_A(x_i) = \left(\frac{\sum_{k=1}^{n} (x_{ik} - \bar{x}_i)^2}{n(n-1)} \right)^{1/2} \tag{2}$$

Type B uncertainty $u_B(x_i)$ derives from a combination of uncertainties over the whole measurement chain, taking into account all available data, such as sensor uncertainty, data logger uncertainty, uncertainty resulting from the possible differences between the measured values perceived by the measuring device. Relevant information should be obtained from calibration certificates or other technical data related to the devices used. They often state resulting uncertainties either in terms of standard deviations or ranges about the measurement values. While the first can be directly included into an uncertainty budget, the latter requires transformation: if there is no additional information about the frequency distribution of values within the stated bounds $[a_-, a_+]$, the most suitable way of including all available information is by describing it with a rectangular distribution. The standard uncertainty is:

$$u_i = \frac{a}{\sqrt{3}} \tag{3}$$

if $a_- = a_+ = a$.

The two kind of errors, A and B, are summed via root sum squared:

$$u(x_i) = \left(u_A^2 + u_B^2\right)^{1/2} \tag{4}$$

In most cases a measured y is determined indirectly from P other directly measured quantities $x_1, x_2, .., x_P$ through a functional relationship $y = f(x_1, x_2, .., x_P)$. The standard uncertainty in the estimate y is given by the law of error propagation:

$$u_c(y) = \left(\sum_{i=1}^{P} \left(\frac{\partial f}{\partial x_i}\right)^2 \cdot u^2(x_i) + 2\sum_{i=1}^{P-1}\sum_{j=i+1}^{P} \frac{\partial f}{\partial x_i}\frac{\partial f}{\partial x_j} cov(x_i, x_j)\right)^{1/2} \tag{5}$$

If the quantities are uncorrelated the covariances are zero.

An example of such indirect determination in the case of PTC collector efficiency testing is the determination of instantaneous efficiency η, which derives

from the values of direct solar irradiance in the collector level G_b, fluid mass flow rate, temperature difference ΔT, collector area A and specific heat capacity C_P. Thus, in this case the standard uncertainty $u(\eta_i)$ in each value η_i of instantaneous efficiency is calculated by the combination of standard uncertainties in the values of the primary measured quantities, taking into account their relation to the derived quantity η.

The expanded uncertainty U defines an interval about the measurement value expected to encompass a large fraction of the distribution of values that could be reasonably attributed to the measurand:

$$U = ku_c(y)$$

The difficulty of the above approach lies in determining the coverage factor k, which itself depends on the yet unknown distribution of the measurand y. On the assumption of sufficiently large numbers of normally distributed results a coverage of 2 covered fraction of 0.95 is obtained for k=2 [68].

Fitting and uncertainties

The basic target of solar collector efficiency testing is the determination of the collector efficiency by measurements under specific conditions [37]. More specifically, it is assumed that the behaviour of the collector can be described by a M-parameter single node, steady-state or quasi-dynamic model:

$$\eta = c_1 x_1 + c_2 x_2 + .. + c_M x_M \tag{6}$$

where η is the collector instantaneous efficiency $x_1, x_2, .., x_M$ are quantities, the values of which are determined experimentally through testing $c_1, c_2, .., c_M$ are characteristic constants of the collector that are determined through testing.

In the case of the steady-state model, for example, M = 3, $c_1 = \eta_0$, $c_2 = a_1$, $c_3 = a_2$, $x_1 = 1$, $x_2 = \frac{(T_m - T_a)}{G_b}$ and $x_3 = \frac{(T_m - T_a)^2}{G_b}$. During the experimental phase, the output, solar energy and the basic climatic quantities are measured in J steady-state or quasi-dynamic state points, depending on the model used. From these

primary measurements the values of parameters η, $x_1, x_2, .., x_M$ are derived for each point of observation j, j = 1...J. Generally, the experimental procedure of the testing leads to a formation of a group of J observations which comprise, for each one of the J testing points, the values of η_j, $x_{j1}, x_{j2}, .., x_{jM}$. For the determination of uncertainties, it is essential to calculate the respective combined standard uncertainties $u(\eta_j)$, $u(x_{j1}), u(x_{j2}), .., u(x_{jM})$ in each observations point.

During analysing the data a least square fitting of the model formula is performed, in order to determine the values of coefficients $c_1, c_2..c_M$ for which the model of eq. 6 represents the series of J observations with the greatest accuracy. Since in reality the typical deviation is almost never constant and the same for all observations, but each data point (η_j, $x_{j1}, x_{j2}, .., x_{jM}$) has its own standard deviation σ_j, an interesting solution is the use of the weighted least square (WLS) method, which calculates, on the base of the measured values and their uncertainties, not only the model parameters but also their uncertainty.

In the case of WLS, the maximum likelihood estimate of the model parameters is obtained by minimizing the chi-squared function:

$$\chi^2 = \sum_{j=1}^{J} \frac{(\eta_j - (c_1 x_{j1} + c_2 x_{j2} + .. + c_M x_{jM}))^2}{u_j^2} \tag{7}$$

where u_j^2 is the variance:

$$u_j^2 = \left((u(\eta_j))^2 + c_1^2 u(x_{j1})^2 + c_2^2 u(x_{j2})^2 + .. + c_M^2 u(x_{jM})^2 \right)^2 \tag{8}$$

Finding coefficients $c_1, c_2..c_M$ and their standard uncertainties by minimizing chi-squared function is complicated, because of the non linearity present in equation 7. A strategy is therefore to find these uncertainties numerically.

Let K be a matrix whose JxM components k_{jm} are constructed from M basic functions evaluated at the J experimental values of $x_1, x_2, .., x_M$ weighted by the uncertainty u_j:

$k_{jm} = \frac{x_{jm}}{u_j}$

Let also L be a vector of length J whose components l_j are constructed from values of η_j to be fitted, weighted by the uncertainty u_j: $l_j = \frac{\eta_j}{u_j}$.

The normal formula of the least square problem can be written:

$$\left(K^T K\right) \cdot C = K^T L \tag{9}$$

where C is a vector whose elements are the fitted coefficients. Given the fact that for the calculation of variances u_j the knowledge of coefficients $c_1, c_2..c_M$ is needed, a possible solution is to use the values of coefficients calculated by standard least squares fitting as the initial values. These initial values can be used in equation 8 for the calculation of u_j ,$j = 1,..,J$ and the formation of matrix K and of vector L. The solution of equation 9 gives the new values of coefficients $c_1, c_2..c_M$, which however are not expected to differ noticeably from those calculated by standard least squares fitting and used as initial values for the calculation of u_j^2.

Moreover, $Z = (K^T K)^{-1}$ is a matrix whose diagonal elements z_{jj} are the squared uncertainties (variances) and the off-diagonal elements $z_{ij} = z_{ji}$ are the covariance between fitted coefficients:

$$u(c_m) = \sqrt{z_{mm}} \;\; m = 1..M \tag{10}$$

$$cov(c_k, c_j) = z_{ij} = z_{ji}, \;\; k = 1..M, \;\; i = 1..M \;\; and k \neq i \tag{11}$$

The 95%-confidence margin of a regression parameter is defined as:

$$c_m^{conf} = c_m \pm t^*_{n-p,1-\alpha/2} \sqrt{z_{mm}} \tag{12}$$

with α as the confidence parameter; $\alpha = 0.05$, $t^*_{n-p,1-\alpha/2}$ is the t-value of the Student's t-distribution.

It should be noted that the knowledge of covariance between the fitted coefficients is necessary if one wishes to calculate, in a next stage, the uncertainty $u(\eta)$ in the predicted values of η using equation 5.